

Universität
Rostock



Traditio et Innovatio

MATERIALS FOR CARBON DIOXIDE SEPARATION

DISSERTATION

ZUR

ERLANGUNG DES AKADEMISCHEN GRADES

DOKTOR DER MATHEMATISCH-NATURWISSENSCHAFTLICHEN FAKULTÄT

DER

UNIVERSITÄT ROSTOCK

VORGELEGT VON

QINGQING XU, GEB. AM 27.04.1984 IN CHINA

AUS ALBERT-EINSTEIN-STR.28

ROSTOCK | 01.10.2014

Gutachter:

1. Gutachter:

Prof. Dr. Eberhard Burkel
Institut für Physik, Universität Rostock

2. Gutachter:

Prof. Dr. Martin Köckerling
Institut für Chemie, Universität Rostock

Datum der Einreichung: 01. Oktober 2014

Datum der Verteidigung: 26. November 2014

TABLE OF CONTENTS

Abstract.....	1
Chapter 1 Introduction and Motivation	1
1.1 Global warming.....	1
1.2 CO ₂ capture and separation technologies	2
1.2.1 Cryogenic distillation.....	3
1.2.2 Membrane separation.....	4
1.2.3 Absorption.....	5
1.2.4 Adsorption.....	6
1.3 Carbon materials	7
1.4 Calcium oxide extracted from eggshell.....	9
Chapter 2 Physi- and chemisorption theories	11
2.1 Physisorption	11
2.1.1 The adsorption isotherm.....	11
2.1.2 Adsorption theories	15
2.1.2.1 Surface area.....	15
2.1.2.2 Pore size and pore volume	17
2.2 Chemisorption.....	20
2.3 Comparison of physi- and chemisorption.....	20
Chapter 3 Comparison of CO ₂ capture and separation on carbon materials by physisorption	23

3.1 Experimental methods and characterization procedures	23
3.1.1 Results	24
3.1.1.1 Characterization of the raw powders	24
3.1.1.2 N ₂ isotherms of the carbon materials	25
3.1.1.3 Pore size and volume distributions in carbon materials	27
3.1.1.4 Carbon dioxide adsorption behaviors at room temperature	29
3.1.1.5 Influences of micropore and surface area on CO ₂ adsorption capacity	29
3.1.2 Discussions	31
3.2 Conclusions	33
Chapter 4 CO ₂ chemisorption by doped CaO from wasted eggshell	34
4.1 CaO-based sorbent extracted from dried eggshell	34
4.1.1 Experimental methods and characterization procedures	34
4.1.2 Results and discussion	36
4.1.2.1 Properties of dried eggshell	36
4.1.2.2 Calcination parameters	38
4.1.2.3 N ₂ physisorption properties	43
4.1.2.4 Macro-structure	45
4.1.2.5 Chemical reaction rate	47
4.1.2.6 CO ₂ adsorption stability	49
4.2 Doped CaO with eggshell as source	50

4.2.1 Experimental method	50
4.2.2 Results and discussion	52
4.2.2.1 Calcination parameters	52
4.2.2.2 TiO ₂ Particle size effect	59
4.2.2.3 TiO ₂ weight ratio effect	64
4.2.2.4 N ₂ physisorption properties.....	70
4.2.2.5 Macro-structure	71
4.2.2.6 Chemical reaction rate	73
4.2.2.7 CO ₂ adsorption stability.....	75
4.3 Calcined eggshell as Ca source with CaTiO ₃ dopant.....	77
4.3.1 Experimental Methods	77
4.3.2 Results and discussions.....	78
4.3.2.1 TiO ₂ particle size effect	78
4.3.2.2 N ₂ physisorption properties.....	82
4.3.2.3 Macro-structure	84
4.3.2.4 Chemical reaction rate	87
4.3.2.5 Further optimizing	89
4.4 Conclusions.....	91
Summary.....	93
References.....	96
Legends.....	109

List of Figures.....	109
List of Tables.....	113
List of abbreviations.....	114
Acknowledgements.....	115
Declaration.....	116

Abstract

The search for optimized materials for the capture and separation of carbon dioxide (CO₂) capture is a challenging topic for environmental protection.

Among others, carbon materials are potential solid sorbents for carbon dioxide (CO₂) separation. In present work, the CO₂ adsorption capacities at room temperature have been investigated by comparing carbon nanotubes (CNTs), fullerene (C₆₀), graphenes, graphite and granular activated carbons (GACs). The factors influencing the CO₂ adsorption uptake in these carbon materials were found to be micropore surface, pore size and specific surface area. However, the highest specific surface area did not lead automatically to the highest CO₂ adsorption capacity. It turned out that the amount of the micropore surface area was dominating the CO₂ adsorption ability.

Another promising class of materials for CO₂ capture and separation are calcium oxide sorbents (CaO). CaO has been widely investigated as CO₂ adsorbent due to its high CO₂ capture capacity, wide range of Ca sources, and high selectivity. However, the fast degeneration of its adsorption capacity during loading and unloading cycles hinders its widespread application. Due to the low costs, rich calcium carbonation (CaCO₃) and recycling concept, eggshell was selected as Ca source and traditional calcination was applied on the eggshell to produce CaO-based adsorbents. Two aspects were studied in present work: a new hybrid materials synthesized by doping the calcium titanate (CaTiO₃) and the relationship between physisorption and chemisorption properties of CaO-based materials. The synthesis parameters, the micro structures, the phase composition, the nitrogen physisorption properties and the chemical reaction rates were discussed in detail. A stable CO₂ chemical adsorption capacity with average value of 11.86 mol/kg could be obtained by this new hybrid material and a high stability over 10 cycles allows general application. The CaO carbonation conversion was higher than the CaO derived from commercial CaCO₃.

Keywords: carbon materials, eggshell, CO₂ capture, physisorption, chemisorption, pore

Chapter 1 Introduction and Motivation

1.1 Global warming

Greenhouse gases are natural and anthropogenic gaseous components of the atmosphere absorbing and emitting radiation within the thermal infrared range from surface, atmosphere and clouds of earth [1]. Based on ten-year satellite data, NASA illustrates the energy balance of earth. Most of the incoming sunlight is reflected back to the space and the energy arriving on earth is divided into two parts: i) the first part is absorbed by ground, trees and everything present, ii) the second part is reflected by, among other things, ice and snow back to space. Absorbed energy is released as heat and most of the heat emitted from the earth surface is absorbed by clouds and greenhouse gases, some of which return to the earth, keeping it warm (greenhouse effect) [2-4].

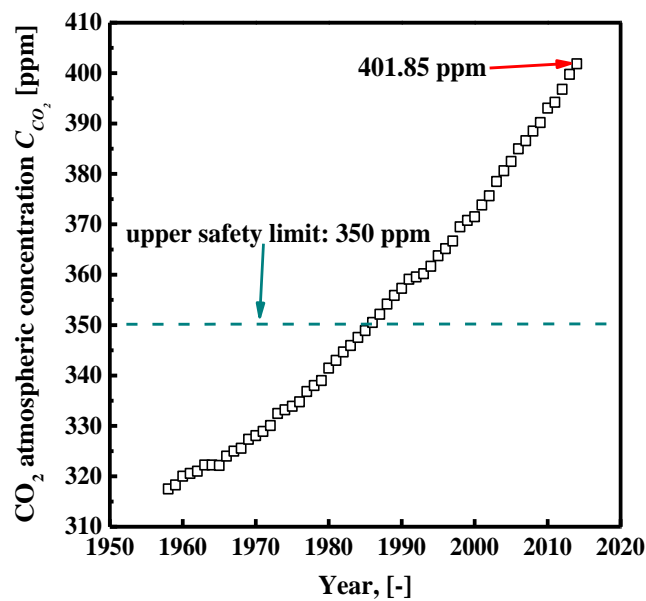


Figure 1.1 Mean concentration of atmospheric CO₂ in May from 1958 to 2014 at the Mauna Loa Observatory in Hawaii [5].

Greenhouse gases in the atmosphere are namely ozone (O₃), water vapor (H₂O), carbon dioxide (CO₂), nitrous oxide (N₂O), methane (CH₄) and the anthropogenic gases such as chlorofluorocarbons (CFCs) and oxidized sulfur gases (SO_x) [1]. Because the gases play important roles in keeping the earth warm, the increasing amount of greenhouse gases can destroy the original balance of the earth's energy budget and lead to global warming. CO₂ has increased by 45 % from 278 ppm in 1750 to 401.85 ppm in 2014

due to the carbon emissions from fossil fuel combustion and cement production. The increasing concentration of CO₂ in atmosphere since 1750 contributes quite a lot to total radiative forcing. The CO₂ concentration growth since 1958 (Figure 1.1), exhibits exponential behavior. The 2013 Intergovernmental Panel on Climate Change Assessment Report (IPCC) indicates that the certainty of human activity being the dominant cause of observed global warming since the mid-20th century is 95 %. This results in increasing temperature of the atmosphere and the oceans, diminishing snow and ice, rising sea levels as well as higher concentrations of greenhouse gases [1]. The CO₂ atmospheric concentration of 350 ppm should be an initial objective target proposed by some scientists such as Rajendra Pachauri [1], Jonathan Foley[6] and James Hansen [7].

1.2 CO₂ capture and separation technologies

On 11th December 1997 in Kyoto Japan, an international agreement ‘The Kyoto Protocol’ connected to the United Nations Framework Convention on Climate Change (UNFCCC) was signed, which set international binding obligations on reducing emission of GHGs. As of 2014 there are 83 signatories and 192 parties [8]. Other approaches are also developed to reduce the CO₂ emissions and mitigate the climate change: 1) search for alternative energy sources [9-12]; 2) enhancement of energy efficiency and conservation [13]; 3) geoengineering [14, 15]; 4) CO₂ capture and storage (or CO₂ capture and sequestration, CCS) [16]. CO₂ capture and storage is considered to be a technically feasible method to make deep reduction in CO₂ emissions from large CO₂ emitters [17]. Many known technologies of gas separation have been utilized and integrated into the CO₂ capture system: cryogenic distillation, membrane separation, adsorption as well as absorption (Figure 1.2).

From the aspect of sorption mechanisms, two basic mechanisms are relevant to the present work: physisorption and chemisorption. Cryogenic distillation and membrane separation are mainly based on physisorption or physical mechanism. Adsorption and absorption can separate CO₂ through both physisorption and chemisorption. In the following sections, these four technologies will be described and introduced.

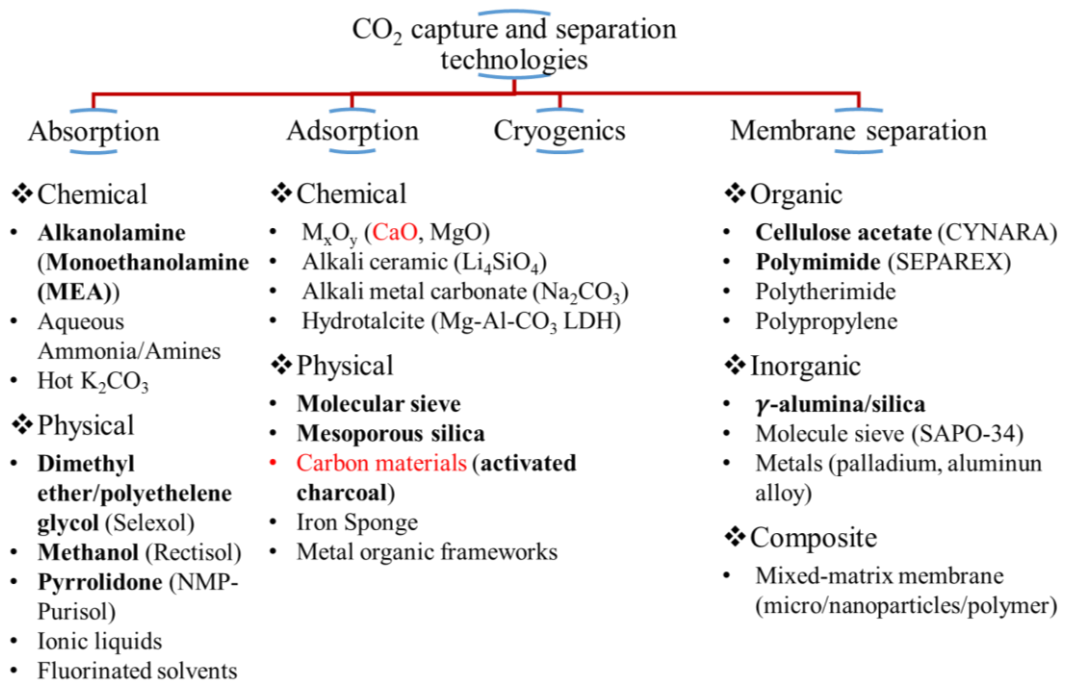


Figure 1.2 Illustration of CO₂ capture and separation technologies and examples [18-21].

1.2.1 Cryogenic distillation

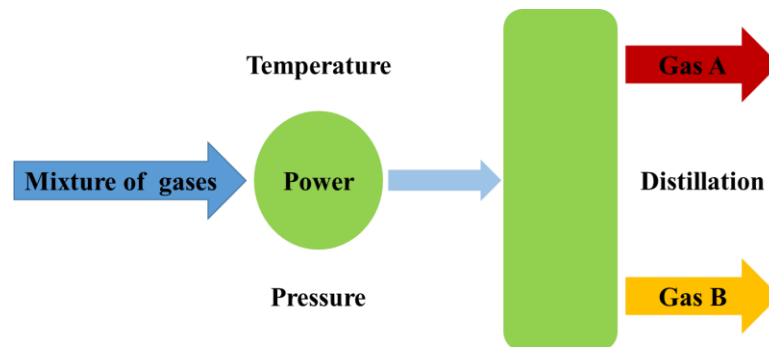


Figure 1.3 Sketch of gas cryogenic distillation [17].

Cryogenic distillation is a conventional air separation process based on the diverse boiling points and volatilities of gases, which condenses the gases into liquid under low temperature and high pressure in order to separate the gaseous components (Figure 1.3). This method is currently operated commercially on the air separation at a large scale [22, 23]. Due to the mature technology, it also can be applied to extract high purity CO₂ (90 % - 95 %) out of a gaseous mixture for easy transportation to storage sites [24]. The critical cryogenic distillation parameters of CO₂ consume intensive energy and increase the costs. Therefore, researchers focus on optimizing the cost by adopting multi-stage compression, refrigeration and separation under high pressures and at ambient temperatures, which is claimed to reduce the energy penalty and to obtain a

CO₂ purity over 99.9 % [25]. Some hybrid cryogenic network is invented by the conjunction of the conventional cryogenic distillation with a desublimation based on multiple packed bed cryogenic separators to reduce the energy costs and to improve the separation performance [26].

1.2.2 Membrane separation

Membrane separation is an energy-saving (no regenerations), continuous, space-saving (no request of a heat-exchange system), environment friendly (without solvent), flexible small-installation and efficient (no phase change) technology [27-29]. A process scheme is presented in Figure 1.4. The drawbacks for the membrane separation technology are the low porous size stability affected by a steam, the decreasing in the permeability and the low selectivity. It is not suitable for the low CO₂ partial pressure environment due to the low driving force and the high flow rate of a steam as well as the critical balance between the permeability and the selectivity [30-32]. Therefore, the membrane separation still faces challenges before it be applied in a large scale in industries [33].

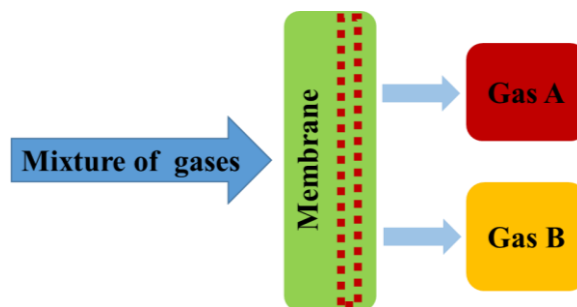


Figure 1.4 Sketch of membrane separation [17].

Membranes can be roughly classified as: inorganic (e.g. metal oxide, ceramic, molecular sieve) [34], organic (cellulose acetate, rubber and polymers such as polyimide and copolymer/polymer blend) [35] and mixed matrix membranes (polymer/inorganic such as zeolite as well as nanoparticle) [36]. Inorganic membranes can be operated at high temperature, pressure and aggressive environment [37]. Zeolite membranes are widely investigated due to their features of the size selectivity as well as the chemical and thermal stability [38]. For instance, Zeolite SAPO-34 [39], T-type [40], DDR [41], FAU [42] and MFI [43] membranes have been reported for the CO₂ gas separation and have exhibited a high selectivity for CO₂ than the other gases. Further improvements in the selectivity and the flux for MFI by preparing a silica MFI

membrane in the fluoride media on an alumina support lead to uniformly oriented channels compared to a conventional MFI or the other zeolite membranes with a random arrangement of crystals [44]. Polymeric membranes have a lot of merits such as low cost of production, flexibility and ease of synthesis. Due to the glass transition temperature T_g , the polymeric membranes are divided into glassy and rubbery polymeric membranes. The commercial polymers mostly used in a small scale are cellulose acetate and polyimide such as CYNARA, Matrimid and SEPAREX. Due to the temperature sensibility of the polymers, the gas flow is normally required to cool down below 100 °C before a separation process [29]. Some modifications have been introduced to the polymer system like amine-PIM-1 [45] (archetypal membrane forming polymer of intrinsic micro porosity), which improves the CO₂ affinity by introducing amine into the system. Recently a number of researches have focused on composite membranes such as MOF mixed matrix membrane based on NH₂-MIL-53(Al) MOF and polyimide [46] which increased the membrane permeability (up to 70 % compared to neat polyimide) without sacrificing the CO₂/CH₄ selectivity. Blended polyethylene glycol/polytrifluoropropylmethylsiloxane presented a higher CO₂/N₂ separation factor 26.67 than 13.79 of PTFPMS [47]. In addition, liquid ionic/polymer composite membrane [48] and zeolite/polymer membrane [49] are being investigated.

1.2.3 Absorption

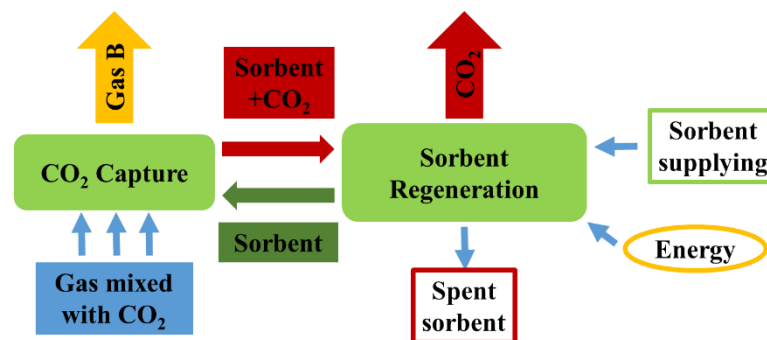


Figure 1.5 Sketch of adsorption/absorption [17].

Absorption is a most mature process for CO₂ capture and separation [24]. Absorption involves dissolving an absorbate into an absorbent phase by a physical or chemical process. The procedure is demonstrated in Figure 1.5, including CO₂ absorption and stripping with mass transfer by varying temperature or pressurization. The advantages

of the absorption are its high CO₂ capture efficiency (> 90 %), flexibility and mature technique [24, 35]. The drawbacks are absorbent degradation, high energy consumption for regeneration and corrosion of facilities [24, 35].

Using Alkanolamine as alkaline solvent dates back to 1930s. Aqueous ammonia and amine are the traditional chemical absorbents and some commercial productions like dimethyl ether/polyethylene glycol (Selextol), methanol (Rectisol) and N-methyl-2-pyrrolidone (Purisol) are physical absorbents. Some nonaqueous solvents have been developed such as silylamines [50] to overcome the drawbacks. Shudong Zheng et al [51] utilized nonaqueous triethylenetetramine (TETA)/ethanol as CO₂ capture solvent which produced a solid precipitate TETA-carbamate after absorption and this solid phase could decompose under 90 °C. Ionic liquids are another new class of the physical absorbents due to their thermal stability, environmental friendliness, CO₂ selectivity and multi-site interaction with CO₂ [52]. Recently, functionalized ionic liquids become popular in researches with either amine [53] or nitrogen-based interacting site on the anion [54].

1.2.4 Adsorption

Adsorption is a process of the molecules landing and accumulating on the internal and external surface of adsorbent through physical or chemical forces. Different from the absorption procedure (bulk phenomenon) which utilizes a liquid absorbent, a solid sorbent is usually selected for the adsorption process (surface phenomenon) to keep CO₂ on its surface [24]. The process of adsorption technology is similar to the absorption technique demonstrated in Figure 1.5. The main criteria for an adsorbent selection are: large surface area, high CO₂ capture capacity, selectivity and regeneration ability, chemical stability, quick ad- and desorption [55]. According to the working temperature, sorbents are classified into three types: i) low-temperature (< 200 °C); ii) intermediate-temperature (200 °C - 400 °C); iii) and high-temperature (> 400 °C) sorbents [56]. Pressure and temperature swings are the main technologies in adsorption and desorption cyclic operations. In the pressure variation type, the adsorption process is executed either at atmospheric pressure and temperature with desorption at lower pressure (vacuum swing adsorption, VSA) [57] or at relatively higher pressure than the ambient pressure with desorption at atmospheric pressure (pressure swing adsorption, PSA) [58]. Temperature swing adsorption (TSA) [59] and electric swing adsorption

(ESA) [60] are alternative technologies of recycling adsorbents by diminishing the equilibrium capacity of the materials with changing temperature.

Various adsorbents have been developed for CO₂ capture including molecular sieves, carbon-based materials, silica, MOFs, metal oxide, alkali ceramic as well as hydrotalcite and so on (Figure 1.2). Among these materials, the molecular sieve such as zeolite X, Y, Z series, silica gel and activated carbon are already commercially available for CO₂ physisorption due to their high surface area [61]. The shortcomings for these materials are the low CO₂ capture capacity and the selectivity as well as the high sensitivity in temperature and moisture [61, 62]. Therefore, more efforts have been made to fabricate different pore structures with an enhanced surface area [63, 64] or graft alkali groups (such as amine) to increase the selectivity [65-67]. To improve the performance of the physical adsorbents under humid operation, Nhung T.T. Nguyen et al [68] have synthesized hydrophobic chabazite-type zeolitic imidazolate frameworks, which presented no CO₂/N₂ separation properties loss under humid condition. The internal covalently functionalizing MOF with primary amine can conduct CO₂ capture in 65 % relative humidity with a full preservation of the MOF structure [69].

Chemical adsorbents such as metal oxides, alkali ceramics and hydrotalcites are promising CO₂ capture materials with a high retaining adsorption capacity and a superior selectivity. Lithium and calcium based materials are widely investigated for the CO₂ capture and separation. Lithium orthosilicate (Li₄SiO₄) and Lithium zirconate (Li₂ZrO₃) possess high adsorption efficiency and rate, which can be applied in high temperature and low CO₂ concentration environment [70-72]. Some metal oxides such as calcium oxide (CaO) and magnesium oxide (MgO) adsorb and release CO₂ by forming and decomposing CO₃²⁻ ion. They are also grafted onto other materials to improve the CO₂ affinity and the adsorption capacity [73-76]. Besides, Sengupta S. et al has focused on the introducing of alkaline metal carbonates into the metal oxide systems to improve the CO₂ adsorption properties [77]. Hydrotalcite is an anionic and layered double hydroxide clay with a general formula $M_{1-x}^{2+}M_x^{3+}(OH)_2A_{x/m}^{m-} \cdot yH_2O$ where the most typical cations are Mg²⁺ and Al³⁺ with Cl⁻/NO₃⁻/CO₃²⁻ anions. Due to the low cost of procurement, Mg-Al-CO₃ hydrotalcite is preferred by some researchers [78].

1.3 Carbon materials

Carbon-based materials are considered as potential solid adsorbents for the CO₂ separation. The advantages of this kind of materials for CO₂ capture are the high surface area, the fast adsorption/desorption kinetics and the large pore volume. Pyrolysis of carbonaceous materials is a custom method to produce the carbon adsorbents, which are mainly consisted of sp²-hybridized carbon atoms and aromatic rings. Based on the stacking of two dimensional structure of the carbon atoms and the aromatic rings, there are many carbon allotropes such as activated carbons (ACs), graphite, graphene, carbon nanotubes (CNTs) and fullerenes [79]. Among them, ACs have been widely applied as a gas adsorbent for a long time such as CO₂, hydrogen, methane and other gas molecules due to its large spectra of surface areas, meso- and microporous carbonaceous structures, as well as hydrophobic and nonpolar surface situations, which weaken the bonding forces between the adsorbents and the adsorbates, leading to an easy regeneration [80-84]. The mechanisms of the ACs with gas adsorption mainly follow diffusion kinetics in pores: in micropore, the surface diffusion dominates the adsorption process along with a steric hindrance depending on the sizes of the pores and the gas molecules; in meso- and macropores, Knudsen diffusion, molecular diffusion and Poiseuille flow occur [27]. Besides the activated carbons, several essays related to CNTs have been published. One branch of these researches is the application of CNTs in gas capture and separation like organic vapors, CO₂/CH₄ separation, hydrogen storage and so on [85-87]. In CNTs gas adsorption, carrier localization and charge distribution mechanisms are present [88]. There are four sites for gas adsorption on the CNTs: vacancies, interstitial channels, external grooves and external surface sites [89]. Graphene is another newly developed carbon material based on the same structure as the nanotubes but in a sheet shape with single or multiple layers. Gas adsorption mainly happens on the graphene surfaces. The research results indicate that the structural defects and the vacancies in graphene are in some degree enhancing the interaction between adsorbate and adsorbent [90-92]. The investigations of the gas adsorption on graphite and fullerene (C₆₀) are relatively rare. The adsorption capacity of C₆₀ depends on the preparation and the purity [93]. There are several types of identified adsorption sites for the C₆₀: dimple sites between four C₆₀ molecules, groove sites between two C₆₀ molecules and hexagonal or pentagonal top of C₆₀ [94, 95]. Carbon-based materials are always compared with other porous materials such as zeolite and MOF on CO₂ adsorption [96-98]. The different properties of the CO₂ capture on different

carbonaceous materials are also investigated by some researchers. Soodabeh Khalili et al [99] studied the CO₂ capture by multi-walled carbon nanotubes (MWNTs) and activated charcoal with a twice higher surface area, demonstrating that the high pore volume and special structure (hollowness and low mass density) of MWNTs contributed more to CO₂ uptake than surface area. Furthermore, the surface-structure effect on the CO₂ adsorption of MWNTs and graphene were also discussed recently [100].

The purpose of this thesis was to systematically evaluate the CO₂ adsorption capacities and the structures as well as the N₂ physisorption properties of the various pristine carbon-based adsorbents including CNTs, C₆₀, graphenes, Graphite and granular activated carbon (GACs). The factors affecting the CO₂ adsorption capacities such as surface areas, micropores, pore sizes and active adsorption sites will be discussed.

1.4 Calcium oxide extracted from eggshell

CaO is a very promising adsorbent due to its fast kinetics of CO₂ capture and regeneration, low cost and most abundant sources such as limestone in nature and high CO₂ capture capacity of 17.8 mol/kg (theoretical) [98]. However, the severe CO₂ capture capacity reduction during cyclic CO₂ capture experiment is a serious disadvantage as a consequence of the thermal sintering and the morphology changes [101]. Introducing dopants or high Tammann temperature (temperature of sintering start) components is one approach being developed to stabilize the cyclic CO₂ capture performance of CaO [102]. Inert materials including SiO₂ [103, 104], MgO [105, 106], Al₂O₃ [107, 108], ZrO₂ [109, 110], etc. are incorporated into CaO to synthesize dopants supported hybrid CaO-based adsorbents, which have been proven to enhance the CO₂ capture performances at different level [111]. In addition, titanium oxide (TiO₂) and calcium titanate (CaTiO₃) are possible candidates as high Tammann temperature dopants and the melting points for them are 1843 °C and 1980 °C [112], respectively. Ching-Tsung Yu et al [113] synthesized Ca/Ti pellets consisting of Ca-Al-CO₃ layered double hydroxide (LDH) impregnated with TiO₂ powders. After 10 cyclic adsorption/desorption, the recovery of Ca/Ti pellets is at least 80 %, while Ca-Al-CO₃ has only 35 % restored. CaO-based sorbents with CaTiO₃ framework are studied and the results proved that the CaTiO₃ prevent the sintering effect on the CaO particles and

stabilized the CO₂ capture efficiency during cyclic reaction [114, 115].

Nowadays, recycling and sustainability are prevailing concepts. Therefore, developing CO₂ adsorbents from waste materials becomes an interesting topic [116]. One of the wasted and useless materials is eggshell. The world egg production is increasing every year, reaching 67.0 million tons in 2013 [117]. Eggshell is a daily house and food industry waste. The wasted eggshells incur an annual disposal cost of about 100,000 euro in Europe reported by a project named SHELLBRANE [118]. D.A. Oliveira et al [119] proposed several potential products obtained from waste eggshells namely calcium as human nutritional supplement, fertilizer, animal feed, heavy metal removal, catalyst in biodiesel, calcium carbonate (CaCO₃) purification and so on. A common way to produce CaO is the thermal decomposition of CaCO₃ and it becomes a suitable choice. Thongthai Wittoon [120] compared the CO₂ adsorption properties of CaO obtained from eggshell and commercial CaCO₃ and pointed out that CaO derived from eggshell exhibited higher carbonation conversion. Some modifications such as acetic acid pretreatment [121] or doping metal oxide (TiO₂, Al₂O₃, CuO and ZrO₂) [122] have been researched to improve the CaO sorbents derived from eggshell.

The purpose of this work is to recycle and to utilize eggshell as a CaO source and to prepare CaO-based sorbent incorporated with the CaTiO₃ which can hinder the sintering effect on the CaO particles and to work as an inert supporter. The morphology of CaO particles is very important to the CO₂ capture performance. Therefore, the N₂ physisorption behaviors of CaO-based materials will be investigated as well the morphologies after different cyclic CO₂ adsorption performances. The relationship between N₂ physisorption and CO₂ chemisorption on the modified CaO-based adsorbents will be discussed.

Chapter 2 Physi- and chemisorption theories

2.1 Physisorption

2.1.1 The adsorption isotherm

Physisorption (physical adsorption) is based on the van der Waals forces (intermolecular forces) between gas and the sorbent/gas, which do not lead to a significant change in the electronic orbital patterns of the gas and the sorbent [123]. The sorbent can easily be regenerated by changing temperature or pressure.

The adsorbed quantity of gas on an adsorbent is proportional to the mass m of the sample. Besides, it also depends on the temperature T and the pressure p of the gas as well as the primitive properties of the adsorbent and the adsorbate. Therefore, the number of moles of the adsorbed gas per gram of solid can be described by the following Equation 2.1 [124]:

$$n = f(p, T, \text{gas}, \text{solid}) \quad (2.1)$$

Equation 2.1 can be simplified by a specific solid and gas at a certain temperature to

$$n = f(p)_{T, \text{gas}, \text{solid}} \quad (2.2)$$

In 1834 Émile Clapeyron first stated the ideal gas law, combining Boyle's law and Charles's law [125]. According to the ideal gas law, the mole volume of an ideal gas at the standard temperature (T_{STP} : 273.15 K) and pressure (P_{STP} : 1 atm) is 22414 cm³/mol and the number of moles n can be calculated as:

$$n = \frac{V_{\text{STP}}}{22414} (\text{mol}) \quad (2.3)$$

Thus, the standard volume V_{STP} can evaluate the gas quantity too. However in reality, gas is unlike ideal gas. Considering the compressibility, van der Waals forces, specific heat capacity, thermodynamic effects and interactions, the ideal gas law cannot really describe the gas behavior [126]. W.V. Loebenstein [127] calculated and compared non-ideal gas corrections and proposed a correction being applied to the ideal gas law:

$$n = \left(\frac{pV}{RT}\right) (1 + \alpha p) \quad (2.4)$$

p and V are pressure and volume of the gas, R is the ideal gas constant (8.314 J mol⁻¹ K⁻¹) and T is the temperature. α is a correction factor for non-ideal gas which is unique to a specific gas at a specific temperature.

The isotherm is based on the gas law theory, which is also the original data for extracting the information of surface area, pore size, pore size distribution and so on.

There are two branches in an isotherm: adsorption and desorption. They have not to be identical. Adsorption is the process, where the concentration of molecules (gas or liquid phase) increases by diffusing to an adsorbent surface, interacting with the sorbent and building up layers on the solid surface as depicted in Figure 2.1 [123, 128]. On the contrary, the reverse process of adsorption where the adsorbed molecules escape from

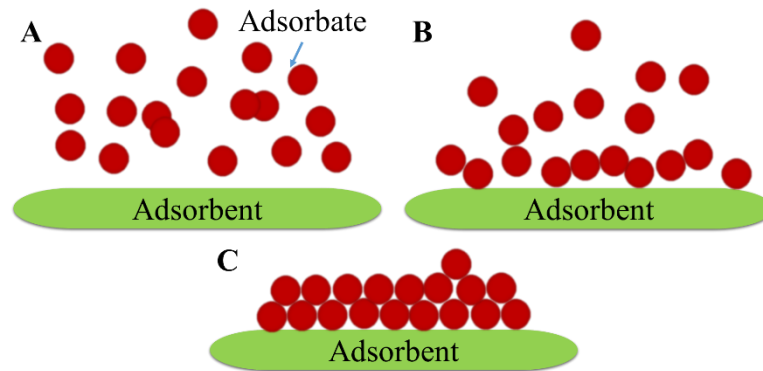


Figure 2.1 Scheme of adsorption process.

a sorbent surface is called desorption. Desorption is accelerated by heating as well as lowering pressure [123]. The isotherm presents the adsorbed volume/pressure relationship at a constant temperature. According to the features of the isotherm, it can be divided into six types (Figure 2.2) (the first five of the adsorption isotherm types originated from Stephen Brunauer [129] and the last one was recently added by Leslie G. Joyner [130]). **Type I** isotherm presents a rapid initial adsorbed uptake at low pressures with a limiting quantity at high pressures (flat region) and the isotherm is reversible in some cases. This isotherm normally appears in microporous powders (pore size smaller than 2 nm), which have pore sizes with a few diameters of the adsorbate molecule. Therefore, the limit of the adsorbed quantity is governed by the accessible micropore volume. The Type I isotherm is sometimes named Langmuir isotherm due to the formation of a monolayer. **Type II** isotherm is encountered with the nonporous or macroporous powders (pore size larger than 50 nm). In this case, monolayer and multilayer occur during the whole adsorption process and the point B (inflection point or knee of the isotherm) is often taken to indicate the end of the monolayer coverage and the beginning of the multilayer. **Type III** isotherm is convex to the pressure axis during the whole adsorption procedure without showing a point B. This isotherm type happens when the affinity of the adsorbate molecules is stronger than the affinity of the

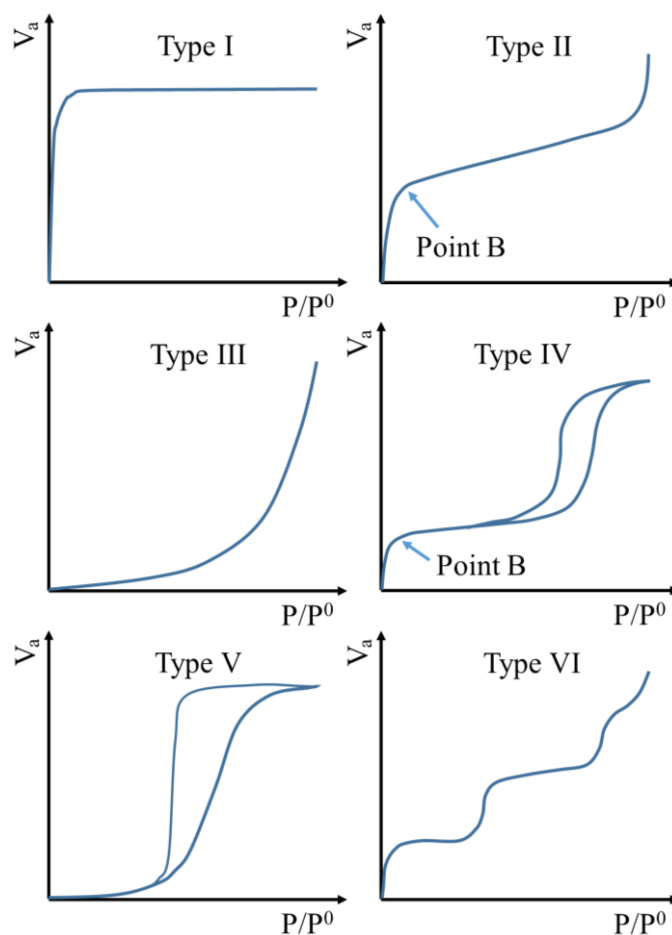


Figure 2.2 The six types of physisorption isotherms.

adsorbate/adsorbent and increasing adsorption occurs after the completion of an interfacial monolayer. The first three isotherm types mentioned above are more or less reversible. The desorption branch of **Type IV** isotherm is different from the adsorption branch and its characteristic feature is the hysteresis loop, which is associated with a capillary condensation in mesopores (pore size between 2 nm and 50 nm). At the low pressure range, the Type IV isotherm is similar to the Type II isotherm with point B. This type of isotherm exists in many mesoporous materials. **Type V** isotherm corresponding to the Type III isotherm arises, when the interaction between an adsorbate and an adsorbent is very small. Due to the existing pores a hysteresis loop occurs.

Type III and Type V contain no information in surface and pore analysis. **Type VI** isotherm results from a uniform non-porous substrate adsorbing stepwise multilayers. The step height demonstrates the monolayer capacity for each adsorbed layer which may maintain almost constant for several layers and the step sharpness depends on the

system and the temperature [128, 131, 132].

In Figure 2.2, Type IV and Type V isotherms exhibit a hysteresis loop related to the different paths of adsorption and desorption. This is the result of the adsorbate molecular capillary condensation in pores (usually mesopores). Capillary condensation occurs when a multilayer forms in a pore and the remaining space of the pore is filled with condensate menisci. More precisely, condensation happens in the inner core rather than directly in the pore itself. This phenomenon vanishes with pore size decreasing to small size such as micropores [123, 124].

In an evaporation process, adsorbed molecules escape from the liquid surface. On contrary, in the condensation process adsorbative molecules arrange themselves from pore walls inwards to the middle core with decreasing radii. Thus, the curvatures of adsorption and desorption are quite different from each other as well as the inhabitation of evaporation which leads to a hysteresis loop. According to the International Union of Pure and Applied Chemistry (IUPAC) classification [131], there are four types of hysteresis loops presented in Figure 2.3. Type **H1** (Type A) has very steep and vertical adsorption and desorption branches which run parallel to each other over a certain pressure range. Leonard H. Cohan [133] explained that this H1 hysteresis loop is caused by condensation in cylindrical pores with opening ends which also include tubular pores with slightly wider parts or one narrow part, tubular pores of two main dimensions, as well as wide ink-bottle and wedge shaped pores. Some porous materials exhibit H1 hysteresis when they are composed of agglomerates or compacts of homogeneous sphere particles in regular arrange and, therefore, have a narrow pore size distribution such as zeolite (SBA-15 and MCM-41 type porous materials) [134, 135] and agglomerates of sphere particles like MgO-Al₂O₃ aerogel [136]. The adsorption branch of Type **H2** (Type E) is gradient and the desorption branch is almost perpendicular at intermediate pressure. The pore shapes causing this type of hysteresis are not well-defined. It is supposed to be the co-effect of ink-bottle pores and a network. However, many porous substrates tend to show Type H2 hysteresis loops such as porous silica/alumina, some porous polymers and inorganic oxide like TiO₂ or MgO [137-140]. There is no adsorption limiting at high pressure for Type **H3** (Type B). The adsorption and desorption branches have sharp slopes at saturation pressure and intermediate pressure, respectively. Type H3 is normally associated with the slit-shaped or parallel walls formed pores with open ends as well as the pores with very wide bodies and

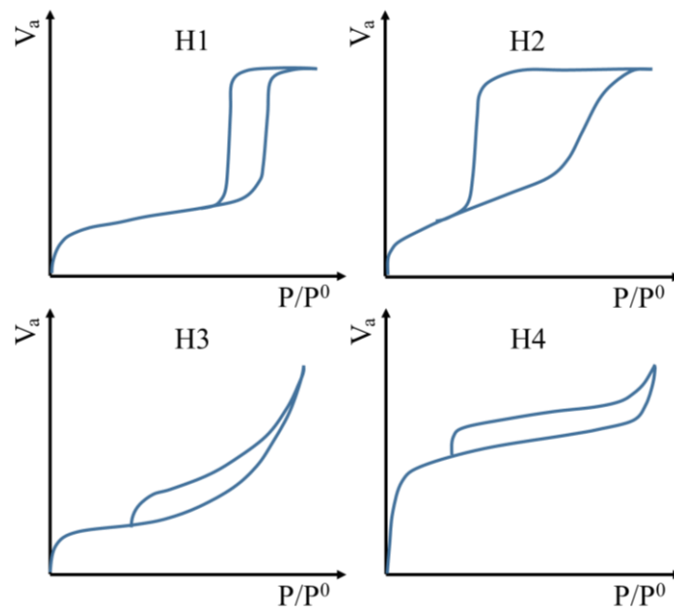


Figure 2.3 Hysteresis loop types of physisorption isotherm.

narrow short necks. More slit-shaped pores are introduced into system with aggregates of plate-like particles. A very typical example is graphene consisting of two-dimensional particles which exhibit Type H3 hysteresis loops [141]. The two branches of Type H4 are similar to Type H1 but horizontally parallel over a wide range of pressure and steep pressure ranges close to Type H3. Narrow slit-like pores contribute to such a kind of hysteresis loop. Besides, the similarity of Type H4 to Type I physisorption isotherm indicates the existence of micropores.

The isotherm and hysteresis loop types are crucial for understanding the feature characteristics of gas adsorption behavior in materials. However, in reality actual materials always possess a broad range of pore sizes and networks. Hence, thermodynamics and other principles are necessary to derive acceptable surface area and pore volume information.

2.1.2 Adsorption theories

2.1.2.1 Surface area

The adsorbed layers can be divided into two types: monolayers (Langmuir adsorption) and multilayers. Langmuir [142, 143] developed a kinetic approach to describe the Type I isotherm situation which is applied more appropriately to chemisorption. There are several Langmuir assumptions: i) only one molecular single layer formed on the adsorbent surface (monolayer adsorption), ii) homogeneous adsorbent surface

(identically energetical sites) and iii) no interactions among adsorbed gas molecules.

The Langmuir equation is

$$V_a = \frac{V_m b p}{1 + b p} \quad (2.5)$$

where b is an empirical constant. V_a and V_m are the volumes of the adsorbed gas molecules and the completely covered monolayer at pressure p .

Later Stephen Brunauer, P.H. Emmett and Edward Teller studied the gas adsorption in multi-molecular layers and generated a universal equation of multilayer adsorption based on the Langmuir concept which is known as BET theory [144]. There are several assumptions to apply the Langmuir concept to multilayer adsorption: i) equal energy for each adsorbed layer, ii) infinite number of adsorption layers, iii) no interaction among each adsorption layer, iv) equal rate of gas molecular condensation on an already adsorbed layer compared to the rate of evaporation from this adsorbed layer. After summing the volume of each adsorbed layer by applying Langmuir theory, a new expression can be derived:

$$V_a = \frac{V_m C p}{(p_0 - p) \left[1 + (C - 1) \frac{p}{p_0} \right]} \quad (2.6)$$

Here p_0 is the saturation gas pressure and C is the BET constant and related to the heat (E_1) of the first layer and the heat (E_L) of liquefaction of the adsorbate [145]

$$C \propto \exp \frac{E_1 - E_L}{RT} \quad (2.7)$$

R is the gas constant. According to Equation 2.6, isotherm possesses an s-shape curve and two regions. When $p \ll p_0$ (low pressure region), Equation 2.6 becomes

$$V_a = \frac{V_m C \left(\frac{p}{p_0} \right)}{1 + C \left(\frac{p}{p_0} \right)} \quad (2.8)$$

$\frac{p}{p_0}$ is named relative pressure. The isotherm becomes concave towards the pressure axis.

In the high pressure region ($p \rightarrow p_0$), the isotherm tends to be convex towards the pressure axis. Thus, there is a Point B in isotherm (Figure 2.2).

For convenient calculation, Equation 2.6 can be rearranged into linear form

$$\frac{p}{V_a(p_0 - p)} = \frac{1}{V_m C} + \frac{C - 1}{V_m C} \left(\frac{p}{p_0} \right) \quad (2.9)$$

With the application of Equation 2.9, the values of $p/[V_a(p_0 - p)]$ are plotted against p/p_0 , which can produce a straight line with intercept $1/V_m C$ and slope $(C - 1)/V_m C$. Based on this straight line or a regression line, the values for V_m and C can be calculated.

The specific surface area S_{BET} of the adsorbent per gram is calculated from V_m with equation

$$S_{BET} = \frac{V_m \sigma N_A}{m V_0} \quad (2.10)$$

$$\sigma = 4 \times 0.866 \times \left[\frac{M}{4(2N_A \rho)^{1/2}} \right]^{2/3} \quad (2.11)$$

where σ is the surface area occupied by one adsorption molecule which is according to the assumption of close packing on a surface, N_A is the Avogadro constant, m is the mass of adsorbent, V_0 is the mole volume of adsorbate, M and ρ are the molecular weight and density in liquid phase. In our study, the σ for nitrogen (N_2) is 16.2 \AA^2 calculated by Stephen Brunauer, P.H. Emmett and Edward Teller.

2.1.2.2 Pore size and pore volume

Pores are classified into three groups depending on the various pore size ranges: i) micropores: $< 2 \text{ nm}$, ii) mesopores: $2 \text{ nm} - 50 \text{ nm}$, iii) macropores: $> 50 \text{ nm}$. The attractive forces are enhanced when adsorbate molecules are sticking to the wall and these forces lead to the beginning of gas condensation. Condensation only happens in relatively large pores and very commonly in mesopores. Normally, the Kelvin equation [146] is applied to derive pore sizes and pore size distributions, by connecting the critical condensation pressures and the pore sizes.

$$\ln \left(\frac{p_v}{p_0} \right) = - \frac{2\gamma v_L \cos \theta}{R T r_k} \quad (2.12)$$

Here p_v and p_0 are the equilibrium vapor pressures of the condensate (critical condensation pressure) in a pore and the equilibrium pressure of the same adsorbate on a plane surface, respectively. The terms γ and v_L are the liquid surface tension and the molar volume of the condensate. r_k and θ are the mean radius of curvature of the liquid meniscus and the contact angle of condensate/substrate (Figure 2.4), respectively.

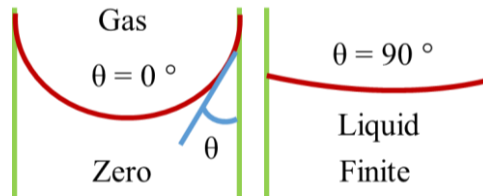


Figure 2.4 Illustration of contact angle.

According to the Kelvin Equation 2.12, condensation is dependent on the liquid/solid contact angle and the pore radius at a certain temperature. The gas condenses in a pore

when the contact angle is smaller than 90° and the process continues as long as the adsorptive pressure is higher than p_v . The condensation occurs firstly in small pores rather than in big pores. There are different geometries of pore structures such as cylinders, slits, spheres etc. Generally, porous materials contain not only one specific pore geometry but a combination of various pore geometries which is too complicated for a mathematical description and calculation. Thus, the most common way is to assume a cylindrical pore model and Equation 2.12 becomes

$$\ln\left(\frac{p_v}{p_0}\right) = -\frac{2\gamma v_L}{r_k RT} \quad (2.13)$$

which is the applied equation for pore size analysis with adsorption branch.

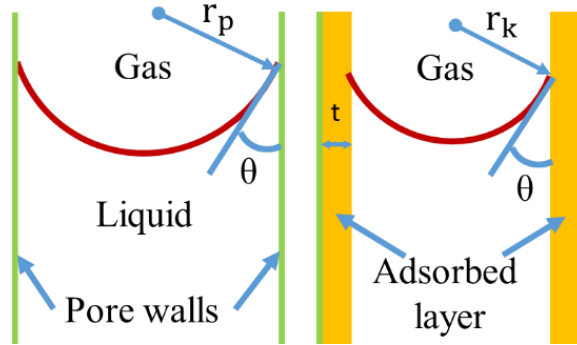


Figure 2.5 Demonstration of pore size.

However, the condensation happens after the adsorption of the multilayer which means that the pore diameter obtained from the Kelvin equation is the size of the condensed liquid core. The real pore size (r_p) should include the thickness (t) of the adsorbed multilayer (Figure 2.5). Therefore, the real pore size is

$$r_p = r_k + t \quad (2.14)$$

The most frequently employed equations for adsorbed layer thickness are from the researches from Halsey [147] as well as from Harkins and Jura [148]. Harkins and Jura derived an expression without the molecule area to determine the surface area of an adsorbent based on an assumption of condensation on a plane surface (Equation 2.15).

$$\log\left(\frac{p}{p_0}\right) = B - \frac{A}{v_a^2} \quad (2.15)$$

This equation leads to a linear region with A and B as slope and intercept, respectively. Therefore, the statistical thickness of the adsorbed condensed layer can be related to the quantity of adsorbed gas [145].

$$t = \left[\frac{A}{B - \log_{10}\left(\frac{p}{p_0}\right)} \right]^{\frac{1}{2}} \quad (2.16)$$

A and B values are empirical and available for the tested adsorbates and adsorbents. In our work, N₂ has been used as operation gas for physisorption and the values for A and B are 13.99 and 0.034, respectively.

Another description of the thickness of a condensed film on a plane surface is called t-plot, which correlates to thickness and the adsorbed volume [149].

$$t = t_m \left(\frac{V_a}{V_m} \right) \quad (2.17)$$

t_m is the thickness of the adsorbate monolayer and 3.54 Å is taken for N₂. A typical expression is presented by the Halsey [147] equation and for N₂ in the following form

$$t = 3.54 \left[\frac{-5.00}{\ln\left(\frac{p}{p_0}\right)} \right]^{\frac{1}{3}} \quad (2.18)$$

The value 5 is empirical and the exponent 1/3 is obtained from the application of the Lennard-Jones potential equation [150]. This thickness calculation form tends to analyze an isotherm at multilayer region (higher pressure area).

After discussing the pore size analysis, the similar theory of the Kelvin equation is also employed for the calculation of pore size distributions. During the mathematical handling, one can either follow the adsorption or the desorption branch of the isotherm. One situation should be considered that the pores must be completely filled and this requests a relative pressure (p/p₀) about 0.995. A common calculation approach is from the work of Elliott P. Barrett, Leslie G. Joyner and Paul P. Halenda [151], called BJH method. By a stepwise decrease of pressure such as from 0.99 to 0.95, 0.91 etc., the quantity loss of adsorbate in each step is equal to the core volume of condensed gas in the pore. The rest of the adsorbed molecules are still considered as the thickness t on the pore wall and this thickness can be calculated by Equation 2.16 or Equation 2.18. Then correlating the Kelvin equation with Equation 2.14, the real pore size r_p can be calculated which corresponds to the pore volume at this point of the relative pressure. And the total pore volume (V_{tp}) is the summation of each pore volume (V_w) with pore width W.

$$V_{tp} = \sum_W V_W \quad (2.19)$$

2.2 Chemisorption

In Section 2.1.2.1 the Langmuir theory was briefly presented. Since this theory is more suitable for chemisorption, more details of the Langmuir equation as chemisorption application are discussed in this section.

According to the kinetic theory of gases, the adsorption rate at any second is a function of the number of molecules colliding to a unit area per second, which means a function of pressure p . Assuming the total accessible adsorption sites number is N_m , the occupied sites number is N_a and the coverage of the monolayer is θ . The Langmuir equation then is

$$\theta = \frac{N_a}{N_m} = \frac{bp}{1+bp} \quad (2.20)$$

or

$$\frac{p}{N_a} = \frac{1}{N_m b} + \frac{p}{N_m} \quad (2.21)$$

where b is an empirical constant which presents the adsorption energy E_a . The coverage θ can be expressed as

$$\theta = \frac{V_a}{V_m} \quad (2.22)$$

Combining Equation 2.20 and Equation 2.22, the linear form of equation includes volume and pressure variants

$$\frac{p}{V_a} = \frac{1}{V_m b} + \frac{p}{V_m} \quad (2.23)$$

At ultra-low pressure, the value of bp in Equation 2.20 is much smaller than 1. Therefore, Equation 2.20 can be written as

$$\theta = \frac{N_a}{N_m} = bp \quad (2.24)$$

This means that the quantity of the adsorbed molecules is proportional to the pressure and this region is called Henry's law region. At high pressure, the term bp is much larger than 1. Then Equation 2.20 can be expressed as

$$\theta = \frac{N_a}{N_m} = 1 \quad (2.25)$$

which indicates the complete occupation of the active adsorption sites.

2.3 Comparison of physi- and chemisorption

Some theories have been discussed above about the physic- and chemisorption. Due to

the different gas-solid connection behavior, various theories have been developed to describe and understand the gas adsorption on solid surfaces. In this section, a comparison between physisorption and chemisorption will be carried out.

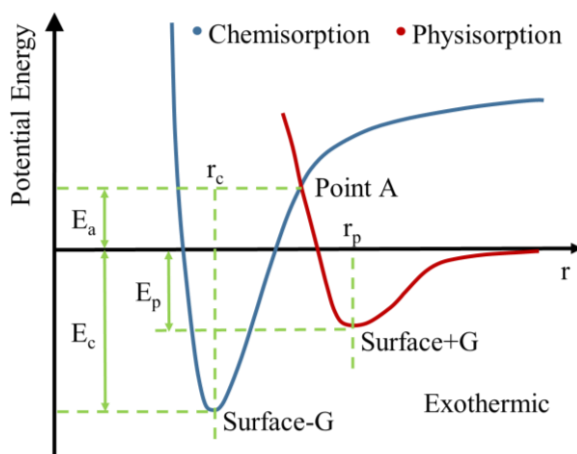


Figure 2.6 Illustration of the potential energy relationship between physisorption and chemisorption [145].

Figure 2.6 depicts the potential energy tendencies and the energy relationship during the adsorption process [128, 145]. A gas molecule (G) mobilizes towards the solid surface along the axis r (distance). Physisorption happens first and it arrives equilibrium (Surface+G). This process is exothermic and gives physisorption energy E_p . If the gas approaches further to r_c , extra energy E_a must be injected into the system to activate the process and point A is a transition point from physisorption to chemisorption. After the dissociation of the gas molecules on the adsorbent surface, chemical adsorption approaches equilibrium (Surface-G) at position r_c ($<r_p$) due to the orbital overlap with closer nuclei and the chemical energy is E_c . This activation process results in the preferable behavior of chemisorption at high temperature and physisorption at low temperature.

Table 2.1 compares physisorption and chemisorption from bonding mechanism to adsorption models. First of all, as the illustration in Figure 2.6 shows, that the interaction of adsorbate-adsorbent for physisorption is a Van der Waals force which is weak and long ranged, while covalent or ion bond is the chemical bonding for chemisorption which is strong and short ranged. In physisorption, a gas molecule attaches on any sites of the surface. On contrary, a gas molecule has a very high selectivity on adsorbent surface in chemisorption. Because of the activation procedure, the energy for chemisorption is normally higher than the necessary energy for

Table 2.1 Physisorption versus Chemisorption [128].

properties	Physisorption	Chemisorption
Bonding	Van der Waals: weak and long range bonding	Chemical bonding: strong and short range bonding
Surface specific	No: on any surface with low enough temperature	Yes: CO ₂ on CaO but not on gold or mercury
Entropy	$\Delta H_{\text{ads}} = (5 \sim 50) \text{ kJ mol}^{-1}$	$\Delta H_{\text{ads}} = (50 \sim 500) \text{ kJ mol}^{-1}$
Being activated	No: fast achieving equilibrium and reducing surface coverage with increasing temperature	Yes: slow equilibrium and enhanced adsorption with increasing temperature
Surface reaction	No	Yes
Adsorption layer	Multilayer	Monolayer
Adsorption equilibrium model	BET isotherm	Langmuir isotherm

physisorption. Generally, further adsorption happens after the completion of the first layer with physisorption and the adsorbate spreads out on the condensed gas monolayer to form a multilayer. Thus, BET theory is adapted for physisorption. However, for chemisorption the adsorbate reacts with adsorbent and forms a monolayer. It is difficult to reach a multilayer in this situation due to the required high temperature.

Chapter 3 Comparison of CO₂ capture and separation on carbon materials by physisorption

3.1 Experimental methods and characterization procedures

Multi-walled carbon nanotubes (MWNTs(1020): diameter from 10 nm to 20 nm; and MWNTs(60100): diameter from 60 nm to 100 nm) and single-walled carbon nanotubes (SWNTs(2): diameter < 2 nm) with purities over 95 % were purchased from Shenzhen Nanotech Port, Ltd., China. Graphite powder (325 mesh, purity of 99.9 %) and granular activated carbons (GACs, 20 - 40 mesh) were purchased from Alfa Aesar, Germany. The fullerene powders (C₆₀) with purity of 99.5 % were obtained from SES Research, Huston, USA. Graphene Nano Platelets (Graphene-750, with average surface area of 750 m²/g) were acquired from XG Sciences, Lansing, USA and Graphene Nano Platelets (Graphene-125, with average surface area of 125 m²/g) were obtained from Graphene Research, Manchester, United Kingdom.

All of the carbon material powders were characterized by high energy synchrotron radiation diffraction at beamline BW5 (DORIS III storage ring, DESY/HASYLAB Hamburger Synchrotron Laboratory) to identify the crystal structures. These measurements were performed with a wavelength of 0.124 Å.



Figure 3.1 An overview of Micromeritics ASAP 2020 [152].

CO₂ and N₂ adsorption on carbon materials were measured by the Micromeritics Accelerated Surface Area and Porosimetry System 2020 (ASAP 2020, America) Analyzer (Figure 3.1). The carbon materials in the form of powder (with sample mass of at least 200 mg) were degassed in two stages. In the first stage, samples were degassed under an evacuation phase for 2 hours and later in a heating phase for 10 hours at 300 °C. After cleaning, the samples were plugged into the Micromeritics ASAP 2020 Analyzer. Incrementally dosing of CO₂ into adsorbent tubes at different pressures was applied to analyze the CO₂ adsorption capacities at room temperature (25 °C). The specific surface areas (SSA) were calculated by using the Brunauer Emmett and Teller (BET) equation through N₂ adsorption isotherms collected at -196 °C. The pore size distributions (PSDs) in carbon materials were measured using Barrett-Joyner-Halenda (BJH) analysis following the adsorption of N₂ on the powders. The micropore volumes of carbon adsorbents were calculated according to the Harkins and Jura equation with t-plot analysis method through N₂ adsorption.

3.1.1 Results

3.1.1.1 Characterization of the raw powders

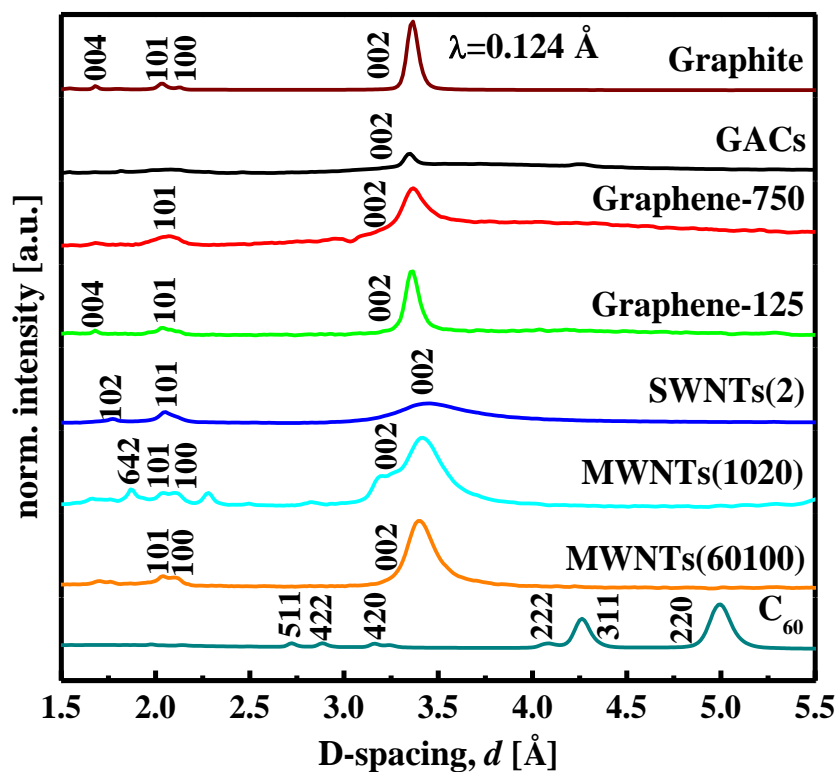


Figure 3.2 High energy synchrotron radiation diffraction patterns for carbon materials.

Table 3.1 The full widths at half maximum of plane (0 0 2) and (1 0 0) for carbon adsorbents calculated from high energy synchrotron radiation diffraction patterns.

Adsorbents	Plane (0 0 2) Width (Å)	Plane (1 0 0) Width (Å)
Graphite	0.06 ± 0.001	0.04 ± 0.005
GACs	0.06 ± 0.002	0.07 ± 0.020
Graphene-750	0.14 ± 0.004	0.06 ± 0.020
Graphene-125	0.08 ± 0.001	0.03 ± 0.010
SWNTs(2)	0.38 ± 0.010	0.05 ± 0.010
MWNTs(1020)	0.22 ± 0.005	0.06 ± 0.002
MWNTs(60100)	0.15 ± 0.003	0.05 ± 0.010

Figure 3.2 shows the diffraction patterns obtained with high energy synchrotron radiation. Table 3.1 gives the full widths at the half maximum (FWHMs) of plane (0 0 2) and (1 0 0) for carbon materials with different structures and sizes derived from the diffraction data. For carbon nanotubes, the main diffraction peaks at $3.39 \text{ \AA} \pm 0.013 \text{ \AA}$ to $3.45 \text{ \AA} \pm 0.013 \text{ \AA}$ related to the (0 0 2) in the plane spacing, which broadened from the MWNTs(60100), MWNTs(1020) to the SWNTs(2). The peaks at 2.28 \AA and 3.21 \AA in the MWNTs(1020) are caused by impurities. The width of the plane (1 0 0) for the SWNTs(2) with respect to the wall distances was similar to the MWNTs (Table 3.1). The peaks at $3.37 \text{ \AA} \pm 0.013 \text{ \AA}$ for graphenes and Graphite belonged to the (0 0 2) plane spacing. The peak widths of plane (0 0 2) (Table 3.1) became narrower from Graphene-750 (0.14 \AA), Graphene-125 (0.08 \AA) to Graphite (0.06 \AA), indicating the increase of crystallinity. While graphenes were mainly two dimensional layers, the broader plane (1 0 0) width of Graphene-750 indicated the smaller horizontal particle size. Peak broadening demonstrated the decreasing particle sizes. In the C_{60} sample, the peaks at $5.00 \text{ \AA} \pm 0.013 \text{ \AA}$ and $4.26 \text{ \AA} \pm 0.013 \text{ \AA}$ corresponded to the C_{60} (2 2 0) and (3 1 1) plane spacings, respectively. In the GACs sample, the (0 0 2) plane spacing was centered at $3.35 \text{ \AA} \pm 0.013 \text{ \AA}$. Although the element carbon had many different allotropes, their structures were basically similar with d-spacing around 3.4 \AA , except the C_{60} (Figure 3.2). CNTs and graphenes could be seen as mono- and multi- graphite layers rolled into cylinders or spread into two dimensions, giving rise to similar plane spacing.

3.1.1.2 N_2 isotherms of the carbon materials

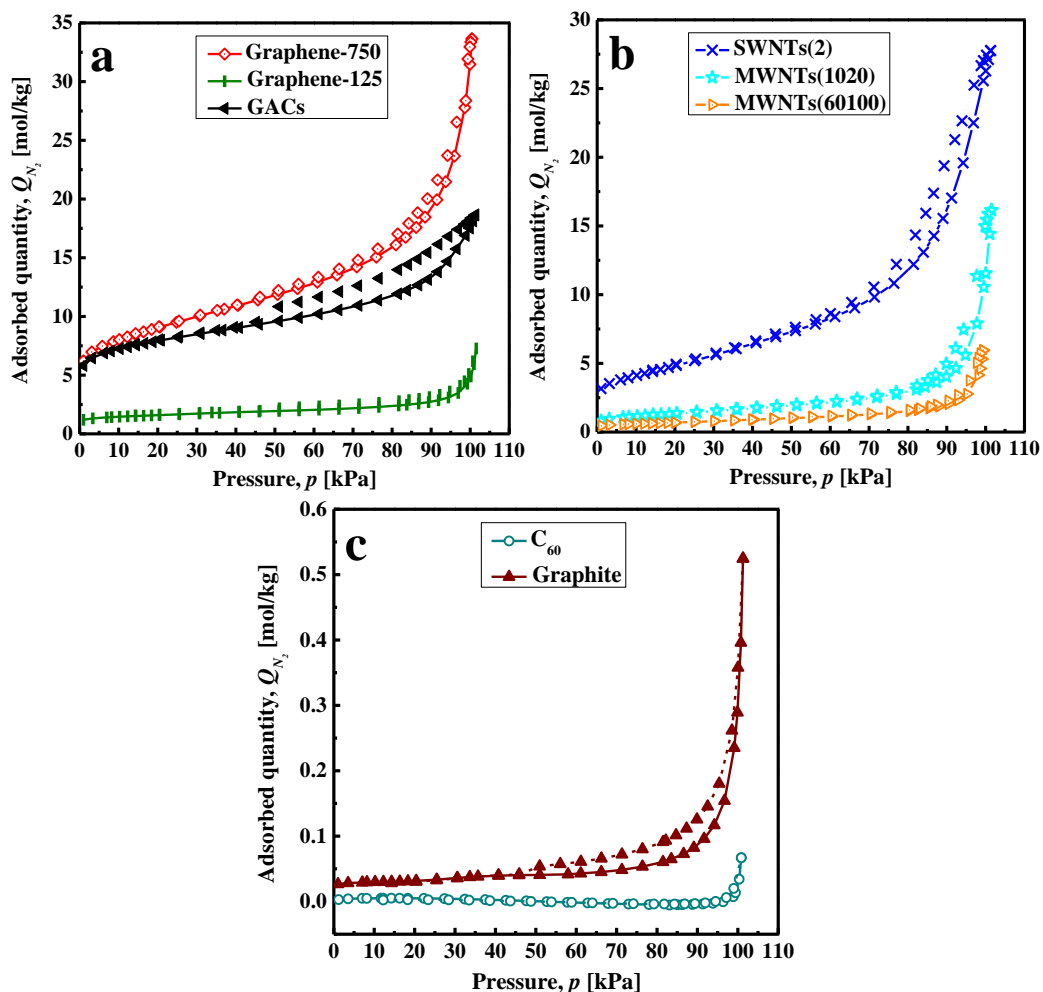


Figure 3.3 Adsorption (solid line) and desorption (dash line) N_2 isotherms for different carbon materials at $-196\text{ }^\circ\text{C}$.

Figure 3.3 presents the N_2 adsorption and desorption isotherms at $-196\text{ }^\circ\text{C}$ for various carbon adsorbents. Comparing all N_2 isotherms of carbon materials in Figure 3.3, there were high initial adsorbances below 1 kPa for GACs, graphenes and CNTs. Furthermore, GACs and Graphene-750 had the highest initial uptakes (Figure 3.3a), while C_{60} and Graphite had the lowest ones (Figure 3.3c). SWNTs, MWNTs and Graphene-125 were in the middle (Figure 3.3a, b). Based on the IUPAC classification [131], the N_2 isotherms for the GACs, graphenes and CNTs belonged to Type IV with inversion point (point B) accompanied by H3 and H1 hysteresis loops. In the H1 hysteresis loop, the adsorption and desorption branches were more likely parallel to each other and nearly vertical in a narrow pressure range. However, both the adsorption and desorption branches in the H3 hysteresis loop were gradient and not vertical/horizontal over a broad pressure region. Graphite and C_{60} possessed the Type V N_2 isotherms which were convex to the pressure axis following the H1 and H3

hysteresis loops (Table 3.2) because of the very weak interactions between adsorbates and adsorbents. Table 3.2 also demonstrates the BET specific surface areas (SSA) for all the carbon adsorbents. Graphene-750 had the highest SSA value. The surface area of GACs was slightly lower. The SSA of Graphene-125 was only half the value of the SWNTs(2), but slightly higher than the SSA of MWNTs(1020).

Table 3.2 Physical properties of various carbon adsorbents.

Adsorbents	SSA	Isotherm	Hysteresis	C_{ad}	Isotherm
		type	loop type		type
		N_2	N_2		CO_2
GACs	617 ± 6	IV	H3	1.78	I
Graphene-750	716 ± 3	IV	H3	1.43	I
Graphene-125	124 ± 1	IV	H3	0.83	III
SWNTs(2)	390 ± 2	IV	H3	0.50	III
MWNTs(1020)	108 ± 0.1	IV	H1	0.23	III
MWNTs(60100)	55 ± 0.1	IV	H1	0.21	III
Graphite	2 ± 0.02	V	H3	0.06	III
C_{60}	0.4 ± 0.02	V	H1	0.03	III

Note: SSA = Specific surface area (m^2/g , BET), C_{ad} = CO_2 sorption capacity at $25^\circ C$ (mol/kg).

3.1.1.3 Pore size and volume distributions in carbon materials

N_2 gas was applied to analyze the pore situation. However, there was a detection limit with the BJH calculation for pore sizes between 1.7 nm and 300 nm. The results were derived from BJH adsorption branches shown in Figure 3.4 and indicated that these carbon materials had broad pore size distributions from 1.7 nm to 220 nm. Nevertheless, C_{60} and Graphite had pore volume values of zero meaning non-porous powders or very low attraction to adsorbates. In the lower pore diameter range (1.7 nm to 5 nm), graphenes and CNTs had relative narrow pore diameter distributions while no peak was observed in this area for GACs. The pore size distribution for GACs may even indicate pore diameters smaller than 1.7 nm which exceeded the detection limit of the instrument. Furthermore, the amounts of pores in Graphene-750 and SWNTs(2) centered around $2.6 \text{ nm} \pm 0.4 \text{ nm}$ and $2.8 \text{ nm} \pm 0.5 \text{ nm}$ were much higher than those for Graphene-125 ($2.4 \text{ nm} \pm 0.6 \text{ nm}$) and MWNTs ($2.8 \text{ nm} \pm 0.7 \text{ nm}$) which were very close to each other. However, the situation changed with high pore diameters. SWNTs(2) showed a pore size distribution around 18 nm with FWHM range from 6 nm to 45 nm with the highest amount of pores. The amounts of pores in Graphene-750 and MWNTs(1020) were relatively lower with pore sizes centered around 30 nm (FWHM

range between 16 nm and 91 nm) and 46 nm (FWHM range between 25 nm and 290 nm). In contrast to Graphene-750 and SWNTs(2), GACs displayed less than half of the pore amount in the vicinity of 23 nm with a FWHM range from 4 nm to 44 nm. MWNTs(60100) and Graphene-125 shifted to larger pore diameter range at 119 nm (FWHM range between 34 nm and 319 nm) and 204 nm (FWHM range from 30 nm to 355 nm); and exhibited much broader pore size distributions.

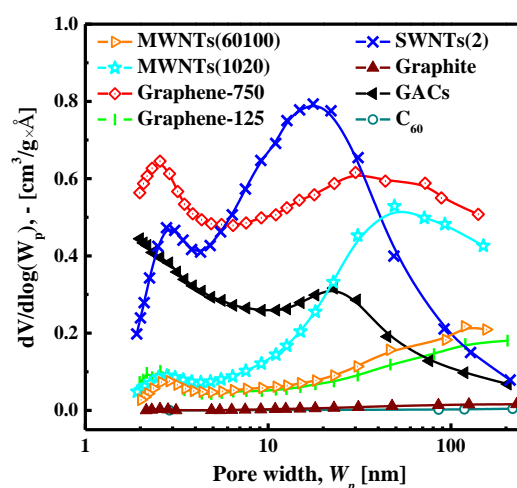


Figure 3.4 Pore size distribution of different carbon materials with N₂ under -196 °C.

Table 3.3 Pore volumes, sizes and distribution ranges for different carbon adsorbents.

Adsorbents	APW	PV	% of total PV in stated pore size (nm) range		
			< 2	2 - 50	> 50
GACs	3.80	0.63	21.2	68.5	10.3
Graphene-750	5.38	1.17	8.4	72.8	18.8
Graphene-125	4.78	0.25	10.7	45.3	44.0
SWNTs(2)	9.09	0.99	0.7	91.0	8.3
MWNTs(1020)	13.5	0.57	0.8	62.2	37.0
MWNTs(60100)	10.5	0.21	1.5	66.9	31.6
Graphite	13.7	0.02	3.4	39.8	56.8

Note: APW = average pore width (nm), PV = total pore volume (cm³/g).

Besides the pore size distribution in Figure 3.4, a direct data analysis on pore volumes, sizes and distribution ranges derived from ASAP 2020 reports for carbon adsorbents is given in Table 3.3, except for C₆₀ which had exceeded the detection possibilities of the machine. Apart from Graphene-125 and Graphite, the rest materials mainly exhibited mesoporous features and SWNTs(2) had the highest mesopore content of 91.0 % (Table 3.3). The ratios of mesopores and macropores were similar in Graphene-125 and Graphite contained slightly more macropores. GACs and graphenes presented

relative small average pore sizes and high micropore volume percentages (< 2 nm) (Table 3.3). According to the total pore volume, Graphene-750 and SWNTs(2) possessed superior values, and the value for Graphite was very low.

3.1.1.4 Carbon dioxide adsorption behaviors at room temperature

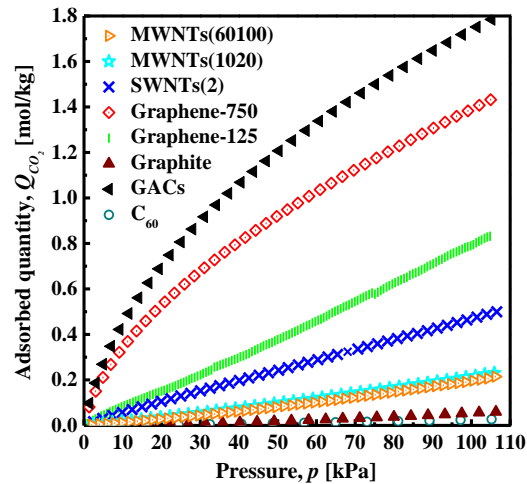


Figure 3.5 Pure CO₂ adsorption isotherms on various carbon materials at 25 °C.

The CO₂ adsorption capacities of carbon materials were characterized by the Micromeritics ASAP 2020 analyzer at 25 °C. The corresponding isotherms are shown in Figure 3.5. According to the IUPAC classification [131], the CO₂ isotherms for GACs and Graphene-750 belonged to type I with a prompt initial adsorption amount at a relatively low pressure and decreasing adsorbed speed towards the high pressure region; the rest of isotherm curves changed into type III, which did not have the inflection points (point B) on the isotherms indicating monolayer completions and the curves were concave towards the pressure axis. The isotherm types and the maximum values of CO₂ adsorbate are presented in Table 3.2. Compared to the other carbon sorbents, GACs (1.78 mol/kg) and Graphene-750 (1.43 mol/kg) had relatively rapid primary adsorbed amounts and store more CO₂ than Graphene-125, CNTs, Graphite and C₆₀. On the contrary, Graphite and C₆₀ stored almost no CO₂. Graphene-125 and SWNTs(2) adsorbed medium amount of CO₂, while the CO₂ adsorbances for MWNTs were lower (around 0.2 mol/kg).

3.1.1.5 Influences of micropore and surface area on CO₂ adsorption capacity

Figure 3.6 shows the micropore volumes calculated by t-plot method for carbon materials as functions of CO₂ capture ability. MWNTs represented a similar micropore

volume ($0.003 \text{ cm}^3/\text{g}$) with CO_2 adsorption capacities around 0.2 mol/kg . The micropore volume of Graphene-125 was $0.025 \text{ cm}^3/\text{g}$, which was almost ten times higher than that of MWNTs. Its CO_2 adsorption amount was 0.83 mol/kg (four times that of MWNTs). This tendency of CO_2 capture ability enhancing, along with increasing amount of micropores, was also detectible for GACs and Graphene-750.

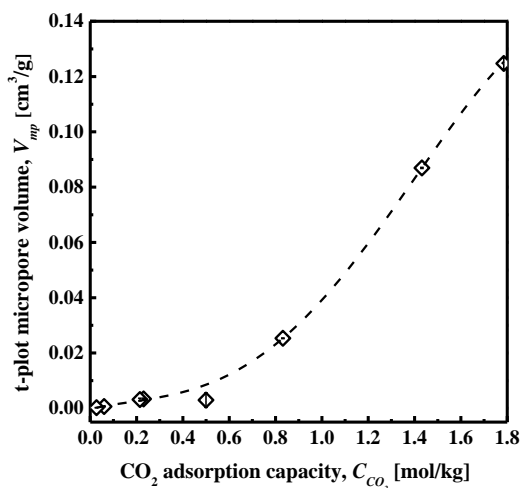


Figure 3.6 Influence of micropore volumes on CO_2 adsorption capacities of carbon materials.

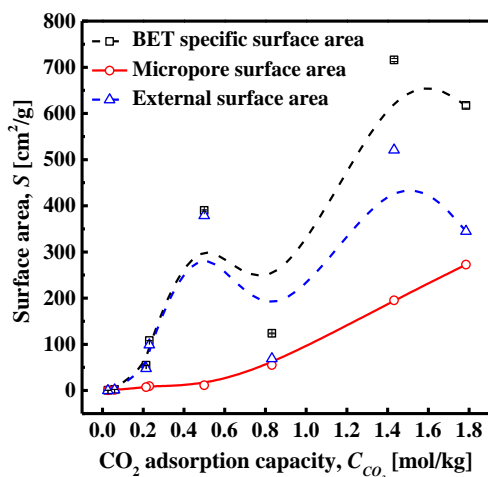


Figure 3.7 Relationships between CO_2 adsorption capacities and BET specific, micropore and external surface areas.

However, the SSAs for these materials in Table 3.2 did not exhibit the same tendency as the effect of the micropore volumes on CO_2 adsorption amount. A complete specific surface area included two parts: internal (micropore) and external surface areas. Figure 3.7 explains the relationships between surface areas and the CO_2 adsorption capacities of carbon materials. The micropore surface areas of carbon materials appeared similar tendency to the micropore volume along with the increasing of adsorbed CO_2 quantities. The tendencies of BET specific surface areas and external

surface areas were very similar, with no clear relationships to the CO₂ adsorbances. Thus, the micropores were dominating the CO₂ physisorption behaviors and capacities of carbon materials. The results of surface areas derived from N₂ isotherms (Figure 3.7) demonstrated that micropore surface area was the more precisely the controller.

3.1.2 Discussions

During physisorption, no chemical reaction occurs between the gas and the carbon adsorbent. However, there are still several preferable sites, namely variety of defects and vacancies, with relative higher energy and activation than the rest spots of the solid surface, which adsorb the gas first [90]. Besides, the sites for adsorption, the morphologies of the carbon materials such as the pore structures and surface curvatures also affect the gas adsorption [153]. These features are the main reasons for the different physisorption behaviors of carbon allotropes with similar crystal structures except fullerenes (Figure 3.2). From the morphology aspect, GACs are porous; graphenes are two dimensional planes; CNTs are sealed cylinders; and Graphite or C₆₀ is similar to a solid particle. The hysteresis loops (Figure 3.3a-b) and pore size distributions (Figure 3.4) for graphenes and CNTs indicated that there were mesopores (2 nm - 50 nm)/macropores (> 50 nm) existing in these materials. Besides, at relatively low pressure ranges, the initial uptakes represented micropores inside graphenes, CNTs, the GACs and Graphene-750 possessed the highest amounts of micropores which led to the higher CO₂ capacities. The existence of hysteresis loops ascribe to the diverse behaviors such as gas condensation within pores and evaporation from pores. The important role for micropores (< 2 nm) during physisorption is obvious. The curve of the micropore volumes or surface areas versus CO₂ capacities (Figure 3.6 or Figure 3.7) reflected that the amounts of micropores dominated the CO₂ uptake capability for sorbents. The CO₂ adsorption uptakes (Figure 3.7) did not scale linearly with the BET specific surface areas. The higher surface area (716 m²/g for Graphene-750) did not correspond to the higher CO₂ adsorptive quantity (GACs with a specific surface area of 617 m²/g). The pore size could correlate to the curvature of the surface, which meant smaller pore size with higher curvature, leading to a higher energy. It is proposed that the pore size smaller than 0.8 nm contributes the most for carbide-derived carbon CO₂ storage abilities [154]. Compared with other materials, GACs and graphenes had smaller average pore sizes (Table 3.3) and own high percentages of pores below 20 nm.

Smaller pore widths of GACs and graphenes contributed to the relatively high micropore volumes and high CO₂ storage abilities. From the active adsorption sites aspect, the adsorption occurs both in the pore and on the surface due to the agglomeration of the powders. Some researchers have calculated the energies of adsorbed sites (internal hollow spaces, interstitial channels, external grooves and surfaces [89]) on CNTs and the energetic sites follow such sequence: E(internal pore) > E(interstitial channel) > E(external groove) > E(external surface) [89, 155]. Hence, if a porous material with micropores is employed as an adsorbent, the micropores are occupied by gas molecules first due to the highest energy of an internal pore.

For the graphenes and sealed ends CNTs in this work, the internal pores did not contribute to the physisorption. Only the external adsorptive sites, such as interstitial channels, external grooves and external surfaces, played important roles in CO₂ adsorption. The different morphologies of graphene and CNTs lead to the diverse interstitial channels. The interstitial channels formed by stacking in graphene are slit-shape pores and larger than the size of CO₂ (0.34 Å), which have small restriction of the powder size for gas adsorption. The configuration of CO₂ adsorption is parallel to the graphene plane to gain a maximum van der Waals contact which is the preferred interaction between π orbital of CO₂ and π ring of graphene [156]. However, the interstitial channels in CNTs only occur in the physisorption process when the minimum outer diameter of the tubes is larger than 1.5 nm. This size is claimed for the homogeneous nanotubes and as well depends on the gas molecule size [89]. This can explain the similar micropore volume values of SWNTs(2) and MWNTs. Because of the tube diameter of SWNTs(2), the external grooves and surfaces determined the specific surface area. Comparing the external and micropore surface areas correlation to CO₂ adsorption capacities of Graphene-125 and SWNTs(2), an indirect proof in Figure 3.7 indicated that the energy of interstitial channel was higher than the external grooves and surfaces. The super low porosity and surface area of Graphite and C₆₀ showed that the physisorption on these two materials should occur mainly on external surface (Table 3.2 and Table 3.3). The low adsorbed N₂ and CO₂ quantities implied that the activation of the external surface site was lower than the rest of the active sites mentioned above (Table 3.2 and Figure 3.3c).

3.2 Conclusions

The CO₂ capacities for GACs (1.78 mol/kg) and graphenes (1.43 mol/kg and 0.83 mol/kg) were the highest among all the carbon materials. Several parameters including micropore volume, average pore size, surface area and morphology affected the CO₂ adsorption ability of different carbon materials. The micropore volume or micropore surface area governed the total CO₂ storage quantity and the external surface area was a less important factor. An indirect proof based on the morphologies and CO₂ adsorption capacities indicated the activation order for diverse adsorbed sites: E(internal pore) > E(interstitial channels) > E(external grooves) > E(external surface). The dominating active sites for GACs were internal pores (micropore), interstitial channels for graphenes, external grooves for SWNTs(2), interstitial channels and external grooves for MWNTs and external surface for Graphite and C₆₀.

Chapter 4 CO₂ chemisorption by doped CaO from wasted eggshell

4.1 CaO-based sorbent extracted from dried eggshell

4.1.1 Experimental methods and characterization procedures

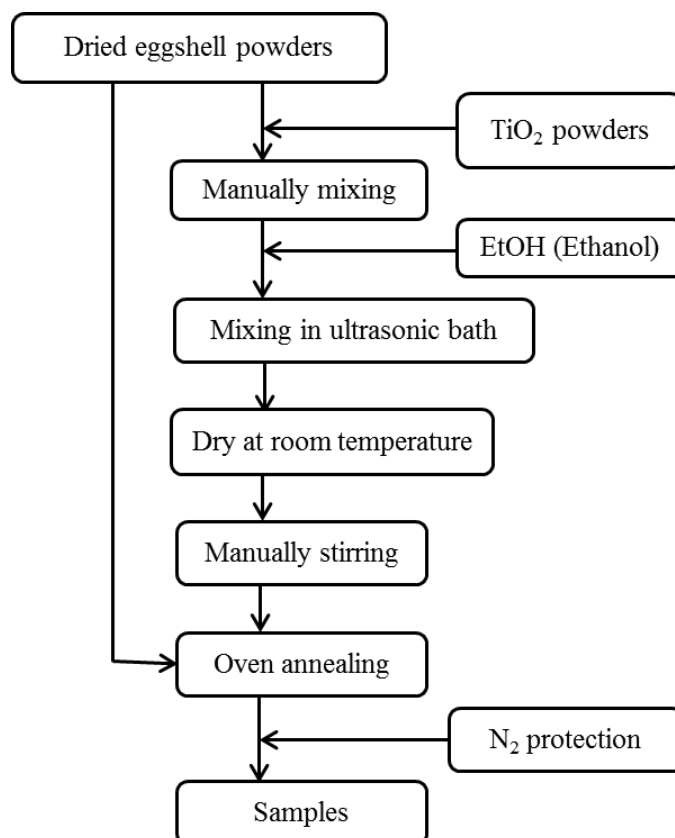


Figure 4.1 Flowchart of producing the CaO-based samples.

Eggshells were collected from domestic wastes. The inner membranes of eggshells were manually peeled and then washed multi times with distilled water. After the cleaning process, eggshells were dried for 48 hours at 100 °C. The collected dried eggshell (dried ES) was ground into specific size range 125 µm - 250 µm. These dried ES powders were calcined in an oven. A flowchart of CaO-based sorbents preparation is described in the Figure 4.1. A heating rate of 3 °C/min was applied to increase temperature from room temperature to target temperature and cooling rate was 6 °C/min. The decarbonation temperatures for experiments were 750 °C, 800 °C, 850 °C, 900 °C, 950 °C, 1000 °C, 1050 °C, 1100 °C and 1200 °C and the holding times were 1 h, 2 h, 3 h and 5 h. Due to the humidity sensitivity of CaO, nitrogen (N₂) was introduced to the decomposition process as a protection gas. The obtained samples after

heating procedures were sealed in separated bottles and preserved in a dryer for further investigations. During the calcination, a decomposition chemical reaction will take place and this process is called decarbonation, desorption or adsorbent regeneration



Based on the chemical reaction Equation 4.1, weight loss of materials after heating at certain temperatures is calculated by the following equation

$$L_w = \frac{W_0 - W_1}{W_0} \times 100 \% \quad (4.2)$$

here L_w and W_1 are the weight loss percentage and the weight of a sample after heating process at certain temperature for specific time. W_0 is the original weight of the sample before heating process.

Several methods were used to characterize the properties of the samples before and after carbonation/decarbonation cycles. The phase analysis of samples was characterized by X-ray diffraction (XRD) with copper (Cu) $K\alpha$ -radiation (D8Discover, 40kV, 40mA) with scanning range from 5 ° to 90 ° and a scanning rate of 2 h/frame. The wavelength of the applied radiation was 1.54 Å.

The morphologies of dried ES, calcined eggshell and calcined eggshell after carbonation/decarbonation were studied by scanning electron microscopy (SEM, Zeiss Supra 25, Germany) at an accelerating voltage of 2 kV. No further sputter coating was applied for observation. Based on the SEM photos, particle diameters and gap sizes of some samples were obtained by using image visualization software Image J.

CO₂ and N₂ adsorption on calcined eggshell were measured by the Micromeritics Accelerated Surface Area and Porosimetry System 2020 (ASAP 2020, America) Analyzer. The calcined eggshell in the form of powder (with sample mass of at least 1 g) was degassed in two stages. In the first stage, sample was degassed under an evacuation phase for 2 hours and later in a heating phase for 12 hours at 350 °C. Dried ES powders were also degassed in two stages. The first stage was the same as the other samples but in the second stage lower temperature 100 °C was applied and heating time was 24 hours. After cleaning, the samples were plugged into the Micromeritics ASAP 2020 Analyzer in a -196 °C liquid N₂ bath. Incrementally dosing of N₂ into adsorbent tubes at different pressures was applied to analyze the physisorption properties. The specific surface areas (SSAs) were calculated by using the Brunauer Emmett and Teller (BET) equation through N₂ adsorption isotherms collected at -196 °C. The pore size

distributions (PSDs) in samples were measured using Barrett-Joyner-Halenda (BJH) analysis following the adsorption of N₂ on the powders. The micropore volumes of eggshell adsorbents were calculated according to the Harkins and Jura equation with t-plot analysis method through N₂ adsorption.

The CO₂ chemisorption of materials was conducted by the same machine Micromeritics ASAP 2020 with different setup (Figure 3.1). CO₂ capture and adsorbent regeneration of ES materials were operated with following parameters: (1) CO₂ capture (carbonation) stage: at the beginning, sample was evacuated at 700 °C for 15 min. Then CO₂ (purity: 99.95 %) was incrementally injected into the sample tube until the pressure of the whole tube system arrived 1 atm at 700 °C. In this stage, CaO-riched samples reacted with CO₂ and formed CaCO₃ phase. The chemical reaction is



(2) adsorbent regeneration (decarbonation) stage: after the CO₂ adsorption stage, the same sample was evacuated at 700 °C for 10 min. Then helium (He) gas was injected into the system and the sample was decarbonated at 850 °C for half an hour (Equation 4.1). One cycle of CO₂ adsorption/desorption (carbonation/decarbonation) includes these (1) and (2) two stages. These two stages were continuously repeating for 1 cycle, 2 cycles, 5 cycles and 10 cycles depending on the purpose of the experiments.

4.1.2 Results and discussion

4.1.2.1 Properties of dried eggshell



Figure 4.2 Normal camera photos of dried ES powders (sieve size: 125 μm - 250 μm).

Regardless of white or yellow color eggshells, the basic compositions of the shell are similar to each other. The obtained dried ES powders after sieving are presented in Figure 4.2 with sieve size of 125 μm - 250 μm. Dried ES (heated at 100 °C for 48 h) was characterized by scanning electron microscopy (SEM). The SEM result (Figure 4.3)

indicates that dried ES composed of relatively solid surface decorated with small pores. The powder size and pore width distributions of dried ES were manually calculated by Image J from SEM photos (Figure 4.4). The average pore size of dried ES was about 173 nm and the average powder size was about 182 μm which was inside the range of 125 μm - 250 μm . The powder size and pore width distributions demonstrated that major powder size and pore diameter were located at relatively narrow ranges around 100 μm to 250 μm and 50 nm to 250 nm, respectively.

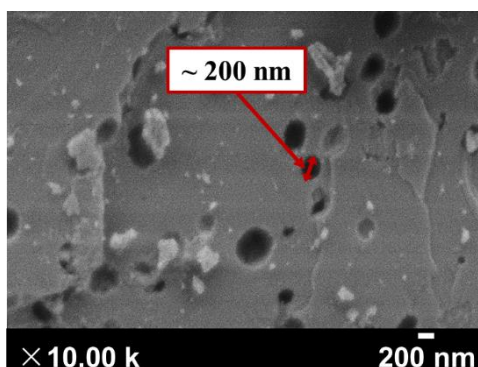


Figure 4.3 SEM morphology of dried ES powders.

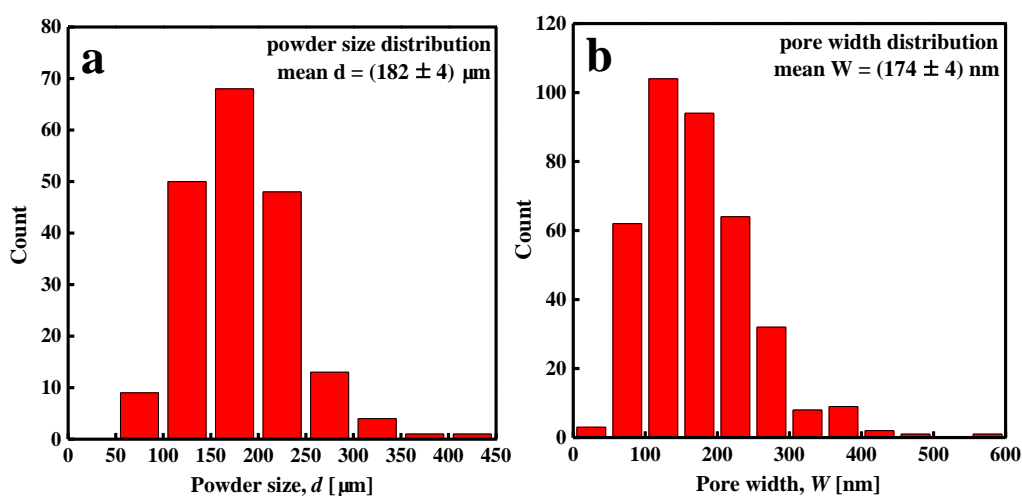


Figure 4.4 The powder size and pore width distributions of dried ES powders calculated by Image J from SEM micrographs.

The XRD diffraction pattern of the dried ES powders is given in Figure 4.5. According to the standard card 01-085-1108 (main peak positions: $2\theta = 29.33^\circ, 48.61^\circ, 64.97^\circ$), the dried ES powders mainly contained CaCO_3 , which was the main Ca source for fabricating CaO-based sorbents.

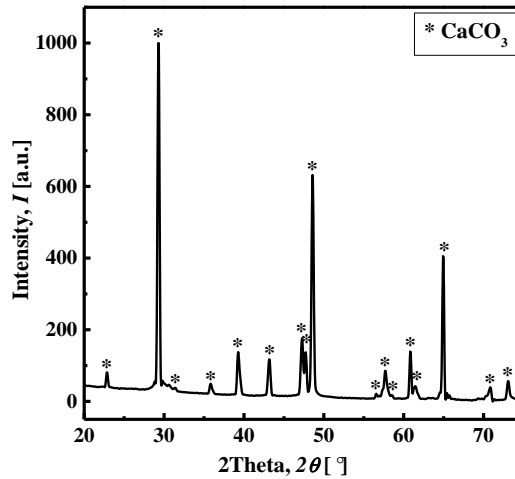


Figure 4.5 The X-ray diffraction pattern for dried ES powders.

4.1.2.2 Calcination parameters

Dried ES powders were heated from 750 °C to 900 °C and held under these temperatures from 1 h to 5 h, denoted as ES(250). First of all, the indirect color changing indicated the decomposition degrees. Figure 4.6 shows the different appearances for ES(250) powders after the treatments at different thermal conditions.

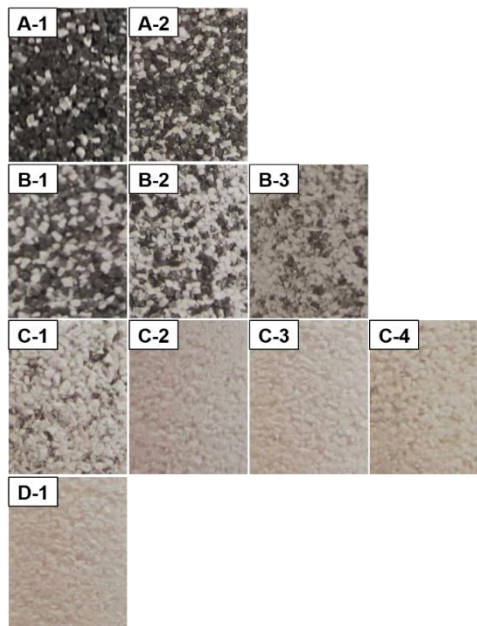


Figure 4.6 Normal camera photos of color changes for ES(250) heated at different parameters: A-1) 750 °C, 1 h; A-2) 750 °C, 5 h; B-1) 800 °C, 1 h; B-2) 800 °C, 3 h; B-3) 800 °C, 5 h; C-1) 850 °C, 1 h; C-2) 850 °C, 2 h; C-3) 850 °C, 3 h; C-4) 850 °C, 5 h; D-1) 900 °C, 1 h.

Black spots and white areas coexisted when the powders were not completely decomposed into CaO (Figure 4.6A, Figure 4.6B and Figure 4.6C-1) and the black spot areas decreased along with increasing temperature and holding time (750 °C: 1 h and

5 h; 800 °C: 1 h, 3 h and 5 h; 850 °C: 1 h). The dark color originated from organic material inside the eggshell which was burned into carbon. Samples heated at 900 °C for 1 h and at 850 °C for more than 1 h (Figure 4.6C-2 to Figure 4.6C-4 and Figure 4.6D) were pure white, indicating the complete removal of protein and other organic materials in eggshell and the primary calcination temperature should be at least 850 °C. The holding time was related to the calcination temperature. In other words, higher decomposing temperature had shorter holding time.

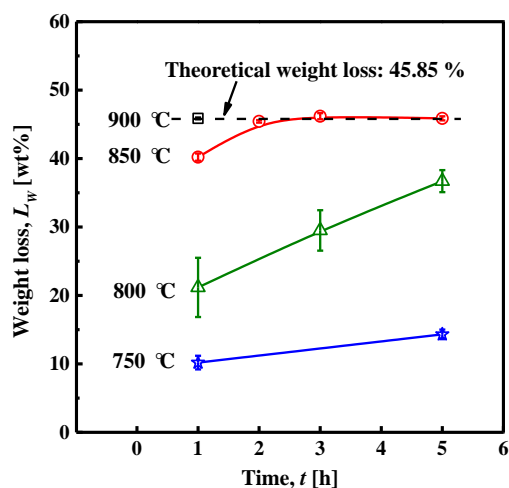


Figure 4.7 The weight losses of ES(250) under different annealing temperatures with various holding time.

The color of the sample can be the first visual indication for obtaining good products or not. But this color changes cannot imply the thorough decomposition reaction from CaCO_3 into CaO . Therefore, weight loss and XRD were necessarily introduced to evaluate the results. The theoretical weight loss calculated from Equation 4.1 for weight loss of CaCO_3 to CaO is 43.97 %. Eggshell mainly consisted of inorganic materials and a small amount of organic materials. Based on the literature [157], the theoretical weight loss for dried ES powders is 45.85 % including the protein burned during the decarbonation procedure. In Figure 4.7, the dash lines indicated the typical weight loss and the rest curves for experimental results. Comparing the samples at different temperatures for 1 h, the decomposition was completed at 900 °C for ES(250) powders. When extending the holding time to 2 h or longer, only samples annealed at 850 °C heating could reach the theoretically calculated weight loss. At low temperature such as 800 °C and 750 °C, CaCO_3 , CaO and organic material coexisted even for longer heating time (Figure 4.7). The weight loss curves demonstrated that best temperature for obtaining pure CaO was above 850 °C. Other than the weight loss, another more

accurate way to estimate the phase composition after decomposition was the XRD patterns.

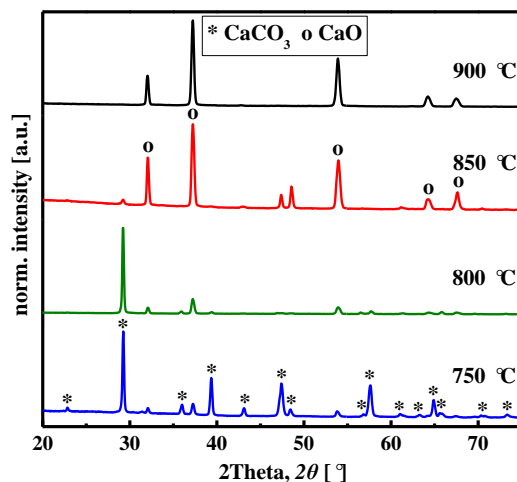


Figure 4.8 The X-ray diffraction patterns of ES(250) at different annealing temperatures for 1 hour.

Figure 4.8 presents the XRD patterns for ES(250) with dried ES powders annealed at different temperatures for 1 h. The standard card number 01-082-1691 for CaO described the main peak positions: $2\theta = 37.39^\circ; 32.21^\circ; 54.08^\circ; 64.37^\circ; 67.48^\circ$. Figure 4.8 demonstrates that the pure CaO could be obtained when the temperature was higher than 850°C with 1 h holding time. Based on CaCO₃ standard card number 01-085-1108 (peak positions: $2\theta = 23.12^\circ; 29.49^\circ; 36.07^\circ; 39.52^\circ; 43.28^\circ; 47.67^\circ; 48.66^\circ; 57.57^\circ$), the powders were mainly consisted of CaCO₃ with heating temperature below 850°C and the main peaks ($2\theta = 29.5^\circ$) of CaCO₃ were pretty sharp in samples heated at 800°C and 750°C for one hour. These results corresponded to the weight loss data in Figure 4.7. No carbon could be obviously observed in the patterns implied that either the crystal of carbon was amorphous or the amount of the carbon was very low.

The compositions of ES(250) under 750°C , 800°C and 850°C for different holding hours are indicated by XRD patterns in Figure 4.9. The different crystal orientations and the large particle size of the ES powder led to the non-identical relative peak intensities of CaCO₃ ($2\theta = 39.52^\circ; 47.67^\circ$ and 48.66°) comparing the ES heated for 1 h with 5 h (Figure 4.9a). The main peak intensity of CaCO₃ ($2\theta = 29.5^\circ$) for 1 h was slightly higher than that for 5 h. When the temperature increased to 800°C , the composition tendency in ES(250) was different in comparison to the tendency in lower temperature. The main peak intensity of CaCO₃ weakened only a little with the heating

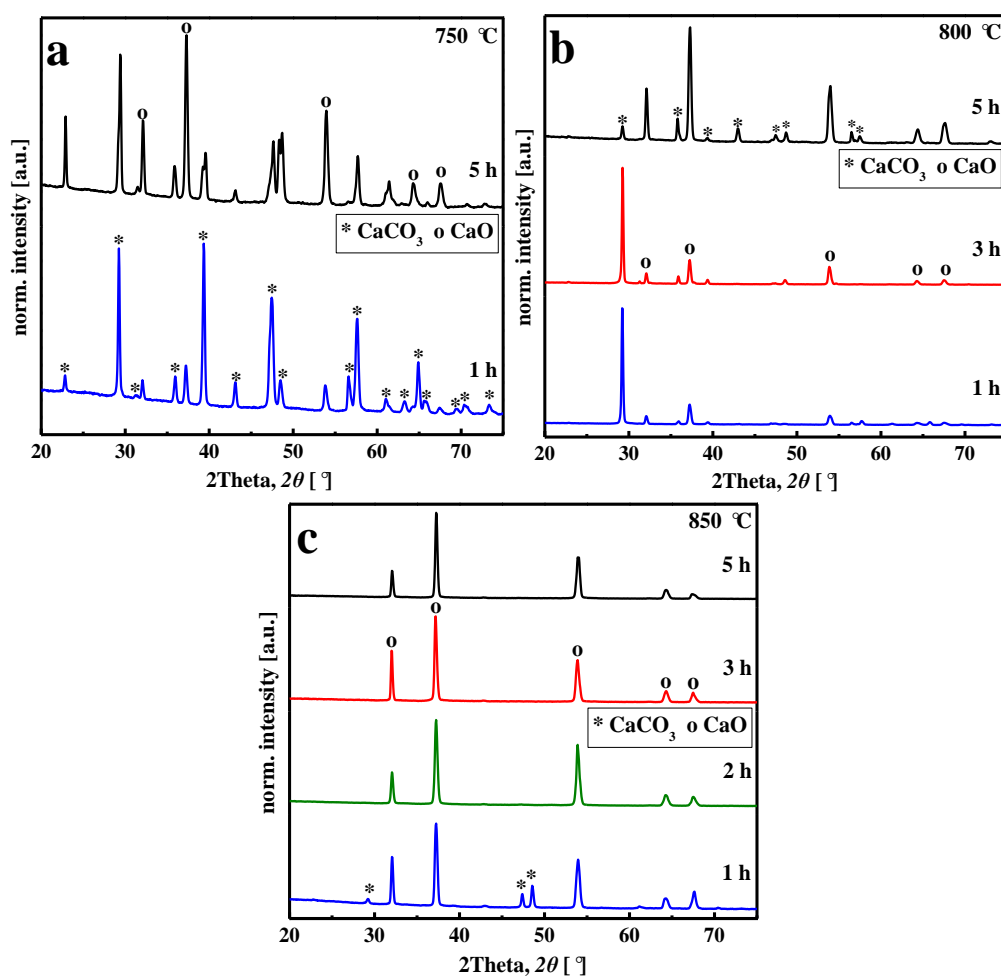


Figure 4.9 The X-ray diffraction patterns of ES(250) heated at 750 °C, 800 °C and 850 °C for different hours.

time elongated from 1 h to 3 h, while this peak intensity decreased dramatically after 5 h heating and formed the sharp peaks of CaO (Figure 4.9b). When the heating temperature arrived around the decomposition temperature of CaCO₃, there was some CaCO₃ left in ES(250) after short heating time (1 h). Pure CaO component could be obtained when holding time was longer than 1 h (Figure 4.9c). Based on the XRD patterns for all samples handled with temperature from 750 °C to 900 °C and holding time from 1 h to 5 h, it was clear that a single CaO component could be produced from the dried ES source with temperature around or above 850 °C and the heat holding time depended on the temperature. 1 hour was enough for a sample heated at 900 °C as compared to heated at 850 °C which needed relatively longer heating period.

ES(250) (heated at 850 °C for 2 h) was characterized by SEM (Figure 4.10). The powder size was in the range of 125 μm to 250 μm as shown in Figure 4.10A. Contrast to the morphology of the dried ES, the surface structure of ES(250) was consisted of

many tunnel-shape gaps with micro rods spreading through the whole surface (Figure 4.10B). The surface of these micro-rods was mainly nonporous with some nano-particles on the top (Figure 4.10C). The tunnel-shape gap size and the micro rod thickness distributions of ES(250) were calculated by Image J from the SEM photos (Figure 4.11). The distributions of the gap size and the micro rods for this ES(250) sample in Figure 4.11 showed that most of the micro rod thicknesses and tunnel-shape gap sizes were in the ranges of 1 μm - 2.5 μm and 0.6 μm - 1.2 μm , respectively. The average thickness of the micro rods was around 1.6 μm with average distance of tunnel-shape gap 0.98 μm , which was the distance from the wall of one rod to the wall of its nearest neighbor.

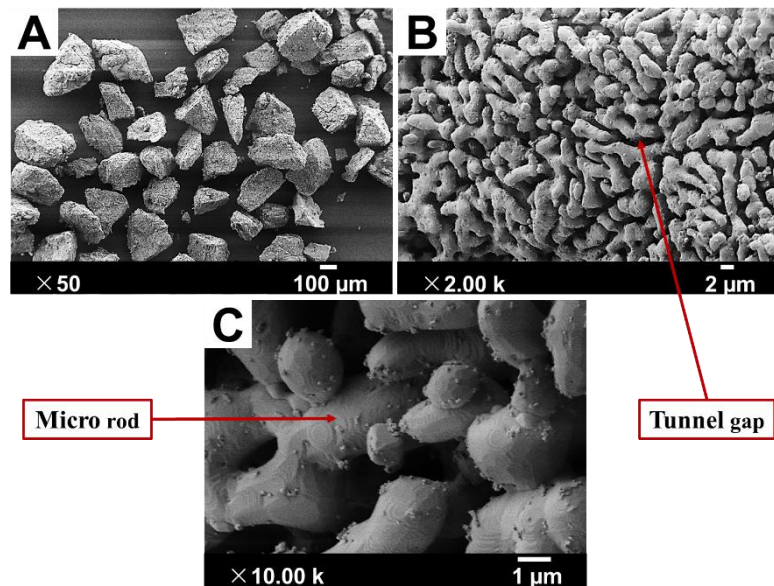


Figure 4.10 The SEM micrographs of ES(250) heated at 850 °C for 2 hours.

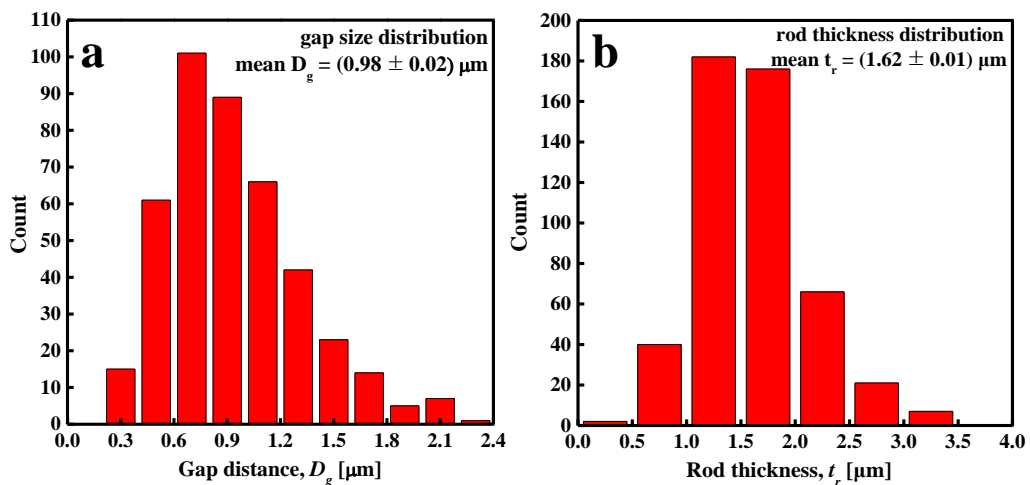


Figure 4.11 The gap size and particle thickness distributions of ES(250) heated at 850 °C for 2 hours calculated by Image J from SEM micrographs.

Adsorption as mentioned in Section 1.2.4 is a surface adsorbing process. Therefore, surface area plays an important role in chemisorption which can affect the CO₂ chemisorption quantity during the carbonation and decarbonation cycles. The weight loss and XRD results pointed out that the annealing temperature should be above 850 °C. Annealing process is always along with sintering effect, which affects the surface area. The BET specific surface area is introduced to further determine the parameters for producing samples. The measured BET specific surface area data are presented in Table 4.1 for ES(250) under three different heating procedures (850 °C for 2 h/5 h and 900 °C for 1 h). Compared to the specific surface area of dried ES(250) heated under 100 °C for 48 h (0.26 m²/g ± 0.003 m²/g), all of the annealed powders possessed much higher surface area values. Decomposing CaCO₃ and releasing CO₂ (Equation 4.1) produced tunnel-shape gaps and some pores (Figure 4.10), which attributed to the increment of the surface area. The surface area decreased with longer holding time and higher annealing temperature due to sintering. Therefore, based on Table 4.1 the suitable decomposing conditions were **850 °C for 2 h**.

Table 4.1 BET specific surface areas for ES(250) under different calcination conditions.

Calcination conditions	ES(250) (m ² /g)
850 °C 2 h	1.97 ± 0.008
850 °C 5 h	0.65 ± 0.010
900 °C 1 h	0.93 ± 0.010

4.1.2.3 N₂ physisorption properties

Figure 4.12 depicts the isotherms and the pore size distributions for ES(250) with decomposition at 850 °C for 2 h. The isotherm was operated with N₂ as test gas at -196 °C. According to IUPAC classification [131], the isotherms (Figure 4.12a) of ES(250) belonged to type IV, which had a certain starting N₂ value under 1 kPa with inversion point or point B and was accompanied by H3 hysteresis loop implying micropores and mesopores inside the powders. Both the adsorption and desorption branches of the H3 hysteresis loop slanted and they were not vertical/horizontal over a broad pressure region. The N₂ adsorbed quantity on the sample was very low around 0.16 mol/kg. The pore size distribution was calculated by the BJH method under N₂ gas at -196 °C with a pore size limitation of 1.7 nm to 300 nm. The result was derived from

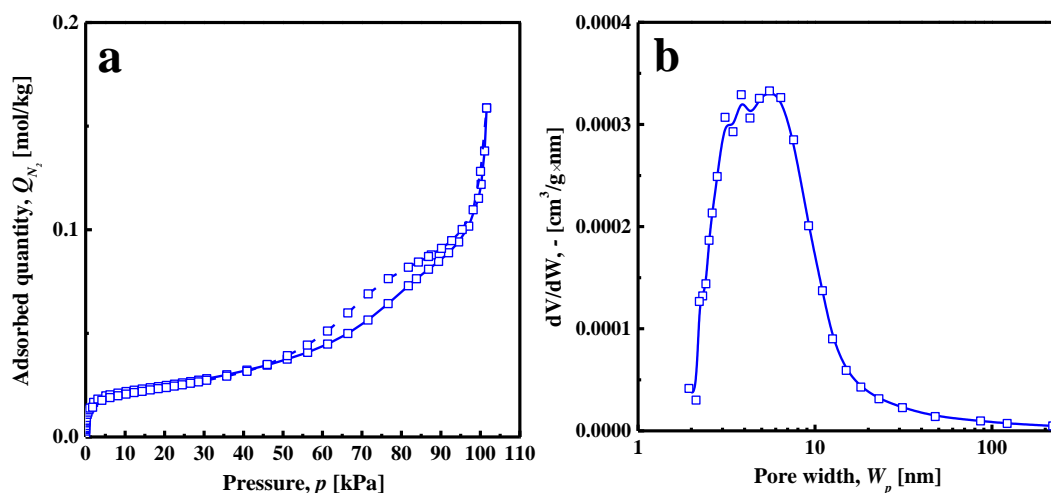


Figure 4.12 Adsorption (solid line) and desorption (dash line) isotherms and pore size distributions with N_2 at -196 °C of ES(250) heated at 850 °C for 2 hours.

the adsorption isotherm branch shown in Figure 4.12b. There was one peak shown in the pore size distribution below 10 nm. This non-sharp peak of ES(250) centered around 4.5 nm with a quite low pore volume (0.00032 cm³/g nm). Although the surface area of ES(250) was higher than the dried ES powders (Table 4.1), the porosity was still low which also could be observed from the surface morphology (Figure 4.10). This little amount of pores was generated during the CO₂ gas flowing outwards.

There were several factors related to the CO₂ adsorption capacity of a material, such as surface area, chemical composition, porosity and pore size, stability of the structure and so on. In order to study the properties of a CO₂ adsorbent and the relationship between physisorption properties and the capacity and stability of chemisorption, the N₂ physisorption features and structure changes of ES(250) powders after cyclic CO₂ adsorption/regeneration were investigated.

The N₂ adsorption/desorption isotherms and pore size distributions at -196 °C of ES(250) after 1, 2, 5 and 10 CO₂ adsorption/desorption cycles are presented in Figure 4.13. The N₂ isotherms of ES(250) (Figure 4.13a) showed to be type IV isotherms having a certain starting N₂ value under 1 kPa and existing point B which were not so obvious in Figure 4.13a. H1 type hysteresis loop was defined for these isotherms and was associated with porous materials. In the H1 hysteresis loop, the adsorption and desorption branches were more likely parallel to each other and nearly vertical in a narrow pressure range. The primary N₂ adsorption and maximum adsorbed quantities were decreasing from the 1st carbonation/decarbonation to the 10th carbonation/decarbonation along with a shrinkage of hysteresis loops. Compared to the

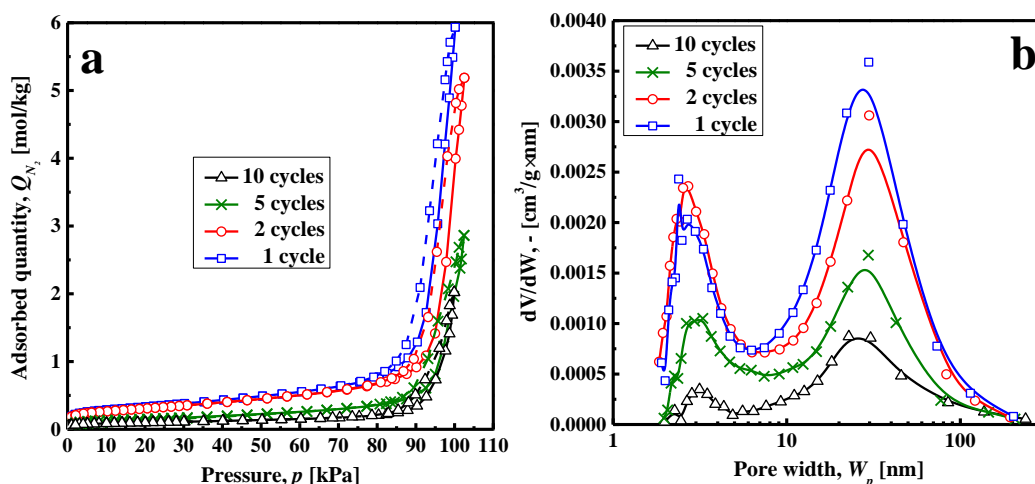


Figure 4.13 Adsorption (solid line) and desorption (dash line) isotherms and pore size distributions with N_2 at -196 °C of ES(250) after 1, 2, 5, 10 carbonation/decarbonation cycles.

N_2 isotherm of the pristine ES(250), the hysteresis loop types were different and the maximum N_2 adsorbed amounts were much higher as well as the initial N_2 uptakes. The hysteresis loop was related to the capillary condensation and occurred in mesopore structures. Figure 4.13b demonstrates the pore size distributions of ES(250). All of the samples displayed bimodal pore size distributions (two peaks) with a fair number of small pores ranging from 1.7 nm to 10 nm and the minority large pores ranging from 10 nm to 100 nm. The peak intensities of ES(250) gradually weakened from the 1st to the 10th carbonation/decarbonation cycle with the peak centers of both small and large pore ranges slightly shifting to lower diameters. This pore size distributions after CO_2 adsorption/desorption cycles were quite different from the original ES(250) powders (Figure 4.12b) with only one peak. The porosities increased dramatically, which implied that the structure of the ES(250) had changed during the process of carbonation/decarbonation. In the next section structure analysis is discussed.

4.1.2.4 Macro-structure

The deteriorating behaviors of isotherms and pore size distributions for ES(250) can be much better determined with the variations of the pore volumes and the average pore diameters after 1, 2, 5, 10 cyclic CO_2 adsorption/desorption in Figure 4.14. The pore volume of pristine sample was quite low 0.006 cm³/g and the mean pore width was around 10 nm. After the first CO_2 carbonation/decarbonation, the total pore volume increased over 0.2 cm³/g, while the pore volumes declined in the following 2, 5 and 10 carbonation/decarbonation cycles. The pore volume after the 10th cycle dropped down

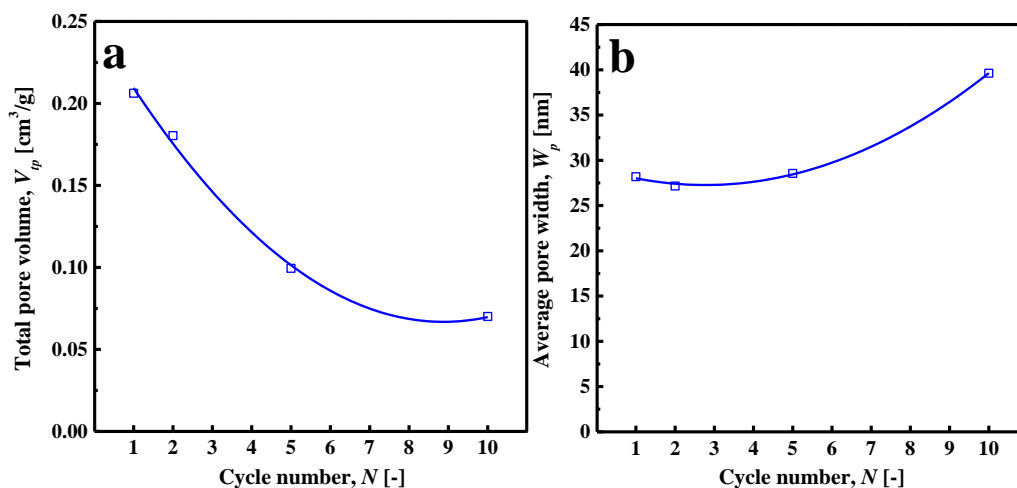


Figure 4.14 Pore volumes and average pore widths of ES(250) after 1, 2, 5, 10 carbonation/decarbonation cycles.

to $0.07 \text{ cm}^3/\text{g}$, which was still 10 times higher than the pore volume of the pristine sample (Figure 4.14a). The average pore diameters after CO_2 adsorption/desorption were enlarged (between 25 nm and 40 nm) in comparison to 10 nm of the adsorbent before carbonation process and the pores tended to grow bigger with more cycles. These pore widths were corresponding to the pore size distributions and demonstrated the higher ratio of pores in range 1.7 nm - 10 nm than in range 10 nm - 100 nm. The growing average pore size was the consequence of losing pores especially the small size pores due to the sintering effect.

This pore structure development was proved by the surface morphologies of the adsorbents. Figure 4.15 shows the SEM micrographs of ES(250) after 1 and 10 cycles of CO_2 adsorption/desorption (Figure 4.15C-F) as well as the sample conducted under the same process with He instead of the CO_2 gas (Figure 4.15A, B), in order to analyze if operation parameters would change the structure of ES(250) particles. The sample which went through the adsorption/desorption cycle with He gas as the chemisorption adsorbate remained the same surface structure as the pristine ES(250) powders (Figure 4.10), while there were a lot of nano pores appearing on the surface and the inner of ES(250) after 1 and 10 calcination and carbonation cycles (Figure 4.15D, F). The inner part of the particle was not as dense as on the surface after the 1st and the 10th cycle such as the morphologies of a cross section after the 1st and the 10th CO_2 capture and adsorbent regeneration process in Figure 4.15D and Figure 4.15G. The tunnel-shape gaps either dramatically narrowed or disappeared in ES(250) after the 10th cycle and the micro rods were connected to each other and formed into large particles

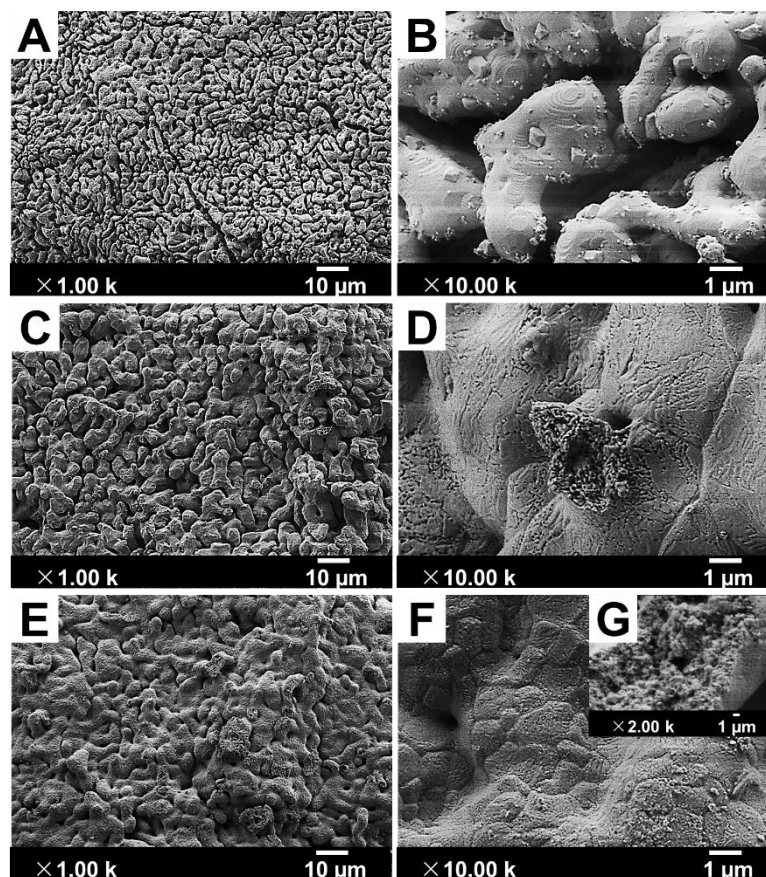


Figure 4.15 SEM micrographs of ES(250) powders after different carbonation/decarbonation cycles: (A, B) 1 cycle without CO₂ reaction, (C, D) 1 cycle and (E, F) 10 cycles.

(Figure 4.15A, C, E). The merging of the micro rods also showed that severe sintering happened during the CO₂ adsorption/desorption process. This process not only yielded to a large amount of pores but also increased the sintering effect in comparison between the cycle with He and the cycle with CO₂ in Figure 4.15(A-D).

4.1.2.5 Chemical reaction rate

Pores, macro-structure and surface area are related to each other and they play an important role in the chemisorption in both the adsorbent reaction kinetics, CO₂ adsorption capacity as well as the CO₂ chemisorption stability. After the discussion of the physisorption properties of ES(250) before and after chemisorption, the chemisorption behaviors during various CO₂ adsorption/desorption cycles are studied in this section.

The 1st, 2nd, 5th and 10th CO₂ carbonation and reaction rate isotherms are presented in Figure 4.16 for ES(250). The uptakes augmented rapidly at low pressure range before reaching a plateau. The CO₂ adsorbed value of the 1st and the 2nd carbonations continued

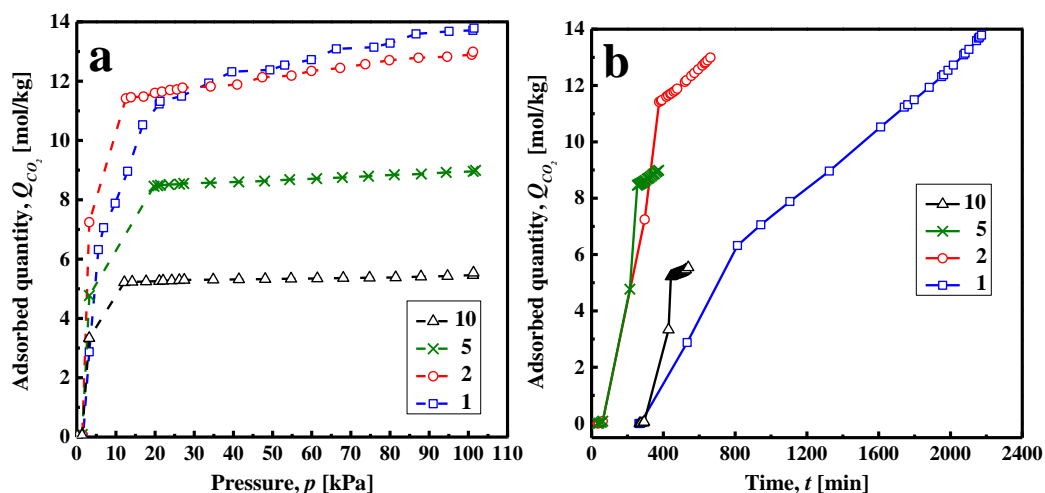


Figure 4.16 The 1st, 2nd, 5th and 10th carbonation (700 °C, 100 % CO₂) and chemical reaction rate isotherms of ES(250).

to climb up after turning point, while it was much flatter for the 5th and the 10th carbonations on the isotherms after the turning point (Figure 4.16a). The pressures of the turning points shifted from 20 kPa to 10 kPa (in the order of the 1st, 5th and 10th carbonation) and the turning point pressure of the 2nd carbonation isotherm was close to that of the 10th carbonation isotherm. The CO₂ adsorbed quantities of ES(250) at 1 atm decreased along with more carbonation/decarbonation cycles. The quick CO₂ adsorption at low pressure was the result of the different reaction rates. The kinetics reaction rate was similar to the carbonation isotherms in Figure 4.16a with two steps and a turning point in the curve. Generally, there are two step-reaction rates for gas-solid chemical reaction: instinct surface controlled kinetic reaction (Step I) and diffusion controlled slow reaction (Step II) [158-160]. The kinetic reaction rate with short instinct surface reaction (Step I) and relatively long diffusion controlled reaction regime (Step II) of the 1st cycle was different from the behaviors of the rest cycles, which were dominated by the Step I (instinct surface reaction rate) (Figure 4.16b). The reaction rate of Step I increased dramatically after the 1st cycle and maintained almost constant through the whole cyclic CO₂ adsorption/desorption, while the diffusion rate of Step II were similar for all of the cycles. Due to the chemical reaction rate control by Step I in the cycles after the 2nd CO₂ chemisorption process, the whole adsorption period shortened. The Step I reaction also controlled the majority of the maximum CO₂ adsorption capacity. As the SEM results in Figure 4.15, after the first carbonation/decarbonation cycle, a lot of pores were produced and this is the reason for the domination change from Step II to Step I, which could be proved by the surface

area development.

Table 4.2 BET specific surface areas of ES(250) after 0, 1, 2, 5, 10 carbonation/decarbonation cycles.

Cycles	ES(250) (m ² /g)
0	1.97 ± 0.01
1	26.61 ± 0.001
2	24.72 ± 0.02
5	12.23 ± 0.02
10	8.05 ± 0.06

Table 4.2 sums the BET specific surface areas for the pristine ES(250) and the samples after 1, 2, 5 and 10 CO₂ chemisorption/regeneration processes. The BET surface area 26.61 m²/g after the 1st cycle was 13 times higher than the surface area for the ES(250) before CO₂ chemisorption, which led to the kinetic rate change in Figure 4.16b. However, the surface areas were reduced along with more cycles and after the 10th adsorption/desorption the surface area was cut down to 8.05 m²/g, which was still 4 times larger than that of the original ES(250). The CO₂ chemisorption took place first on the surface and CO₂ must penetrate through CaCO₃ layer (product of chemisorption) after finishing surface reaction. Thus, due to the very low surface area of the pristine ES(250), Step II played a more important role in CO₂ adsorption.

4.1.2.6 CO₂ adsorption stability

A good adsorbent should provide high CO₂ adsorption capacity, short CO₂ separation time and chemical stability. For the study of the CO₂ adsorption stability, the following equation is used to calculate the adsorbed CO₂ uptake.

$$C_{CO_2}^n = \frac{n_{CO_2}^n}{M} \text{ (mol/kg)} \quad (4.4)$$

$C_{CO_2}^n$ is the CO₂ capacity in mol/kg in the nth cycle, $n_{CO_2}^n$ is the reacted CO₂ amount in mol in the nth cycle, and M is the mass of the sample in kg. The CaO carbonation conversion is applied to evaluate the chemisorption stability and is calculated with formula

$$X_n = \frac{n_{CO_2}^n}{MY/56} \times 100 \% \quad (4.5)$$

X_n is the carbonation conversion of CaO after n cycles, Y is the percentage of CaO in the sample. $n_{CO_2}^n$ and M is the same as in Equation 4.4.

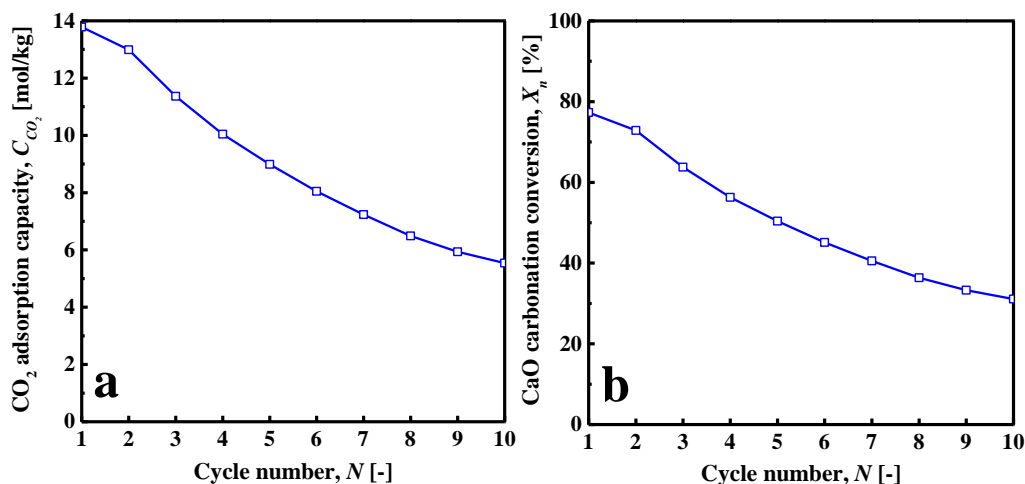


Figure 4.17 The CO₂ adsorption capacities and CaO carbonation conversions during carbonation (700 °C, 100 % CO₂)/decarbonation (850 °C, 100 % He) cycles of ES(250) powders heated at 850 °C for 2 hours.

The CO₂ adsorption capacity gradually diminished after each adsorption/desorption cycle and after the 10th carbonation the capacity of ES(250) was less than half of the initial CO₂ capacity (Figure 4.17a). This can be the results of the sintering with the loss of the new born pores after the 1st carbonation/decarbonation cycle. The efficiency of reacted CaO was quite high at the beginning with around 77 % (Figure 4.17b) higher than the conversion (0.45 - 0.71) for CaO sorbents from limestone [161, 162]. However, the CaO carbonation conversion decayed below 35 %. As the morphologies shown in Figure 4.15(C, D), after the 10th CO₂ chemisorption, ES(250) lost the tunnel-shape gaps with a fusion of the micro rods and the pores from the first carbonation. The consequence of this loss was the decrease of the efficient CaO for CO₂ adsorption. According to the study of Diego Alarez et al [163], a critical CaCO₃ product layer thickness around 50 nm is acceptable. The average thickness of the rods in ES(250) was about 1.6 μm and they merged into much larger ones after the carbonation/decarbonation cycles. The inner CaO cannot participate in the CO₂ chemisorption due to the formation of CaCO₃ product layer. This leads to the deterioration of both the adsorbed CO₂ quantities and the CaO carbonation conversions.

4.2 Doped CaO with eggshell as source

4.2.1 Experimental method

According to the study of the ES(250), the reasons of reduction in CO₂ chemisorption stability were the loss of the pores, surface area and the fusion of rods. In order to stop

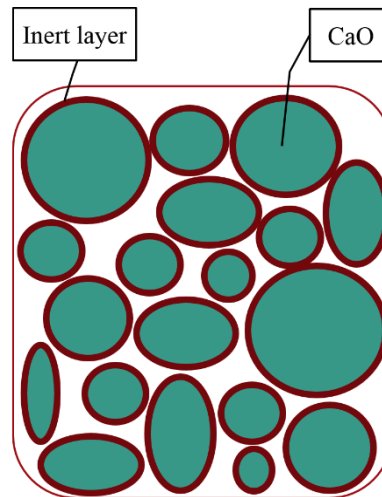


Figure 4.18 Scheme of the experimental concept.

this sintering effect, TiO_2 powders were introduced into the system to synthesize a CaO-rich $CaO/CaTiO_3$ sorbent. An experimental concept scheme is shown in Figure 4.18. Due to the chemical stability of $CaTiO_3$ under high temperature, synthesis of $CaTiO_3$ can function as an inert layer to separate the CaO particles, allowing CO_2 to pass through and react with CaO, as well as hindering the sintering effect on the CaO particles during carbonation/decarbonation cycles. For the production of $CaTiO_3$, there are two possible chemical reactions taking place



Synthesis of $CaTiO_3$ and decomposition of $CaCO_3$ happened at the same time under the same heating environment. Two kinds of TiO_2 powders with sizes of 27 nm (T(27)) and 44 μm (T(44)) and eggshell powders with size of 125 μm - 250 μm were used as $CaTiO_3$ and CaO sources. Eggshell powders and TiO_2 powders were mixed first in a dry way, then ethanol was introduced into the system for a wet mixing to make sure that the mixture was homogeneous. The wet mixture was then dried at room temperature until a constant weight was achieved and loaded into an oven for annealing process. The whole sample production procedure is shown in Figure 4.1. The temperature rate of 3 $^{\circ}C/min$ was applied for heating the prepared mixtures from room temperature to a target temperature and cooling rate for the decarbonation was 6 $^{\circ}C/min$ to room temperature. The setting temperatures for experiments were 750 $^{\circ}C$, 800 $^{\circ}C$, 850 $^{\circ}C$, 900 $^{\circ}C$, 950 $^{\circ}C$, 1000 $^{\circ}C$, 1050 $^{\circ}C$, 1100 $^{\circ}C$ and 1200 $^{\circ}C$ and the holding times were 1 h, 2 h, 3 h and 5 h. Due to the humidity sensitivity of CaO, the synthesis was

operated under the nitrogen gas protection. And the target samples obtained after heating procedures were sealed in separated bottles and preserved in a dryer for further investigations.

Table 4.3 Weight ratios and names of the samples.

Sample name	TiO ₂ (g)	ES (g)	TiO ₂ (wt %)
ES	0.00	3.00	0
5T/ES	0.15	2.85	5
10T/ES	0.30	2.70	10
15T/ES	0.45	2.55	15
20T/ES	0.60	2.40	20
30T/ES	0.90	2.10	30
40T/ES	1.20	1.80	40

All obtained samples were named with basic information of original two sources and the weight ratio of TiO₂ introduced to the mixture (Table 4.3). For example, 10T(27)/ES(250) meant that TiO₂ and eggshell powders weight ratio was 10 to 90 and the particle sizes for TiO₂ and dried ES powders were 27 nm and 125 μm - 250 μm, respectively. The characterization methods were the same as described in Section 4.1.1.

4.2.2 Results and discussion

4.2.2.1 Calcination parameters

Although the decarbonation of ES(250) powders had been investigated and discussed, the decomposition of TiO₂/ES was conducted at the same time to study the synthesis of CaTiO₃ and the influence of TiO₂ on decarbonation of eggshell powders. To compare with ES(250) sample, a mixture of T(27) and dried ES (125 μm - 250 μm) was chosen with 10 : 90 weight ratio between TiO₂ and eggshell, and the relative sample was named as 10T(27)/ES(250). First of all, the color changes can indicate the decomposition levels. Figure 4.19 shows the powder colors for 10T(27)/ES(250) powders after undergoing various temperatures (750 °C to 900 °C) for different holding hours (1 h to 5 h). Despite the various powder colors for ES(250) with black/white and 10T(27)/ES(250) with grey/white because of the TiO₂ powders, the color changing trends for both systems were close to each other (Figure 4.6 and Figure 4.19). The non-white areas were reduced with longer heating time and higher heating temperature (Figure 4.19a, b and Figure 4.19c-1). The powders turned out completely white at

850 °C for 2 h to 5 h (Figure 4.19c-2 to Figure 4.19c-4) and at 900 °C for 1 h (Figure 4.19d-1).

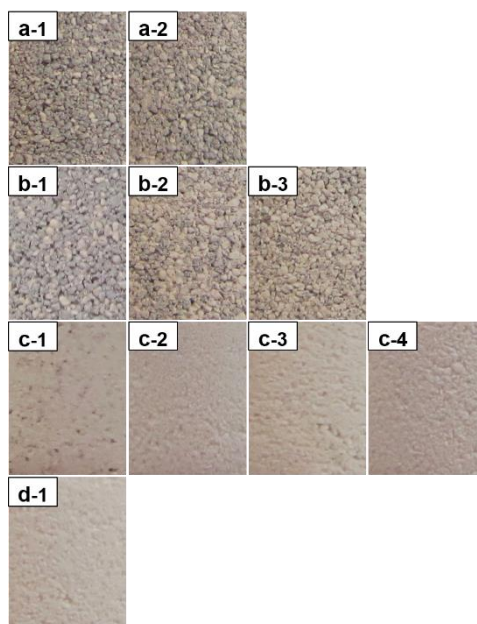


Figure 4.19 Normal camera photos of color changes for 10T(27)/ES(250) powders heated at different parameters: a-1) 750 °C, 1 h; a-2) 750 °C, 5 h; b-1) 800 °C, 1 h; b-2) 800 °C, 3 h; b-3) 800 °C, 5 h; c-1) 850 °C, 1 h; c-2) 850 °C, 2 h; c-3) 850 °C, 3 h; c-4) 850 °C, 5 h; d-1) 900 °C, 1 h.

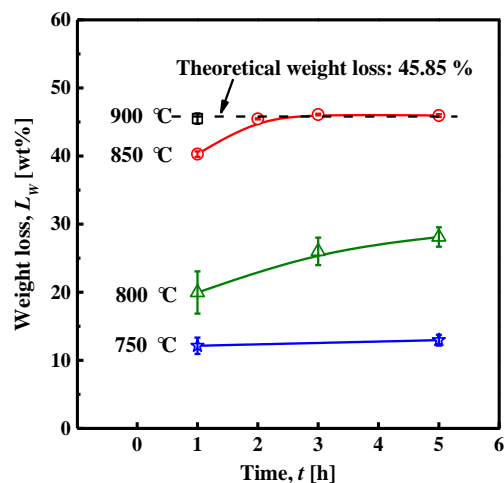


Figure 4.20 Weight losses of 10T(27)/ES(250) powders under different annealing temperatures with various holding time.

Decomposition led to the weight loss of the mixture based on the chemical reaction Equation 4.1. The weight losses of 10T(27)/ES(250) powders were analyzed and demonstrated in Figure 4.20. The dash line indicates the typical weight loss (45.85 %) and the rest dots were experimental results. In comparison to the samples kept for 1 hour at different temperatures, the decomposition was completed at 900 °C for

10T(27)/ES(250) powders. When extending the holding time to 2 hours or longer, only samples annealed at 850 °C could reach the typical calculated weight loss. At low temperature such as 800 °C and 750 °C, CaCO₃ existed even for longer heating. In contrast to the weight loss results in Figure 4.20 by the weight loss for ES(250) in Figure 4.7, the decomposition rates of 10T(27)/ES(250) powders at 750 °C and 800 °C were a little lower than that of ES(250).

The higher temperatures (850 °C and 900 °C) eliminated such differences. This phenomenon was produced by introducing the component TiO₂ into the mixture system. During the heating, chemical reactions of Equation 4.6 and Equation 4.7 took place and formed some amount of CaTiO₃. When CaCO₃ decomposed into CaO and CO₂ (Equation 4.1), CO₂ was needed to transfer from the inner of a particle to the outside edge (CaTiO₃ and TiO₂) and then released into environment. However, the mobility rate of CO₂ was related to the temperature and the medium. At low temperature, the permeability of CO₂ was slower than that at high temperature. Therefore, the weight loss of 10T(27)/ES(250) powders was slower than that of ES(250) powders.

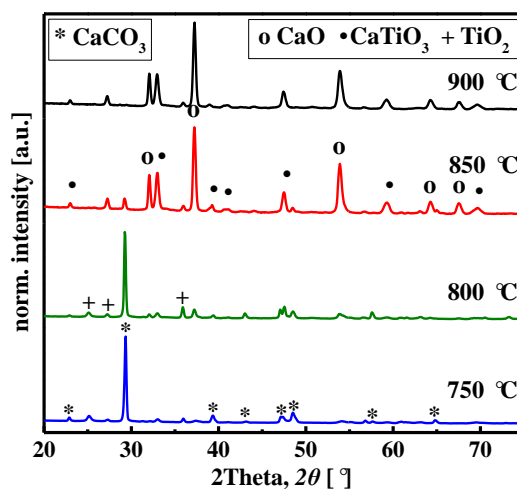


Figure 4.21 The X-ray diffraction patterns of 10T(27)/ES(250) powders at different annealing temperatures for 1 hour.

The phase analysis for 10T(27)/ES(250) at different annealing parameters was characterized by XRD and illustrated in Figure 4.21. The standard card number 01-082-1691 for CaO presented the main peak positions: $2\theta = 37.39^\circ$; 32.21° ; 54.08° ; 64.37° ; 67.48° . Figure 4.21 indicates that the pure CaO can be obtained when the temperature reached 900 °C with 1 hour heat holding. Based on the CaCO₃ standard card number 01-085-1108 (peak positions: $2\theta = 23.12^\circ$; 29.49° ; 36.07° ; 39.52° ; 43.28° ; 47.67° ; 48.66° ; 57.57°), the powders mainly consisted of CaCO₃ with heating

temperatures at 750 °C as well as 800 °C. The main peaks ($2\theta = 29.5^\circ$) of CaCO_3 were pretty sharp in the samples at these temperatures for one hour. These results corresponded to the weight loss data in Figure 4.20. The decrease tendencies of CaCO_3 major peaks in 10T(27)/ES(250) samples were similar to the variation of ES(250) (Figure 4.8). CaTiO_3 increased very fast as the temperature went up to 850 °C and 900 °C (standard card number 01-089-8033 with peak positions: $2\theta = 23.22^\circ$; 32.85° ; 33.08° ; 33.29° ; 47.47° ; 58.79° ; 58.96° ; 59.25° ; 59.36°). But TiO_2 powders did not completely react with CaO at high temperatures. There were still little amount TiO_2 observed in Figure 4.21 at 850 °C and 900 °C. XRD curves demonstrated that temperature had high influence on the decomposition of CaCO_3 and the synthesis of CaTiO_3 .

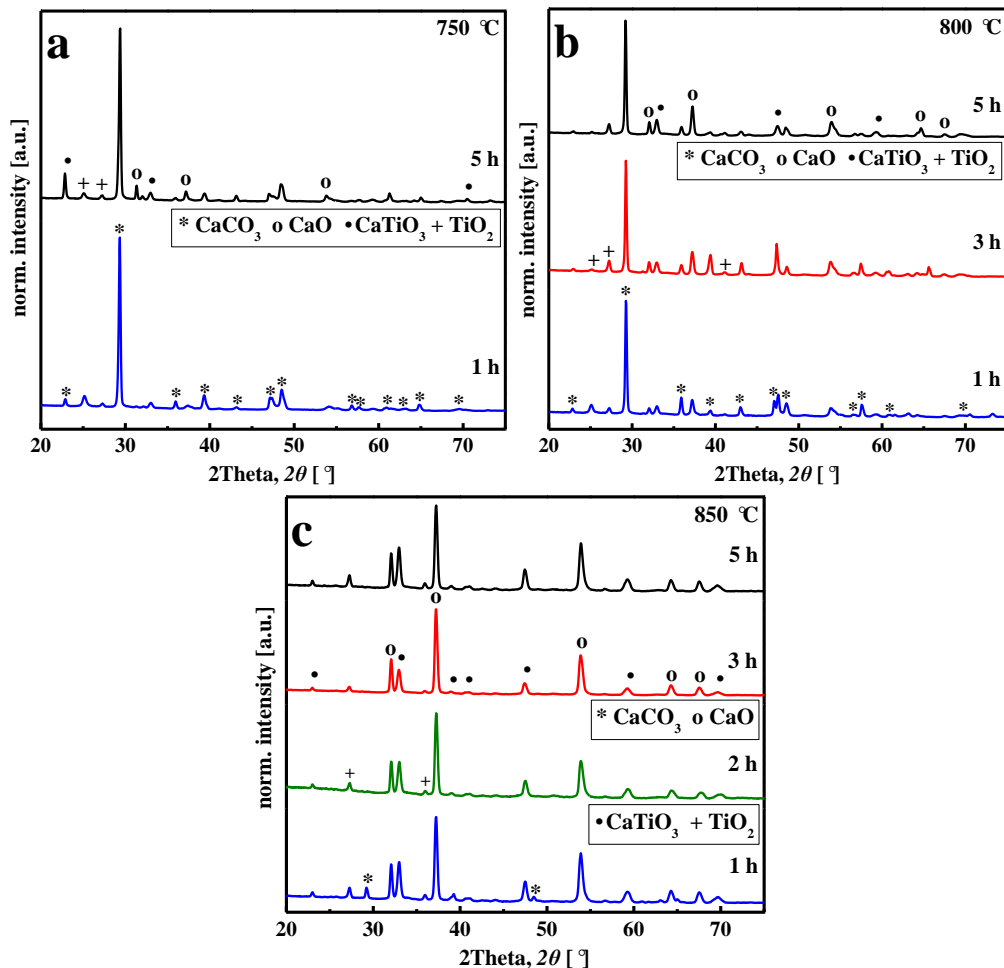


Figure 4.22 The X-ray diffraction patterns of 10T(27)/ES(250) powders heated at 750 °C, 800 °C and 850 °C for different hours.

The phase development of 10T(27)/ES(250) under 750 °C, 800 °C and 850 °C for different holding hours were indicated by XRD patterns in Figure 4.22.

10T(27)/ES(250) had similar main peak intensities of CaCO_3 for both 1 h and 5 h at 750 °C. In contrast to the short heating period, obvious CaTiO_3 peaks formed after the sample heated at 750 °C for 5 h (Figure 4.22a). On the contrary to ES(250) (Figure 4.9b), the compositions of 10T(27)/ES(250) seemed to change slightly and a relative high ratio of CaCO_3 existed in the mixture powders (Figure 4.22b) with increasing the temperature to 800 °C and holding time from 1 h to 5 h, which agreed with the weight loss results (Figure 4.20). When the heating temperature reached around the decomposing temperature of CaCO_3 , there was some CaCO_3 left and obvious CaTiO_3 peaks appeared in the 10T(27)/ES(250) sample after short heating time (1 h) (Figure 4.22c). CaCO_3 component completely disappeared when the holding time was longer than 1 h. Most of the TiO_2 reacted with CaO/CaCO_3 and transformed into CaTiO_3 . Little percentage of TiO_2 remained without reacting with CaO no matter how long the heating last at 850 °C. Based on the XRD patterns for all samples annealed with temperature from 750 °C to 900 °C and holding time from 1 h to 5 h, it was clear that single CaO component could be produced with temperature around or above 850 °C and the heat holding time depended on the temperature. 1 hour was enough for a sample heated at 900 °C compared to heat at 850 °C, which needed relatively longer heating period. For 10T(27)/ES(250), activated reaction between TiO_2 and CaO/CaCO_3 happened at 850 °C or above.

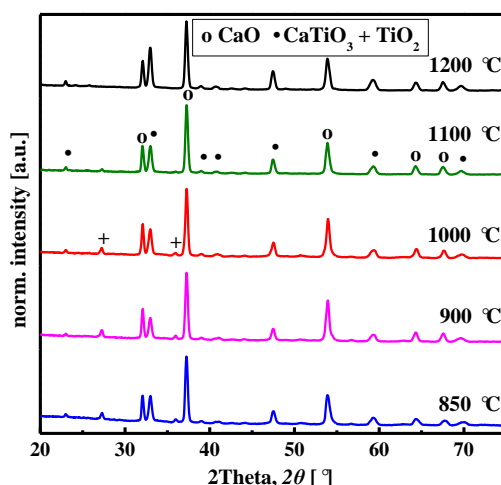


Figure 4.23 The X-ray diffraction patterns of 10T(27)/ES(250) powders heated from 850 °C to 1200 °C for 2 hours.

A further thermal investigation between temperature and the CaTiO_3 synthesis was conducted with heating temperature over 900 °C for 2 hours. The XRD patterns

(Figure 4.23) shows that from 850 °C to 1000 °C there were little amount of TiO₂ remained, while TiO₂ disappeared with the annealing temperatures of 1100 °C and 1200 °C, which contributed to the increase of ions mobility. The surface of the eggshell particles reacted first with TiO₂. After that, the solid state chemical reaction relied on the ion permeation from inner to outside. Relatively high temperature enhanced Ca²⁺ ion to move to the outside layer for further reaction.

A rule for selecting CO₂ adsorbent is high surface area, which corresponds to the CO₂ adsorption uptake. A two-phase system of CaO/CaTiO₃ could be reached with the reaction temperature higher than 1000 °C. However, the structures were different in association with the crystal growths of CaO and CaTiO₃ after thermal process at 850 °C, 1000 °C and 1200 °C (Figure 4.24). Part of the CaTiO₃ layer detached away from ES(250) surface for 10T(27)/ES(250) heated at 1200 °C (Figure 4.24E). The CaTiO₃/TiO₂ and CaO particles enlarged from 850 °C to 1200 °C (Figure 4.24B, D, F). The particle size of CaTiO₃(TiO₂) at 1200 °C was 3 to 4 times larger than that at 850 °C, while the CaO particles at 1200 °C was around 10 times bigger than that at 850 °C.

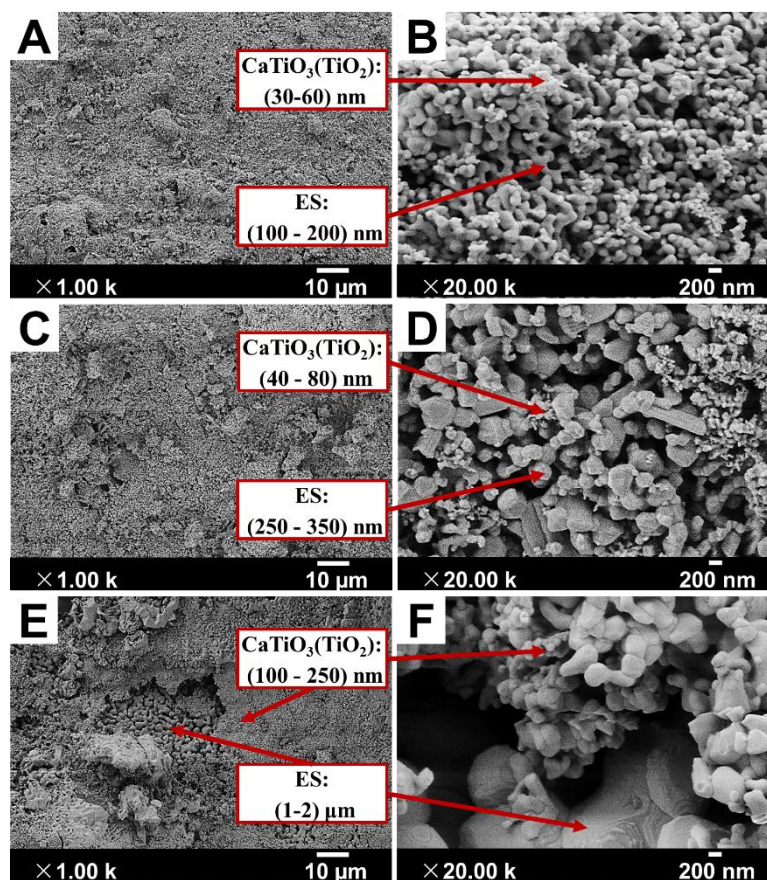


Figure 4.24 SEM morphologies of 10T(27)/ES(250) powders heated at (A, B) 850 °C, (C, D) 1000 °C and (E, F) 1200 °C for 2 hours.

Comparing the particle size of $\text{CaTiO}_3(\text{TiO}_2)$ and CaO at $1000\text{ }^\circ\text{C}$ to the samples heated at $850\text{ }^\circ\text{C}$, the sizes did not change so dramatically. CaTiO_3 prevented the sintering effect and crystal growth of CaO in some degree, while the CaO rod thickness was around $1.6\text{ }\mu\text{m}$ in ES(250) (Figure 4.10 and Figure 4.11b). When the temperature was higher than $1000\text{ }^\circ\text{C}$, the aggregation and sintering phenomena became much more obvious.

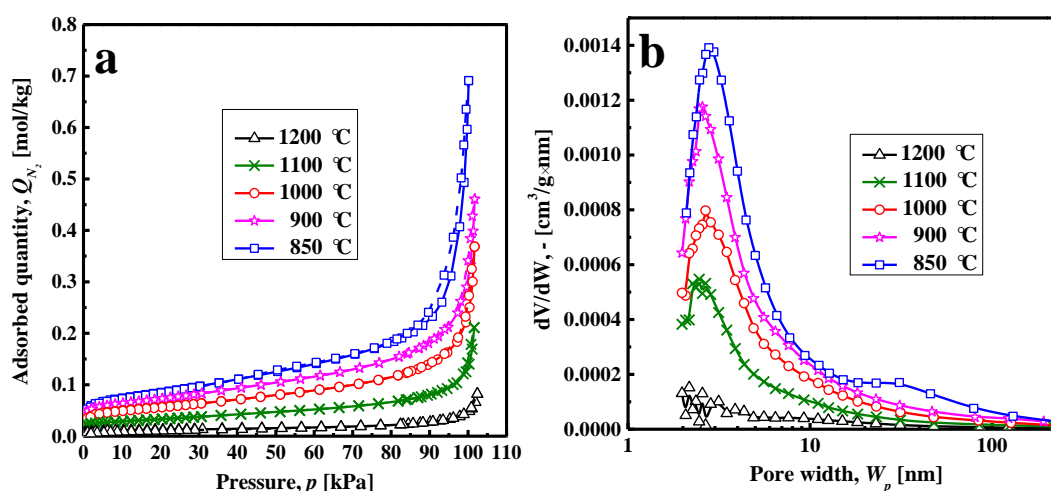


Figure 4.25 Adsorption (solid line) and desorption (dash line) isotherms and pore size distributions with N_2 at $-196\text{ }^\circ\text{C}$ of 10T(27)/ES(250) heated at $850\text{ }^\circ\text{C}$, $900\text{ }^\circ\text{C}$, $1000\text{ }^\circ\text{C}$, $1100\text{ }^\circ\text{C}$ and $1200\text{ }^\circ\text{C}$ for 2 hours.

Aggregation can always change the powder structures to some extent and affect the physisorption properties of the samples. Figure 4.25 illustrates the isotherm curves and the pore size distributions for 10T(27)/ES(250) annealed from $850\text{ }^\circ\text{C}$ to $1200\text{ }^\circ\text{C}$. All of the N_2 adsorbed quantities, hysteresis loops and initial N_2 uptakes were either reduced or shrank from $850\text{ }^\circ\text{C}$ to $1200\text{ }^\circ\text{C}$. According to the IUPAC classification [131] the isotherms in Figure 4.25a pertained to type IV, with a large starting N_2 value under 1 kPa and existing inversion point accompanied by H1 hysteresis loops ($850\text{ }^\circ\text{C}$ to $1200\text{ }^\circ\text{C}$). In the H1 hysteresis loop, the adsorption and desorption branches were more likely parallel to each other and nearly vertical in a narrow pressure range. The shrinking hysteresis loops implied the extinguishing of pores. N_2 gas had been applied to analyze the pore situation. However, there was a detection limit with the BJH calculation for pore sizes between 1.7 nm and 300 nm. The results derived from BJH adsorption branches shown in Figure 4.25b indicated that 10T(27)/ES(250) had relatively narrow (1.7 nm to 15 nm) ($850\text{ }^\circ\text{C}$ to $1200\text{ }^\circ\text{C}$) and broad (15 nm to 230 nm) ($850\text{ }^\circ\text{C}$) pore size distributions. At narrow pore size distribution area, the peaks

centered around 2.5 nm and the pore volumes reduced distinctively from 850 °C to 1200 °C, at which almost no peaks could be observed. The sample at 850 °C also showed a small peak at the broad pore size distribution area with a peak center around 31 nm. The pores in 10T(27)/ES(250) powders consisted of two parts: (1) interstices formed by CaTiO₃(TiO₂); and (2) pores formed by CO₂ flowing outwards.

Table 4.4 BET specific surface areas for 10T(27)/ES(250) under different annealing temperatures for 2 hours.

Calcined conditions	10T(27)/ES(250) (m ² /g)
850 °C	6.77 ±0.004
900 °C	5.76 ±0.002
1000 °C	4.50 ±0.013
1100 °C	2.64 ±0.006
1200 °C	0.98 ±0.009

Because of the close relationship between the surface area and the particle size, the particle size increased with a reduction of the surface area as the temperature went up, which had been discussed by German and Munir with neck-growth model [164]. Table 4.4 collects the BET specific surface areas for 10T(27)/ES(250) heated from 850 °C to 1200 °C for 2 h. The surface areas for 10T(27)/ES(250) were several times larger than that for ES(250) heated at 850 °C and 900 °C. Surface area dropped with higher annealing temperature and the value of 10T(27)/ES(250) at 1200 °C for 2 h was close to the quantity of ES(250) at 900 °C for 1 h. This surface area change coincided to the SEM morphologies in Figure 4.24 and provided more proof for the hindrance effect of CaTiO₃ on the sintering process and CaO crystal growth. Even though it is necessary to obtain CaTiO₃ with a complete reaction between CaO and TiO₂ for a more stable two-phase system, unfortunately this causes rapid loss of surface areas, which could directly influence the CO₂ chemisorption property. Thus, with the data support of the weight loss, XRD, morphology and surface area, 850 °C and 2 h were decided as the standard temperature and holding time for the further preparation of samples and investigation.

4.2.2.2 TiO₂ Particle size effect

Two types TiO₂ with particle sizes with 27 nm (T27) and 44 μm (T44) have been introduced into the powder system for further investigation. Figure 4.26 presents the

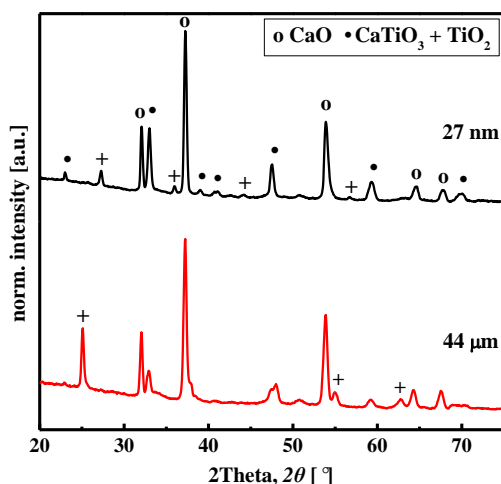


Figure 4.26 The X-ray diffraction patterns of 10T/ES(250) without and with different TiO₂ sizes heated at 850 °C for 2 hours.

XRD patterns for 10T/ES(250) with T(27) and T(44) at 850 °C for 2 hour. By comparing the two patterns in Figure 4.26, pretty high T(44) remained non-reacting and low amount of CaTiO₃ formed. Because of the large particle size, only the surface of the T(44) participated in the chemical reaction between T(44) and ES(250). The average tunnel-shape gap size on ES(250) was 0.98 μm, which was too narrow for a T(44) particle to pass through and react with the wall of the rod. As a result, it reduced the reaction efficiency of T(44) and CaO to form CaTiO₃. In nature, rutile, metastable anatase and brookite are the well-known phases of TiO₂. All of these three phases can be synthesized, moreover metastable anatase and brookite can transform into rutile under certain circumstances such as heating at high temperature [165, 166]. Because of the phases of original 27 nm (mainly rutile) and 44 μm (mainly anatase, stable below 900 °C) TiO₂ powders were different. Therefore, the phases of residual TiO₂ in 10T/ES(250) mixtures did not present with the same crystal structures.

Since the TiO₂ and CaTiO₃ coexisted in the T(27)/ES(250) system. Before performing analysis and comparison of CO₂ adsorption/desorption, it was necessary to test the chemical stabilities of TiO₂ and CaTiO₃ during carbonation/decarbonation cycles. Before running the carbonation/decarbonation cycles, CaTiO₃ and TiO₂ were heated at 850 °C for 2 h under N₂ atmosphere. This step would ensure that all the tests ran under the same conditions. The results shown in Figure 4.27 demonstrates that CaTiO₃ and TiO₂ had no chemical reactions with CO₂. The CO₂ capacities for CaTiO₃ and TiO₂ were almost at zero level with a small fluctuation, which could be neglected in comparison to the CO₂ adsorption capacity on ES(250) during the whole 10

carbonation/decarbonation cycles. This meant that CaTiO_3 and TiO_2 were the stable and inert components in the system.

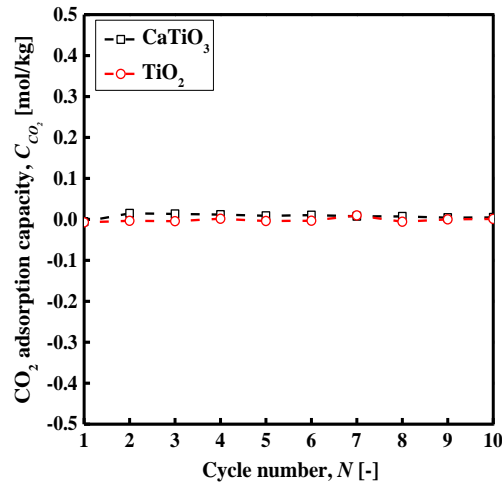


Figure 4.27 The stabilities of CaTiO_3 and TiO_2 during carbonation (700 °C, 100 % CO_2)/decarbonation (850 °C, 100 % He) procedures.

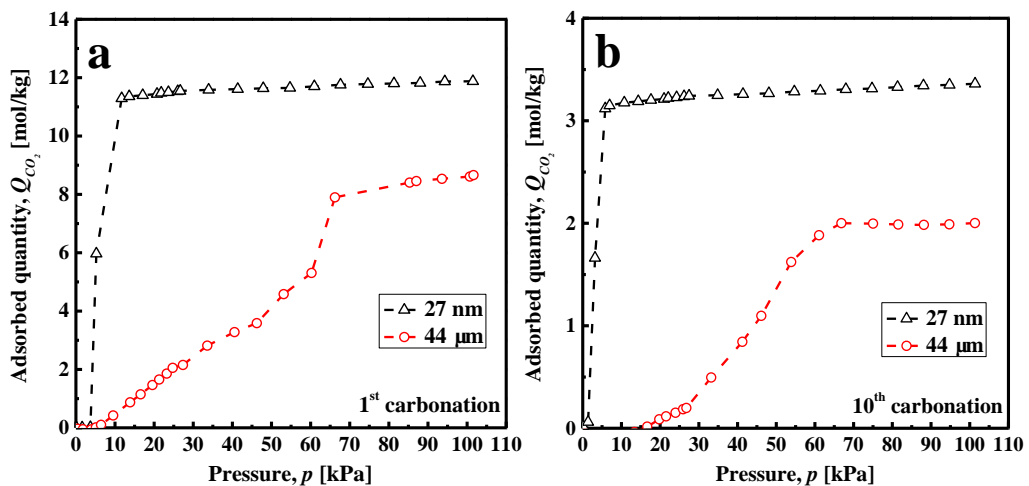


Figure 4.28 The 1st and 10th carbonation (700 °C, 100 % CO_2) isotherms of 10T/ES(250) powders with different TiO_2 sizes heated at 850 °C for 2 hours.

The investigation is focused on recycling and modifying eggshell to receive suitable and stable product as CO_2 sorbent. Hence, the behaviors of sorbents under CO_2 carbonation/decarbonation cycles are the most important aspect. The 1st and the 10th carbonation curves of CO_2 adsorption quantity versus pressure were presented in Figure 4.28. During the 1st carbonation (Figure 4.28a), the final CO_2 capacity of 10T(44)/ES(250) was about 8.7 mol/kg less than that 11.7 mol/kg of 10T(27)/ES(250). In contrast to the rapid CO_2 capacity of 10T(27)/ES(250) below 10 kPa, the CO_2 adsorbed quantity of 10T(44)/ES(250) developed very slowly and the plateau showed up above 65 kPa. The carbonation isotherm with a flatter plateau of 10T(27)/ES(250)

was analogous to the isotherm of ES(250) (Figure 4.16a). In the 10th carbonation (Figure 4.28b), the starting point of CO₂ adsorbing process for 10T(44)/ES(250) shifted from 5 kPa to 16 kPa and the turning point was located near 65 kPa with plateau more parallel to the pressure axis than the isotherm in Figure 4.28a. The maximum CO₂ adsorbed quantities for 10T/ES(250) dropped down less than 4 mol/kg, which were lower than the value (above 5 mol/kg) for ES(250).

The reaction rates of the 1st and the 10th carbonations with adsorbed quantity versus time (min) were demonstrated in Figure 4.29 to investigate more details of the chemisorption behaviors. In the 1st carbonation (Figure 4.29a), 10T(27)/ES(250) represented surface controlled and diffusion controlled chemical reaction rates. However, there was no obvious two chemical reaction rates for 10T(44)/ES(250). The chemical reaction rate was almost constant and slower than the Step I reaction rate but closer to the Step II reaction rate of 10T(27)/ES(250). It implied that the diffusion dominated the whole chemisorption in the 10T(44)/ES(250) and the reaction rate was even slower than that of the ES(250) (Figure 4.16b). In the 10th carbonation (Figure 4.29b), the activities of both 10T/ES(250) samples were enhanced and the durations were also much shorter. The 10T(27)/ES(250) was still more active than the

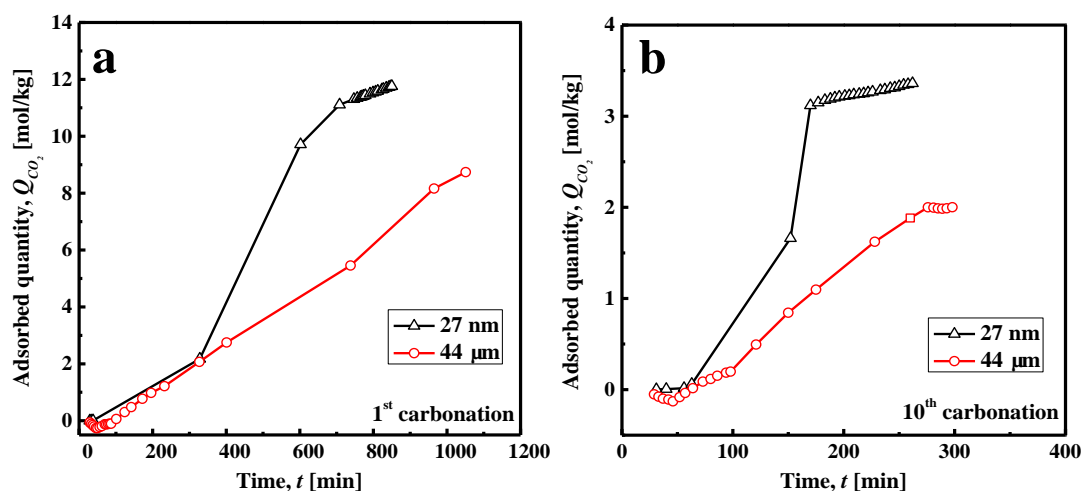


Figure 4.29 The 1st and 10th carbonation (700 °C, 100 % CO₂) reaction rate isotherms of 10T/ES(250) powders with different TiO₂ sizes heated at 850 °C for 2 hours.

10T(44)/ES(250). One difference for sample with T(44) after the 1st and the 10th carbonation was that a distinctive plateau appeared in Figure 4.29b. A fast uptake is one of the criteria on choosing CO₂ sorbents. T(44) doesn't bring positive effectiveness on this point to shorten the kinetic reaction time.

Such consequence could be linked to the TiO₂ particle size and the thickness of the inert

layer. Large particle hinders the solid state reaction speed and degree of completion like the XRD results in Figure 4.26. According to the experimental concept, the obtained powders have shell ($\text{CaTiO}_3/\text{TiO}_2$) and core (CaO) structures. An illustration of the particle after CO_2 adsorption is demonstrated in Figure 4.30.

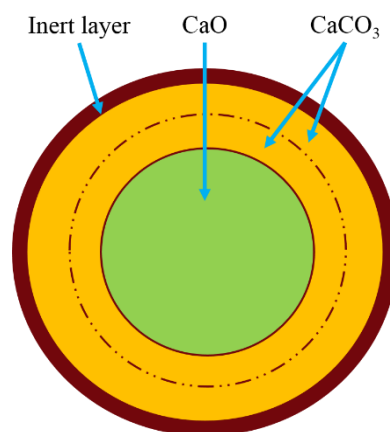


Figure 4.30 Scheme of the layers after carbonation.

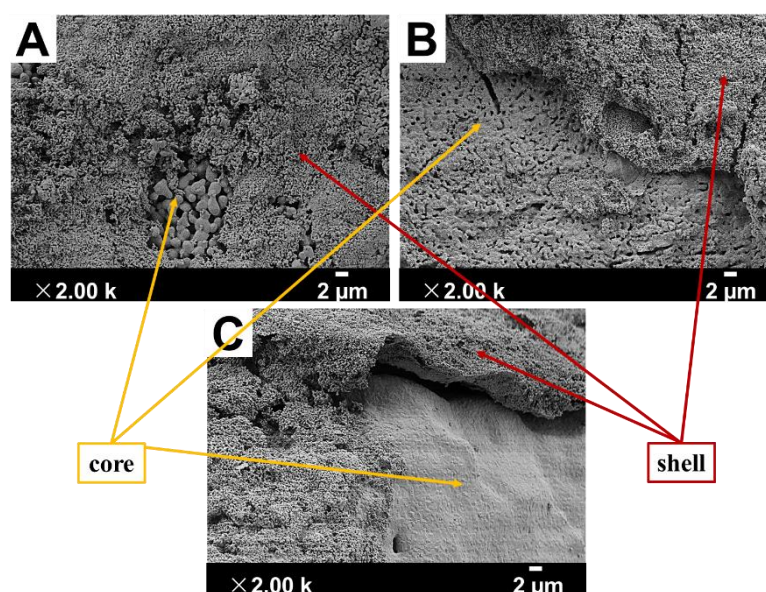


Figure 4.31 SEM morphologies of shell/core structures for 10T(27)/ES(250).

Before CO_2 chemisorption, there was one inert layer ($\text{CaTiO}_3/\text{TiO}_2$) between CO_2 and CaO . Only when CO_2 molecules moved through this inert layer, a sufficient CO_2 capture process could take place and formed a second layer (CaCO_3) between the CaO (core) and the inert layer. In this stage, all of the accessible external and internal surfaces (pores) participated in the chemical reaction (surface controlling). When this phase finished, the CO_2 gas had to penetrate through the two out layers ($\text{CaTiO}_3/\text{TiO}_2$ and CaCO_3 layers) for further carbonation, which mainly relied on the diffusion

(diffusion controlling). The formed $\text{CaTiO}_3/\text{TiO}_2$ layer was thicker with T(44) as chemical source, which resulted in a longer CO_2 penetrating distance from surface to inner core and generated more resistance for a molecule passing through. Since the particle size of T(44) was larger than the tunnel-shape gaps, the prevention of sintering effect by the T(44) as source may not be as effective as T(27). Because of these reasons, the performances of 10T(27)/ES(250) in Figure 4.28 and Figure 4.29 were better than 10T(44)/ES(250). The shell/core structure was also observed in various samples through SEM pictures Figure 4.31. Figure 4.31A was the structure of 10T(27)/ES(250) annealed at 1200 °C for 2 h. The core structure was similar to the pristine ES(250) structure (Figure 4.10B) and on the top was the shell or inert layer. Part of the shell was peeled off the core during the carbonation/decarbonation cycles and the morphologies were presented in Figure 4.31B and Figure 4.31C for 10T(27)/ES(250) after the 1st and the 10th CO_2 adsorption/desorption cycles. Because of the structure changes in the core, the interlayer between the shell and the core became much brittle and led to the exfoliation of the inert layer.

4.2.2.3 TiO_2 weight ratio effect

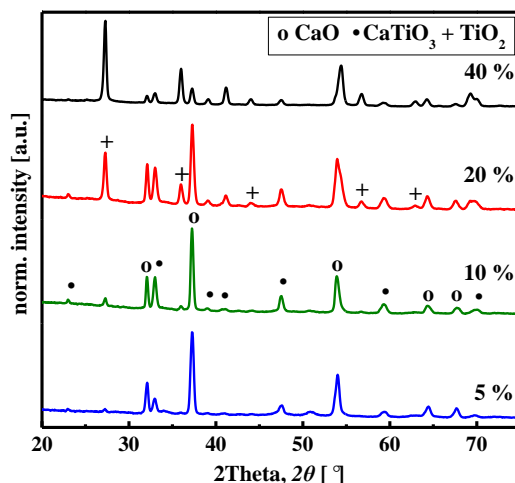


Figure 4.32 The X-ray diffraction patterns of T(27)/ES(250) with different T(27) concentrations heated at 850 °C for 2 hours.

Figure 4.32 presents the XRD patterns for T(27)/ES(250) with different T(27) concentrations at 850 °C for 2 hour. Figure 4.32 indicated that the residual T(27) was in all samples and with higher T(27) concentration (5 % to 40 %) more T(27) remained. Because the concentrations of ES(250) in samples were opposite to the concentrations of T(27), the CaO peak intensities weakened with more T(27) powders. The XRD

patterns of T(27)/ES(250) with 5 %, 10 % and 20 % T(27) indicated that optimal concentration was 5 % and 10 %, because the most of the T(27) had reacted with ES(250) in contrast to the T(27) residue in 20T(27)/ES(250). Therefore, a sequence of samples with T(27) concentrations from 5 % to 20 % were tested for further investigations.

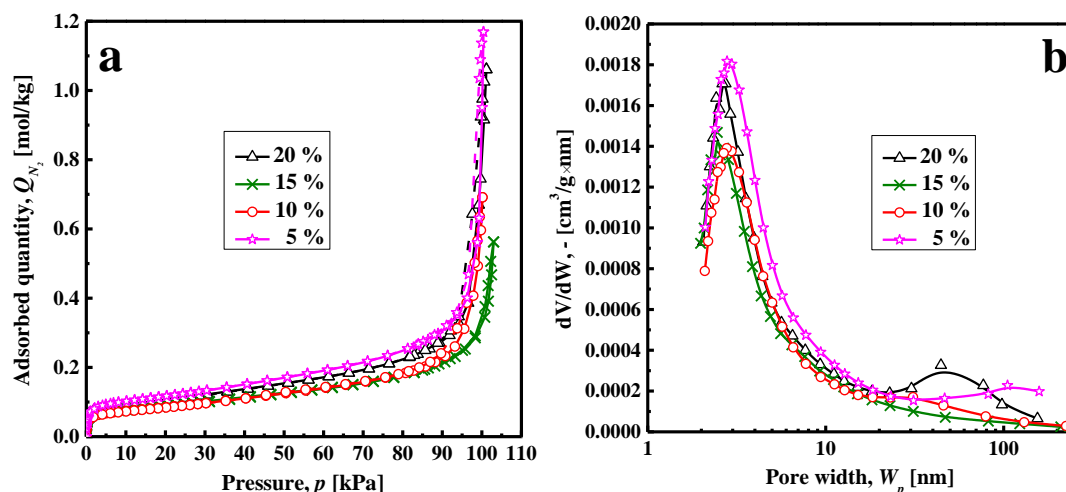


Figure 4.33 Adsorption (solid line) and desorption (dash line) isotherms and pore size distributions with N_2 at -196 °C of T(27)/ES(250) with different T(27) concentrations heated at 850 °C for 2 hours.

As mentioned above, the interstices formed by $CaTiO_3(TiO_2)$ and the space in CaO body generated during decarbonation contribute to the formation of the pores and surface area in T(27)/ES(250) system. The concentration of T(27) not only had influence on the final compositions of the powders but also affected the physic- and chemisorption properties. Figure 4.33 depicts the isotherms and the pore size distributions for T(27)/ES(250) with 5 % to 20 % T(27) being handled at 850 °C for 2 h. According to the IUPAC classification [131], the isotherms (Figure 4.33a) fitted to type IV, with a certain starting N_2 value under 1 kPa and an existing inversion point accompanied by H1 (5 % to 20 %) hysteresis loops. In the H1 hysteresis loop, the adsorption and desorption branches were more likely parallel to each other and nearly vertical in a narrow pressure range. The N_2 adsorbed quantities of samples with T(27) concentrations from 5 % to 20 % decreased from 1.17 mol/kg to 0.56 mol/kg (5 % to 15 %) and then increased again to 1.06 mol/kg (20 %). The N_2 adsorbed quantity of ES(250) was very low around 0.16 mol/kg, which stated clearly that $CaTiO_3$ and T(27) contributed a lot to the total surface area. The pore size distributions of T(27)/ES(250) (Figure 4.33b) described in depth about the influence of $CaTiO_3/TiO_2$. There were

narrow (1.7 nm to 18 nm) and broad (18 nm to 230 nm) pore size distributions. At the narrow pore size distribution area, the peaks of T(27)/ES(250) (5 % to 20 %) centered around 2.7 nm and the pore volumes were first decreasing then increasing. The formed CaTiO_3 played as an inert layer to retard the sintering effect and preserved the pores during synthesis. However, on the one hand, some of the pores in CaO body could be sealed by TiO_2 particles along with higher TiO_2 concentration, and the 10T(27)/ES(250) displayed a lower pore volume than the surface area for 5T(27)/ES(250). On the other hand, the contribution of the residual TiO_2 to the surface area and the pore volume became bigger after the concentration of TiO_2 reached a value. An increased pore volume was exhibited in T(27)/ES(250) with 15 % and 20 % T(27). More details of the changes in specific surface area will be discussed later. At broad pore size distribution area, 20 %, 10 % and 5 % T(27)/ES(250) had a tiny peak with center around 44 nm, 31 nm and 105 nm, respectively.

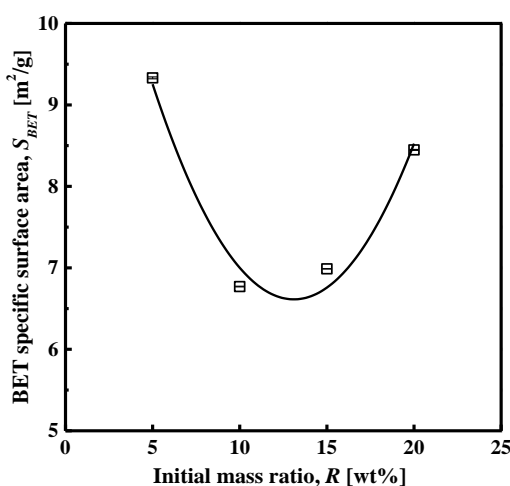


Figure 4.34 BET specific surface area changes of T(27)/ES(250) with different initial T(27) concentrations heated at 850 °C for 2 hours.

Figure 4.34 indicates the BET specific surface areas for T(27)/ES(250) with T(27) content from 5 % to 20 % at 850 °C for 2 h. From 5 % to 20 %, the specific surface areas first dropped down then climbed up in a parabolic shape. The specific surface area of ES(250) was only $1.97 \pm 0.008 \text{ m}^2/\text{g}$, which was much smaller than that of the powders containing T(27). All of the physisorption properties are related to the accessible surface. T(27) had small particle size and high surface area ($41.27 \pm 0.54 \text{ m}^2/\text{g}$), which was far larger than that of ES(250). The CaTiO_3 particle size was around 30 nm to 60 nm (Figure 4.24A, B), which was slightly bigger than T(27). The total surface area (S_t) constituted the surface areas of ES(250) or CaO

(S_{CaO}), $CaTiO_3$ (S_{CaTiO_3}) and TiO_2 with little residue (S_{TiO_2}) in T(27)/ES(250):

$$S_t = S_{CaTiO_3} + S_{CaO} + S_{TiO_2} \quad (4.8)$$

With low percentage of T(27), formed $CaTiO_3$ dispersed homogenously on the surface of ES(250) in the T(27)/ES(250) and attributed a lot to the formation of the surface area as well as preserving and forming the pores. The rod size of ES(250) in T(27)/ES(250) was around 100 nm to 200 nm, which was only $\frac{1}{5} \sim \frac{1}{4}$ of the micro rod size in the ES(250) (1.62 μm in Figure 4.11b) due to the resistance of sintering effect by $CaTiO_3$. In T(27)/ES(250), ES(250) preserved high surface area and pores. Thus, 5T(27)/ES(250) showed the highest N_2 quantity, pore volume and specific surface area. With increasing weight percentage of T(27), partial $CaTiO_3(TiO_2)$ powders played the same role as before and the contribution from S_{CaTiO_3} was enhanced, part of them blocked the existing pores, which reduced the surface area (S_{CaO} : \downarrow). The unreacted T(27) portion raised very little according to the indication of XRD result (Figure 4.32). The ratio of S_{TiO_2} was not high enough to control the total surface area. As a consequence, the shrinking amount of S_{CaO} was compensated with the increment of S_{CaTiO_3} and S_{TiO_2} . The surface area was lowered due to the nonequal quantities of reduction and augment surface area in 10T(27)/ES(250). As the amount of T(27) arrived at 15 %, more T(27) was surplus in the system, which dedicated more to the formation of the surface area as well. The slightly large surface area of 15T(27)/ES(250) just proved this situation with a small increment of the surface area. XRD pattern of 20T(27)/ES(250) (Figure 4.32) indicated that there was a lot of T(27) left in the powders. The residual T(27) in the 20T(27)/ES(250) was very high and S_{TiO_2} started to play a decisive role on surface area.

The 1st and 10th carbonation curves of CO_2 adsorption quantity versus pressure were presented in Figure 4.35. During the 1st carbonation (Figure 4.35a), the CO_2 adsorbed quantities of 5 %, 10 % and 20T(27)/ES(250) lessened by degrees. The uptakes of 5 % to 20 % T(27)/ES(250) augmented rapidly at low pressure range before reaching the plateau. In the 10th carbonation (Figure 4.35b), the behaviors of T(27)/ES(250) samples were quite alike, that turning points showed up around 10 kPa and the slope was very steep. All showed similar plateaus with different CO_2 adsorbed amounts and the curves for 10 % and 20 % T(27)/ES(250) overlapped.

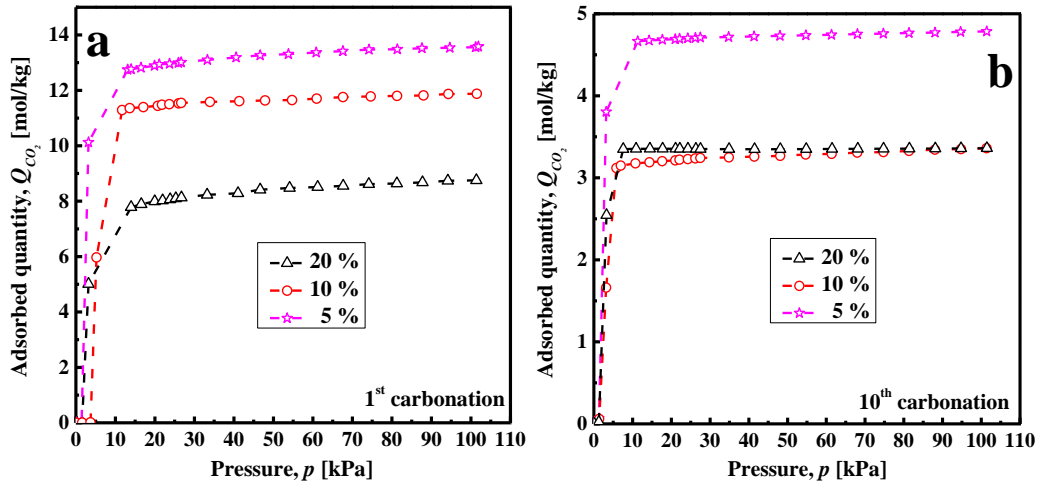


Figure 4.35 The 1st and 10th carbonation (700 °C, 100 % CO₂) isotherms of T(27)/ES(250) with different T(27) concentrations heated at 850 °C for 2 hours.

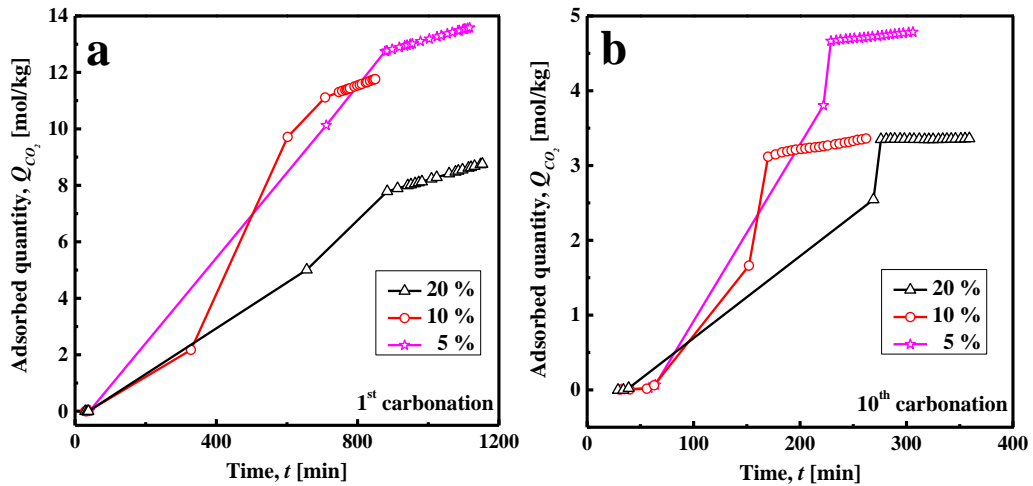


Figure 4.36 The 1st and 10th carbonation (700 °C, 100 % CO₂) reaction rate isotherms of T(27)/ES(250) with different T(27) concentrations heated at 850 °C for 2 hours.

In corresponds to Figure 4.35, reaction rates of T(27)/ES(250) were investigated. The chemical reaction rates of the 1st and the 10th carbonations with adsorbed quantity versus time (min) are demonstrated in Figure 4.36. In the 1st carbonation (Figure 4.36a), they resembled the carbonation isotherms in Figure 4.35a with two developing steps. The chemical activities of 5 % to 20 % T(27)/ES(250) were a little more prominent than the activity of ES(250) with CO₂ molecule as well as shorter carbonation periods. For T(27)/ES(250), intrinsic surface reaction (Step I) controlled the CO₂ chemisorption, while the diffusion reaction (Step II) dominated the CO₂ adsorption for ES(250). The reaction rate of Step I for 5 % and 10 % T(27)/ES(250) were quicker than the reaction rate of the 20T(27)/ES(250), which were slower than the first reaction rate of ES(250). This could be caused by the inert layer on the surface CaO yielding to slower mobility

of CO₂ from outside onto the CaO surface. In the 10th carbonation (Figure 4.36b), 5 % to 20 % T(27)/ES(250) behaved quite similar to Figure 4.36a but with faster kinetic reaction on the surface. The activities of T(27)/ES(250) improved during the carbonation/decarbonation cycles. In comparison of the second plateaus (Step II) in Figure 4.36a, the increment of the 2nd plateau in Figure 4.36b was relatively insignificant.

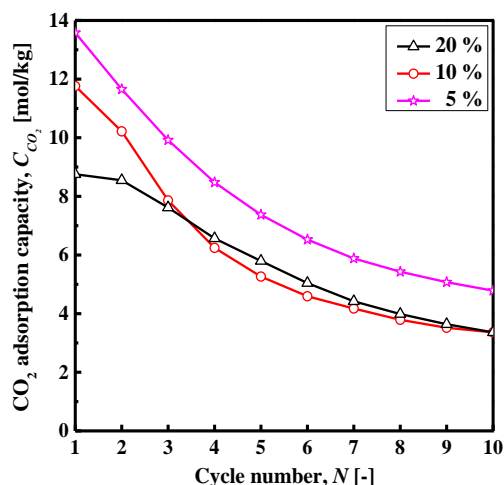


Figure 4.37 The maximum CO₂ uptakes during carbonation (700 °C, 100 % CO₂)/decarbonation (850 °C, 100 % He) cycles of T(27)/ES(250) powders with different T(27) concentrations and heated at 850 °C for 2 hours.

Based on the Equation 4.4, the tendencies of CO₂ capacity for the powders during carbonation/decarbonation cycles were presented in Figure 4.37. One common trend for the samples under all these different annealing conditions was that the CO₂ capacity gradually diminished after each carbonation/decarbonation cycle and after the 10th carbonation the capacities of all samples were less than half of the initial CO₂ uptakes. The CO₂ cycle curves of T(27)/ES(250) were more or less parallel to each other except for the curve of 20T(27)/ES(250). The first two cycles, CO₂ capacities of 20T(27)/ES(250) were below the CO₂ adsorbed amounts of the 10T(27)/ES(250), and from the 3rd to the 10th cycle the two curves tended to overlap. Figure 4.37 indicated that too high concentration of TiO₂ did not contribute much to the CO₂ capacity or the stability.

The amount of TiO₂ governed the thickness of the layer on the eggshell powders which also had influence on the CO₂ capacity and reaction rate of the sample. As the results in Figure 4.35 and Figure 4.36, there were always two different reaction rates during the carbonation process due to the gas-solid chemical reaction kinetics which were

surface controlled reaction and diffusion controlled reaction. By adding more T(27), on the one hand the effective component (CaO) ratio decreased which resulted in a lower CO₂ capacity. On the other hand, the layer on ES(250) particle in T(27)/ES(250) became thicker and introduced more resistance for CO₂ permeation from outside into the inner ES(250) particle. These could be the reasons for the diminishing maximum CO₂ uptakes of samples 5 % to 20 % T(27)/ES(250). However, CaTiO₃/TiO₂ layer could partially prevent the grain growth during carbonation/decarbonation and stabilize the chemisorption property which could be observed in the results of 20T(27)/ES(250).

4.2.2.4 N₂ physisorption properties

In order to understand the CO₂ chemisorption on T(27)/ES(250) and the influence of CaTiO₃ and TiO₂ on the properties of T(27)/ES(250) better, a N₂ physisorption analysis on 10T(27)/ES(250) after 1, 2, 5 and 10 CO₂ adsorption/desorption cycles was operated and the results are shown in Figure 4.38. The N₂ isotherms of 10T(27)/ES(250) (Figure 4.38a) was similar to the isotherms for ES(250) with decreasing N₂ quantities and maximum adsorption values. They belonged to type IV isotherm and H1 hysteresis

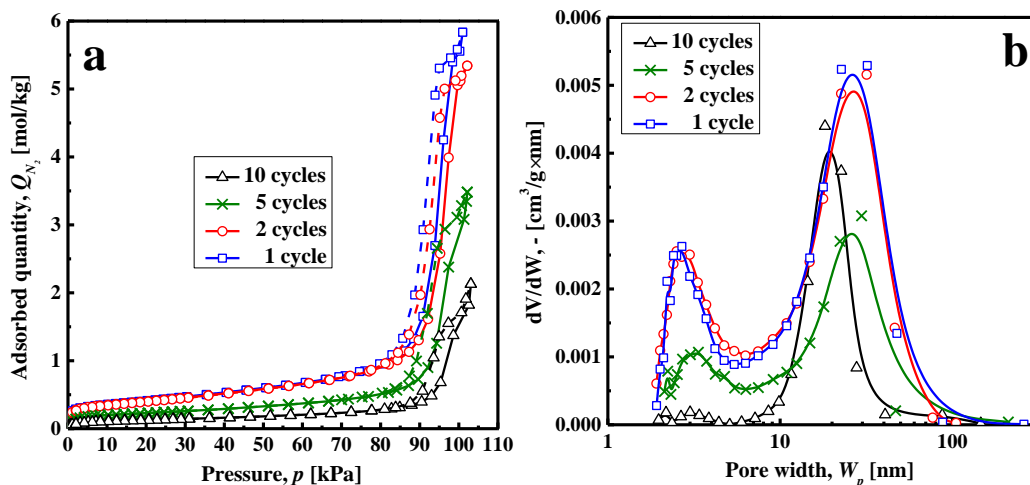


Figure 4.38 Adsorption (solid line) and desorption (dash line) isotherms and pore size distributions with N₂ at -196 °C of 10T(27)/ES(250) after 1, 2, 5, 10 carbonation/decarbonation cycles.

loop associated with porous materials. But the decreasing trends of 10T(27)/ES(250) were slower than these of ES(250) and the hysteresis loops of 10T(27)/ES(250) after 5 and 10 cycles were larger than the loops of ES(250) (Figure 4.13a). This implied that 10T(27)/ES(250) still maintained a certain amount of pores after 10 cycles of CO₂ adsorption and desorption. This could be demonstrated with the pore size distributions in

Figure 4.38b. The samples exhibited bimodal pore size distributions (two peaks) with a fair number of small pores ranging from 1.7 nm to 10 nm. The pore size distributions after the 1st and the 2nd cycles kept relatively similar positions and intensities. The peak intensities after 5 and 10 cycles diminished which indicated the disappearance of pores. The peak centers moved slightly towards higher pore width range after the 5th cycle, and the peak intensity of the small pores (1.7 nm to 10 nm) dramatically decreased. On the contrary to the pore size distribution after the 5th cycle, the peak intensity of the large pores (> 10 nm) after the 10th cycle increased with lowering of the peak center (Figure 4.38b). This pore size distributions of 10T(27)/ES(250) were different from the ES(250), where the peak intensities gradually weakened after various carbonation/decarbonation cycles with the peak centers of both small and large pore ranges slightly shifting to lower diameter (Figure 4.13b). This pore size distribution results proved the important role of CaTiO₃ inert layer on maintaining the quantity of pores.

4.2.2.5 Macro-structure

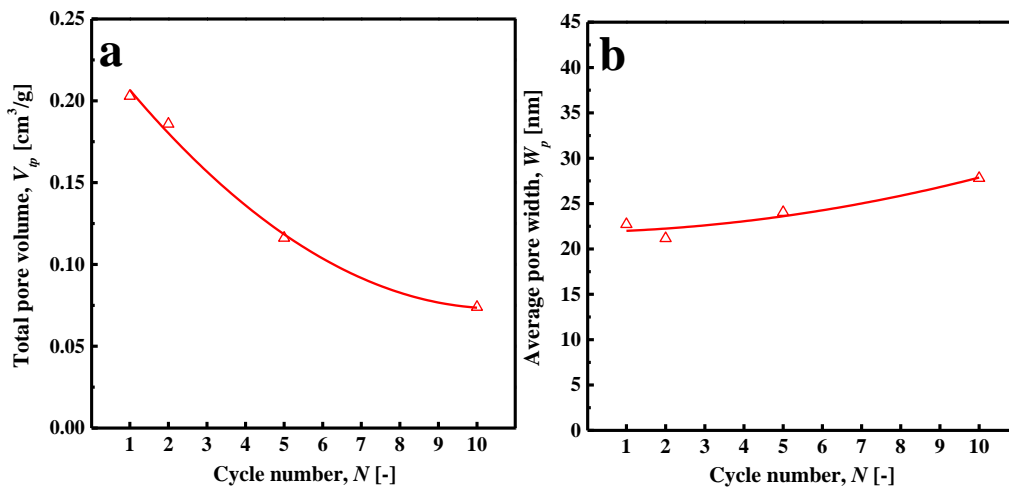


Figure 4.39 Pore volumes and average pore widths of 10T(27)/ES(250) after 1, 2, 5, 10 carbonation/decarbonation cycles.

The decaying phenomenon of N₂ isotherms and pore size distributions after various CO₂ ad- and desorption cycles on 10T(27)/ES(250) can be more easily observed and understood through the changes of the total pore volume values and the average pore diameters after CO₂ chemisorption in Figure 4.39. The pore volume of 10T(27)/ES(250) before CO₂ adsorption was 0.024 cm³/g, which was 4 times higher than the pore volume for ES(250) and the average pore diameter was around 15 nm. After the first CO₂

adsorption/desorption, the total pore volume increased to 0.2 cm³/g (close to the value for ES(250), Figure 4.14a), while in the following 2, 5 and 10 cycles, the pore volumes descended and the pore volume after the 10th cycle went down to 0.07 cm³/g. The pore volume quantity of 10T(27)/ES(250) was almost overlapping with the amount of ES(250) (Figure 4.14a), which suggested that a similar structure changes on ES(250) also happened in the core of 10T(27)/ES(250). The average pore widths after carbonation/decarbonation were widened (between 20 nm and 30 nm) compared to 15 nm of the adsorbent before CO₂ adsorption procedure. The pores of 10T(27)/ES(250) tended to grow bigger with more cycles in a rather mild way in contrast to the pore diameter development for ES(250) in Figure 4.14b. This ascribed to dope the TiO₂ and form CaTiO₃ which could be demonstrated by the change of morphologies.

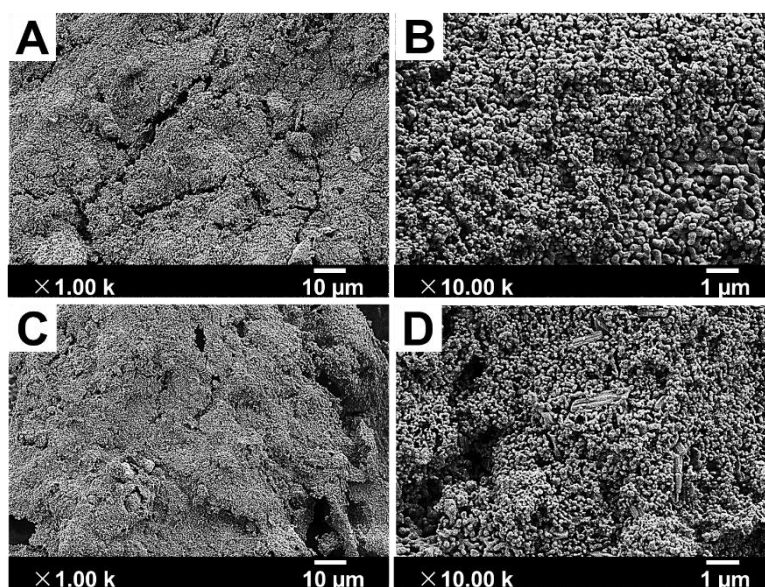


Figure 4.40 SEM morphologies of 10T(27)/ES(250) after: (A, B) 1 and (C, D) 10 carbonation/decarbonation cycles.

The particle sizes of the CaTiO₃/TiO₂ layer in 10T(27)/ES(250) had no apparent variation after 1 and 10 calcination/carbonation cycles (Figure 4.40), which proved the thermal stability of CaTiO₃/TiO₂ under this carbonation/decarbonation conditions. The inert layer displayed to be fluffier and partially deciduous after the 10th CO₂ chemisorption.

The ES(250) under the layer exhibited porous structures with macro-pores (> 50 nm, here 100 nm - 600 nm) and meso-pores (2 nm - 50 nm) spreading throughout the surface during carbonation/decarbonation (Figure 4.41A, B). Different from the

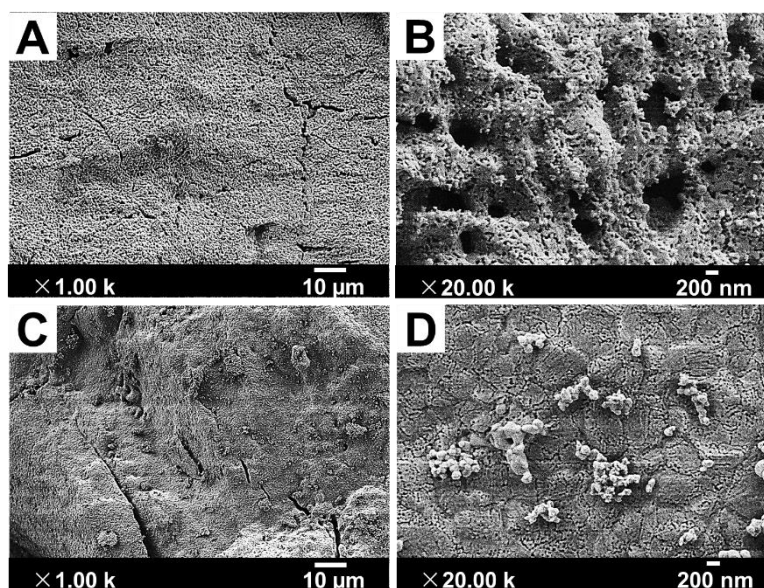


Figure 4.41 SEM morphologies of 10T(27)/ES(250) under inert layer after: (A, B) 1 and (C, D) 10 carbonation/decarbonation cycles.

morphology of ES(250) in Figure 4.15, the porosity of CaO-rich component under the $\text{CaTiO}_3/\text{TiO}_2$ layer decayed slower and there were macro-pores instead of tunnel-shape gaps as well as with a huge amount of meso-pores after the 1st cycle (Figure 4.41A, B) because of the retard influence on sintering effect from the $\text{CaTiO}_3/\text{TiO}_2$ layer. After the 10th cycle, the majority of visible macro-pores (100 nm - 600 nm) disappeared and the surface of 10T(27)/ES(250) under $\text{CaTiO}_3/\text{TiO}_2$ layer was more densified with homogeneous meso-pores (Figure 4.41C, D) which was in accordance with the pore size distribution result of one sharp peak centered around 18 nm (Figure 4.38b).

4.2.2.6 Chemical reaction rate

The physisorption properties and morphologies of 10T(27)/ES(250) were mostly similar to the physisorption performance of ES(250). However, there was a small difference with pore extinguishing rate (slower in 10T(27)/ES(250)), which led to the various behaviors of CO_2 chemisorption. The 1st, 2nd, 5th and 10th carbonation isotherms of CO_2 adsorption quantity versus pressure are presented in Figure 4.42a for 10T(27)/ES(250) as well as the chemical reaction rate curves (Figure 4.42b). Part of the carbonation development of 10T(27)/ES(250) had already been discussed earlier in Section 4.2.2.2 and Section 4.2.2.3. The 2nd and the 5th carbonation isotherms of 10T(27)/ES(250) were similar to the 10th isotherm except that the turning point of the

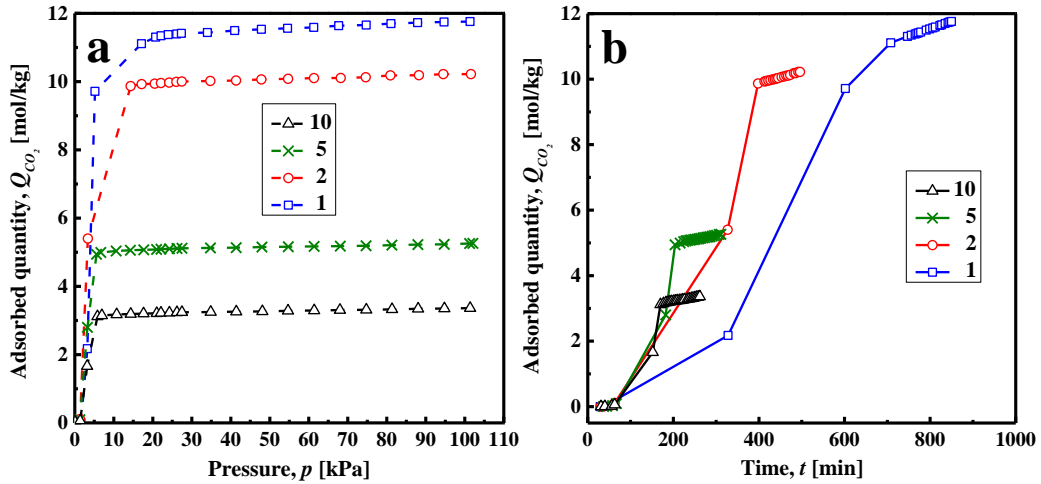


Figure 4.42 The 1st, 2nd, 5th and 10th carbonation (700 °C, 100 % CO₂) and chemical reaction rate isotherms of 10T(27)/ES(250).

2nd isotherm was located at a relatively high pressure area and the plateau of the 5th isotherm showed up at a lower pressure point (Figure 4.42a). Comparing with the carbonation isotherms of the ES(250) (Figure 4.16a), the turning points on the curves of 10T(27)/ES(250) emerged earlier below 12 kPa, and the plateaus of the 5th and the 10th carbonations shifted to even lower pressure area (< 6 kPa). The CO₂ adsorption happening at low pressure is a good property for application, while no CO₂ filtering and compressing were required before the gas was injected into the solid adsorbent. The CO₂ capacity loss from the 5th to the 10th isotherm for 10T(27)/ES(250) was 36 % which was slightly lower than 38 % of ES(250). Fast and slow chemical reaction rates occurred in chemical reaction isotherms (Figure 4.42b). The instinct surface reaction dominated the carbonation through the complete 10 CO₂ adsorption/desorption cycles and the diffusion controlled reaction stage did not contribute much to chemisorption. Differing from the diffusion controlled reaction isotherm of ES(250) at the 1st cycle, surface reaction of 10T(27)/ES(250) lasted for a long period of time and the reaction rate appeared to be slightly slower than the Step I rate in the subsequent cycles. Figure 4.24B pointed out that the rod size of CaO in 10T(27)/ES(250) was smaller than the rod thickness of ES(250), which as a result generated a higher accessible and active surface area for CO₂ adsorption. Therefore, the dominating role of 10T(27)/ES(250) at the first carbonation transformed from diffusion to surface controlling. The reaction rates of the 2nd and the 5th carbonations for 10T(27)/ES(250) partly overlapped at Step I with the 10th carbonation curve and were slower than the kinetic reaction rates for the 2nd to the 10th carbonation in ES(250). This may be caused by the resistance from the

inert layer.

Table 4.5 BET specific surface areas of 10T(27)/ES(250) after 0, 1, 2, 5, 10 carbonation/decarbonation cycles.

Cycles	10T(27)/ES(250) (m ² /g)
0	6.77 ± 0.004
1	32.85 ± 0.01
2	32.16 ± 0.01
5	18.53 ± 0.10
10	10.44 ± 0.06

The surface area of 10T(27)/ES(250) is a summation of CaO, TiO₂ and CaTiO₃ surface areas. In accordance with the morphology results before and after CO₂ adsorption processes, the change for CaTiO₃/TiO₂ was not significant (Figure 4.40) and the structure of CaO on the other hand changed distinctly (Figure 4.41). Hence, the total BET surface area can in some degree depicted the surface area change of CaO in T(27)/ES(250) system. Table 4.5 sums the BET specific surface areas for 10T(27)/ES(250) before and after 1, 2, 5 and 10 CO₂ chemisorption/regeneration processes. The BET surface area before carbonation was 6.77 m²/g higher than the surface area for the ES(250), which resulted in the kinetic rate change in Figure 4.42b. After the 1st CO₂ ad-/desorption, the specific surface area of 10T(27)/ES(250) was 32.85 m²/g larger than that of ES(250), which corresponded to the diversities of morphologies in Figure 4.15(C, D) and Figure 4.41(A, B). However, the surface areas were reduced along with more cycles and the surface area was cut down to 10.44 m²/g after the 10th carbonation/decarbonation, which was only slightly higher than 8.05 m²/g of ES(250). Due to the close relationship between the surface area and the CO₂ adsorption capacity as well as the stability, it is necessary to have a further study about the variation of adsorbed CO₂ quantities and CaO conversions during the CO₂ capture/regeneration cycles.

4.2.2.7 CO₂ adsorption stability

A trace of TiO₂ was detected by the XRD pattern of 10T(27)/ES(250) (Figure 4.22c), and the residual amount of TiO₂ could not be accurately calculated. Due to the very close peak positions of TiO₂ and CaTiO₃, the accuracy of simulating the XRD patterns of this system is not very high. However, in the calculation of a CaO carbonation

conversion, the percentage of CaO in the system is necessary. Therefore, an assumption has been made here by applying Equation 4.5. The theoretical calculation value Y of CaO is 71.8 %. If a residue amount of TiO_2 is assumed to be 50 %, then the Y value of CaO is 77.6 %. And the difference of CaO carbonation conversion between the results calculated from 71.8 % and 77.6 % are 1 % to 5 %. In reality, the TiO_2 residual quantity was far lower than 50 %, because only a tiny trace of TiO_2 was shown on XRD. Thus, 71.8 % was adopted for the CaO carbonation conversion calculation, which was approximately the real CaO percentage in 10T(27)/ES(250).

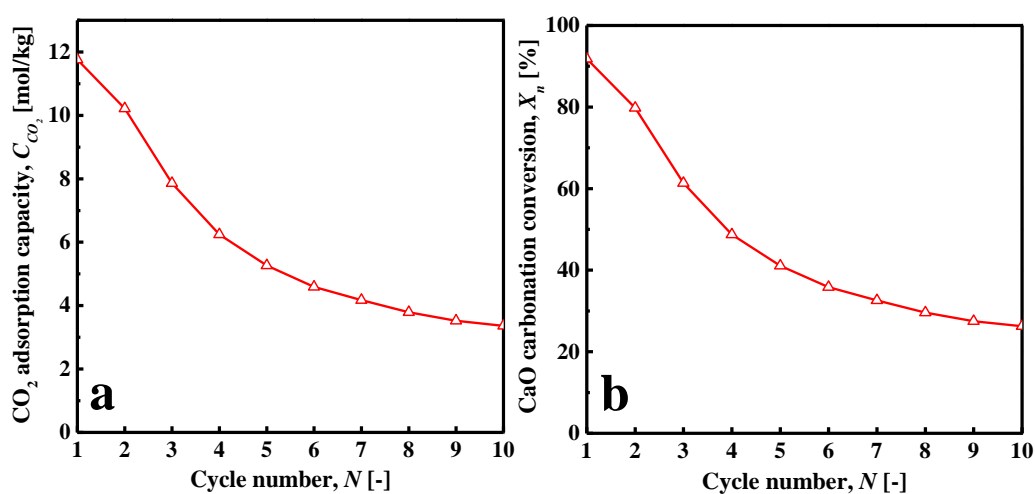


Figure 4.43 The CO_2 adsorption capacities and CaO carbonation conversions during carbonation (700 °C, 100 % CO_2)/decarbonation (850 °C, 100 % He) cycles of 10T(27)/ES(250) powders heated at 850 °C for 2 hours.

The CO_2 adsorbed quantity gradually decayed after each adsorption/desorption cycle and after the 10th carbonation the capacity of 10T(27)/ES(250) was only 3.36 mol/kg (Figure 4.43a). This could be due to the sintering with the loss of the new born pores after the 1st carbonation/decarbonation cycle. The efficiency of reacted CaO was quite high at the beginning with around 92 % (Figure 4.43b), which was higher than the conversion for ES(250). However, the CaO carbonation conversion slipped down to 80 % and 61 % after the 2nd and the 3rd cycle. On the one hand, it implied that 10T(27)/ES(250) had higher CaO conversion at the first several cycles and the doping of TiO_2 contributed to such improvements. On the other hand, the severer decrease of CaO carbonation conversion in 10T(27)/ES(250) meant that the positive effect of TiO_2 doping was not enough to stop the extinguishing of pores, which was also proved by the morphology in Figure 4.41D. A possible reason could be the large particle size of eggshell powders. Although some of the T(27) could access into the tunnel-shape gaps

and react with CaO rods to prevent the contact among these CaO rods, the rods were not completely isolated from each other by CaTiO₃ inside the eggshell powder. Therefore, deep inside of the rods may still be connected to each other and Ca²⁺ ions could possibly flow from one CaO rod to another. In another aspect, the crystal volume of CaCO₃ is almost 3 times of the crystal volume for CaO. When carbonation started, the reacted CaO would also grow into a larger size containing CaCO₃ and this size expansion could lead to the contact among CaO rods without CaTiO₃ layer. As a consequence, such unification created a chance for sintering.

4.3 Calcined eggshell as Ca source with CaTiO₃ dopant

4.3.1 Experimental Methods

A calcined eggshell consists of two parts: tunnel-shape gaps and micro rods (CaO-rich). Due to such structures, the mechanical strength of calcined eggshell is weak and brittle. Single rod can be produced by manual grounding with little effort. Two TiO₂ powders (particle size: 27 nm and 44 μm) were selected for the doping and synthesis of CaTiO₃. The ratios of TiO₂ powders in the TiO₂ and calcined eggshell system (T/ES(calcined)) were 5 % and 10 %, respectively. In order to compare T/ES(calcined) system with T/ES(250) system, the weight percentage of TiO₂ was calculated in following equation

$$TiO_2 \text{ wt } \% = \frac{m_{TiO_2}}{m_{TiO_2} + m_{CaCO_3}} \times 100 \% \quad (4.9)$$

m_{TiO_2} and m_{CaCO_3} are the masses for TiO₂ and CaCO₃ (or dried ES), respectively. Ca source, named as ES(calcined), was eggshell with a size range of 125 μm-250 μm decomposed at 850 °C for 2 h. In the case of the application of ES(calcined) powders, the necessary mass of ES(calcined) was calculated by Equation 4.1. For example, in a sample 10T/ES(250) with a composition of 0.3 g TiO₂ and 2.7 g dried ES, then the mass of ES(calcined) is $\frac{2.7 \times 56.077}{100.087} = 1.52$ g in 10T/ES(calcined) sample.

The approach to prepare samples for annealing was the same as the process for T/ES(250) system using dried ES as Ca-source. The original structure of ES(250) was destroyed during preparation of T/ES(calcined) powders. Calcination was conducted at 850 °C for two hours. The morphologies, N₂ physisorption, phase analysis and CO₂ chemisorption were performed with the same parameters for the other series of eggshell-based adsorbents, which have been described in Section 4.1.1. The concept was the same as the system produced in Section 4.2.1 to acquire a shell/core structure.

The shell consisting of CaTiO_3 worked as inert layer to separate CaO particles from contacting each other and restrain the sintering effect. The prepared samples were named according to Table 4.3.

4.3.2 Results and discussions

4.3.2.1 TiO_2 particle size effect

A phase composition analysis by XRD is shown in Figure 4.44 for 10T/ES(calcined) powders with 27 nm and 44 μm TiO_2 as sources under the heating condition of 850 $^\circ\text{C}$ for 2 h. Two-phase powders (CaO and CaTiO_3) were obtained by both samples. The basic structure of ES(250) as raw material was destroyed during preparation which yielded very small particle sizes and enhancing the reaction between TiO_2 and ES(calcined).

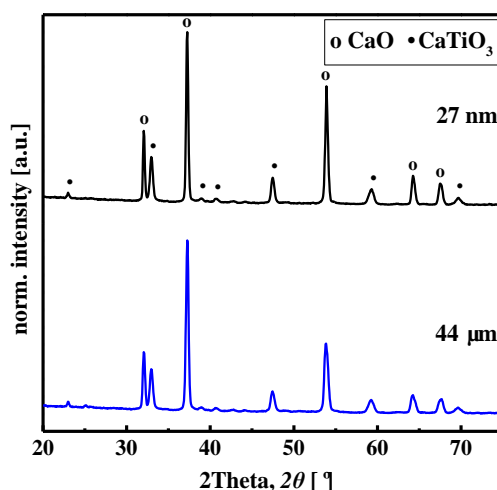


Figure 4.44 The X-ray diffraction patterns of 10T/ES(calcined) powders with different TiO_2 sizes heated at 850 $^\circ\text{C}$ for 2 hours.

The final powders consisted only CaO and CaTiO_3 with either T(27) or T(44) as chemical reagent. The influence of TiO_2 particle size on the CO_2 chemisorption during carbonation/decarbonation was interesting. The 1st and 10th carbonation curves of CO_2 adsorption quantity versus pressure are presented in Figure 4.45. During the 1st carbonation (Figure 4.45a), the developments of CO_2 capacity for T/ES(calcined) were different to the CO_2 uptakes for T/ES(250) which always showed a rapid increase at low pressure range (0 - 20 kPa) (Figure 4.35). 10T(27)/ES(calcined) showed a quick and small CO_2 uptake at pressures below 6 kPa, while CO_2 uptake by 10T(44)/ES(calcined) was insignificant at pressures below 5 kPa. The carbonation

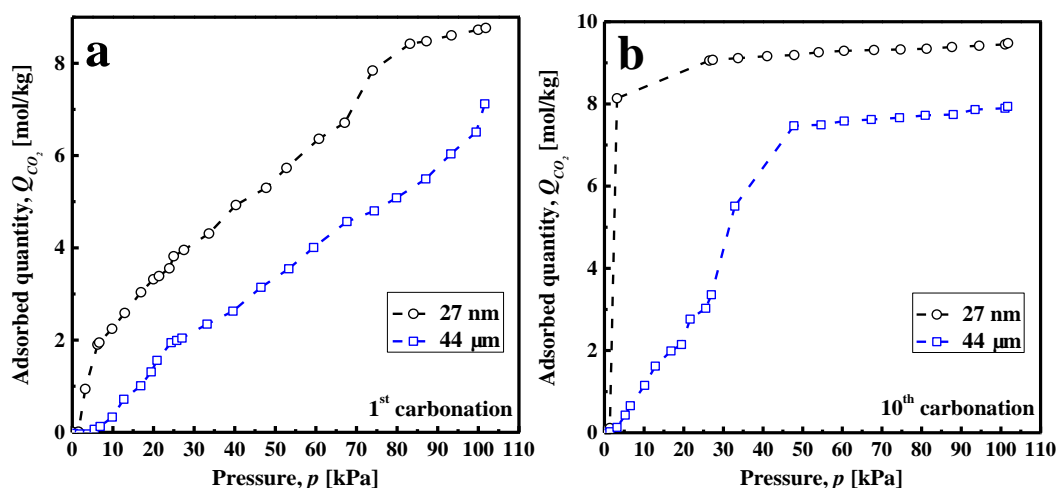


Figure 4.45 The 1st and 10th carbonation (700 °C, 100 % CO₂) isotherms of 10T/ES(calcined) powders with different TiO₂ sizes heated at 850 °C for 2 hours.

isotherms of 10T(27)/ES(calcined) and 10T(44)/ES(calcined) were similar and no plateau like the carbonation isotherms for ES(250) and T(27)/ES(250) (Figure 4.16a and Figure 4.35a) was observed. On the contrary to the first carbonation, there were obvious turning points and plateaus for 10T/ES(calcined) in the 10th carbonation (Figure 4.45b). In the 10th carbonation, the turning points of 10T(27)/ES(calcined) and 10T(44)/ES(calcined) occurred at 3 kPa and 48 kPa, respectively. That meant the activation of the 10T/ES(calcined) was enhanced. The adsorbed CO₂ quantities by T/ES(calcined) were almost constant at high pressures until the end of the carbonation process. The carbonation isotherm in the 10th cycle for 10T(27)/ES(calcined) was similar to the isotherm of 10T(27)/ES(250) but with a steeper curve at the low pressure area (Figure 4.28). The isotherm of 10T(44)/ES(calcined) was similar to the first isotherm curve of 10T(44)/ES(250) (Figure 4.28a). This observation is probably due to the core/shell structure (Figure 4.30) for both T/ES(calcined) and T/ES(250). The thickness of the inert layers for both 10T(27)/ES(250) and 10T(27)/ES(calcined) were close, and identical for 10T(44)/ES(250) and 10T(44)/ES(calcined) samples. The maximum CO₂ uptakes for 10T/ES(calcined) remained on the same levels for the 1st and 10th carbonation cycles. The observation that 10T(27)/ES(calcined) captures CO₂ at very low pressure (below 3 kPa) was an important step in the optimization progress. The reaction rates of the 1st and 10th carbonations with adsorbed quantity versus time (min) are demonstrated in Figure 4.46. In the 1st carbonation (Figure 4.46a), the chemical activities of T/ES(calcined) were close to each other. Instead of surface controlled reaction regime, diffusion controlled regime of CO₂ capture dominated the

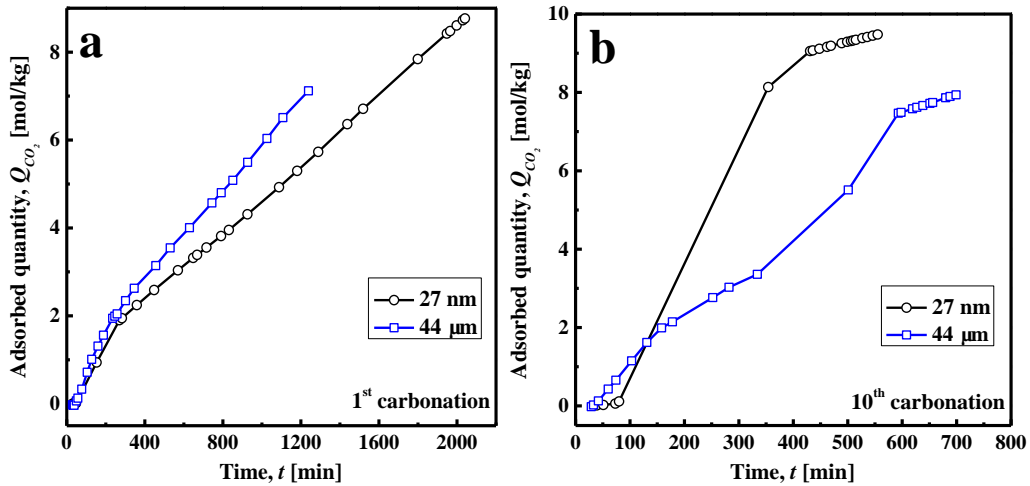


Figure 4.46 The 1st and 10th carbonation (700 °C, 100 % CO₂) reaction rate isotherms of 10T/ES(calcined) powders with different TiO₂ sizes heated at 850 °C for 2 hours.

whole carbonation rhythm, which followed the behavior of ES(250) in the first carbonation (Figure 4.16b). The cause for such performance could be the low porosity and surface area of the core inside the sample. Thus, the outside CaO from the core quickly reacted with CO₂ and the surface was completely covered by CaCO₃. Only diffusion allowed a further reaction of CO₂ and the CaO from the inner core. The diffusion reaction rate for 10T(44)/ES(calcined) was slightly higher than the rate of 10T(27)/ES(calcined). For CO₂ molecule, there were two pathways for the diffusions: diffusion on the solid surface (CaCO₃ layer and CaTiO₃ layer) and diffusion in meso and macropores [27]. The diameter of interstices formed by the agglomeration of large size particles is bigger than small size particles. The diffusional resistance through larger interstices is lower than through small ones. Therefore, CO₂ diffused through the interstice pores in 10T(44)/ES(calcined) faster than in 10T(27)/ES(calcined), which caused a slightly higher diffusion reaction rate in the 1st carbonation cycle. In the 10th carbonation (Figure 4.46b), the Step I (surface reaction) of chemisorption played the main role and the durations of this carbonation process with T/ES(calcined) were much shorter than before. The reaction rate of 10T(27)/ES(calcined) had been improved by a factor of three, while the chemical reaction rate of 10T(44)/ES(calcined) only enhanced by a factor of 1.5.

Figure 4.46 shows that each T/ES(calcined) had the same CO₂ capacities to adsorb CO₂ during the 1st and 10th carbonations. For this reason, detailed investigation on CO₂ adsorption during carbonation/decarbonation cycles were conducted (Figure 4.47 and Figure 4.48). According to the Equations 4.1, 4.6 and 4.7, the percentages of CaO and

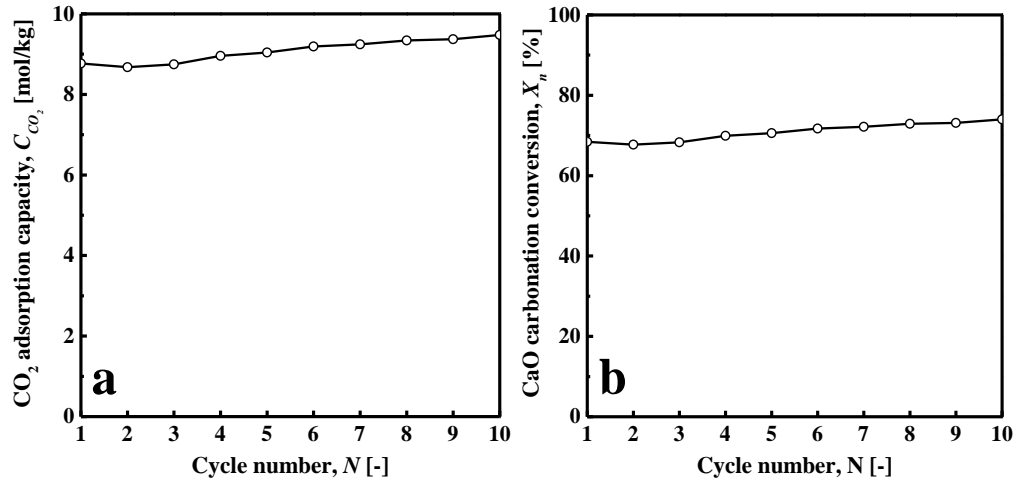


Figure 4.47 The CO₂ adsorption capacities and CaO carbonation conversions during carbonation (700 °C, 100 % CO₂)/decarbonation (850 °C, 100 % He) cycles of 10T(27)/ES(calcined) heated at 850 °C for 2 hours.

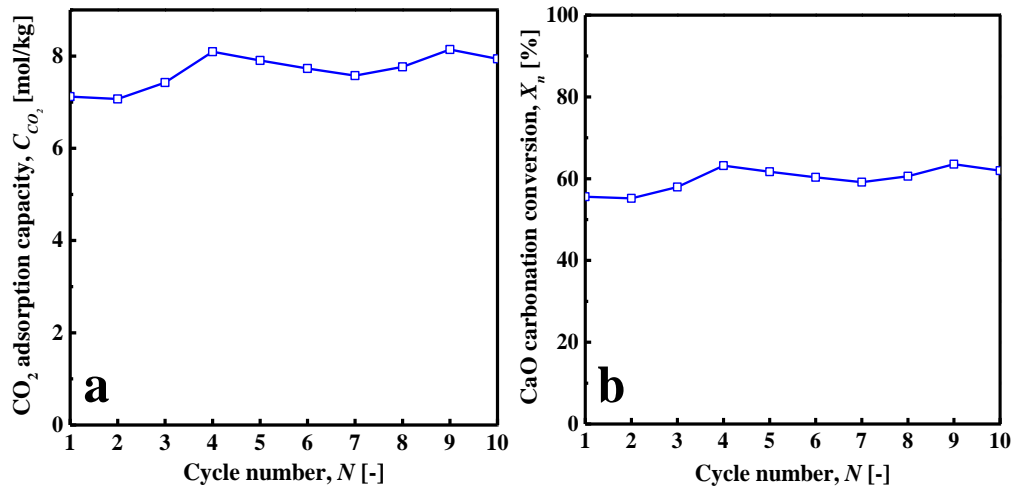


Figure 4.48 The CO₂ adsorption capacities and CaO carbonation conversions during carbonation (700 °C, 100 % CO₂)/decarbonation (850 °C, 100 % He) cycles of 10T(44)/ES(calcined) heated at 850 °C for 2 hours.

CaTiO₃ in sample 10T/ES(calcined) were 71.1 % and 28.9 %, respectively. These values were applied for the calculation of CaO carbonation conversion in Equation 4.5. The CO₂ capture properties of T/ES(calcined) were generally very stable except that small fluctuations were observed in sample 10T(44)/ES(calcined). 10T(27)/ES(calcined) had a higher CO₂ storage capacity, in average 9.08 mol/kg, compared to 10T(44)/ES(calcined) with an average value of 7.68 mol/kg. Theoretically, 1 kg CaO can adsorb 17.8 mol CO₂. Therefore, the conversion rates of CaO were incomplete. The average CaO conversion rates of 10T(27)/ES(calcined) and 10T(44)/ES(calcined) were 71 % and 60 %, respectively. It is very obvious that the stability of sorption capacity and CaO conversion of 10T(27)/ES(calcined) were

superior compared to 10T(44)/ES(calcined). Although the constituent ratios of 10T(27)/ES(calcined) and 10T(44)/ES(calcined) were identical, there was 1.4 mol/kg CO₂ capacity difference between them and the CaO conversion of 10T(27)/ES(calcined) was 11 % higher than 10T(44)/ES(calcined) due to smaller TiO₂ particle size of 10T(27)/ES(calcined). The maximum and minimum CaO conversions of ES(250) were 77 % (1st carbonation) and 31 % (10th carbonation), respectively. The average CO₂ adsorption capacity was 9 mol/kg for 10-times carbonations which was equal to the value of 10T(27)/ES(calcined). Therefore, T/ES(calcined) samples with ES(calcined) as raw material are much promising for the application because of the durability and high capacity in the capture of CO₂. It surpasses the CO₂ capture properties of CaO-based sorbents published in literatures [114, 167-169]. For instance, S.F. Wu et al [114] investigated the CaO/CaTiO₃ system using commercial nano CaCO₃ and tetrabutyl titanate (Ti(OC₄H₉)₄) as precursors. The maximum CO₂ uptake of CaO/CaTiO₃ (weight ratio 1:9 for TiO₂ and CaCO₃) was 5.3 mol/kg and, therefore lower than the CO₂ capacities of T/ES(calcined).

4.3.2.2 N₂ physisorption properties

During carbonation/decarbonation, sintering occurs and leads to the growth of crystals, closure of the pores and consequently to a reduction in an effective surface area discussed in Section 4.1 and Section 4.2. The decaying or unstable CO₂ adsorption capacities and CaO conversions of ES(250) and T/ES(250) was caused by the shrinkage of effective surface area, pores and particle sizes. The modification of T/ES(calcined) adsorbents on the other hand showed some improved CO₂ adsorption stability as well as in the CaO carbonation conversion. In order to understand the factors for such improvement, this section mainly focusses on the structures under various conditions. For a better understanding and comparison with the other CaO-based adsorbents discussed earlier, 10T(27)/ES(calcined) was selected for further discussion.

Figure 4.49 describes the N₂ isotherms and pore size distributions at -195 °C of 10T(27)/ES(calcined) after 1, 2, 5, 10 CO₂ adsorption and desorption cycles. In contrast to the deteriorating N₂ isotherms and shrinking hysteresis loops of ES(250) and 10T(27)/ES(250) after CO₂ chemisorptions (Figure 4.13a and Figure 4.38a), the isotherms of 10T(27)/ES(calcined) (Figure 4.49a) were similar with initial uptakes, maximum N₂ adsorbed quantities, isotherm and hysteresis loop types. According to the

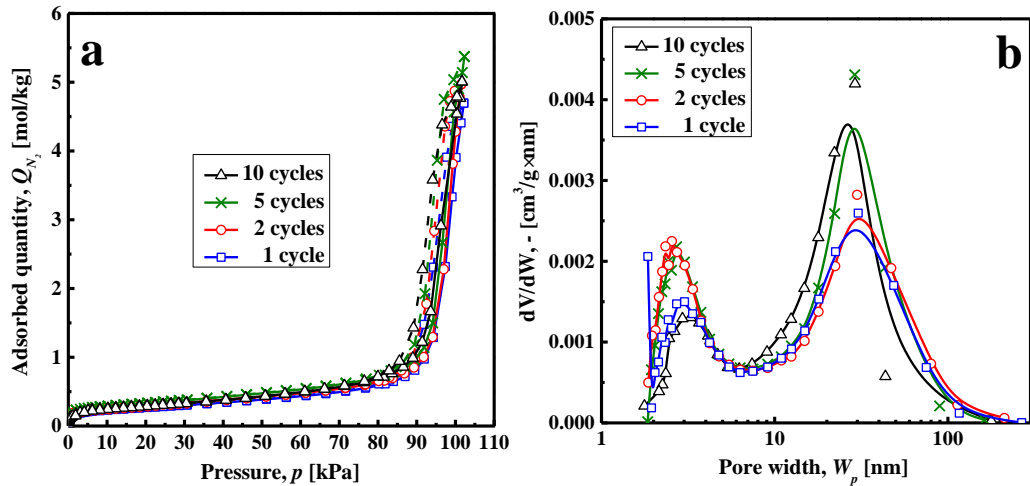


Figure 4.49 Adsorption (solid line) and desorption (dash line) isotherms and pore size distributions with N_2 at $-196^\circ C$ of 10T(27)/ES(calcined) after 1, 2, 5, 10 carbonation/decarbonation cycles.

IUPAC classification [131], the isotherms belonged to type IV having a certain starting N_2 value under 1 kPa and existing inversion point accompanied by hysteresis loop type H1 for porous materials. In the H1 hysteresis loop, the adsorption and desorption branches converge to parallels and are nearly vertical in a narrow pressure range. All of the pore size distributions exhibited two peaks in a bimodal distribution with a fair number of small pores ranging from 1.7 nm to 10 nm and minority large pores ranging from 10 nm to 100 nm. The peak centered at 10 nm to 100 nm shifted to lower pore diameters and the peak intensities enhanced (Figure 4.49b). It differed from the peak intensities of ES(250) and 10T(27)/ES(250) (Figure 4.13b and Figure 4.38b). The peaks for small pores (ranging from 1.7 nm to 10 nm) first moved to slightly small sizes and then became large in 10T(27)/ES(calcined) during the cycles. In this range, the peak intensities showed the same phenomenon. The pore size distributions of the 1st and 2nd carbonation cycles almost overlapped and similarity in the 5th and 10th carbonation cycles, which indicated the dynamically stable pore structures. There was single pore size around 1.9 nm with high pore volume for the pore size distribution of 10T(27)/ES(calcined) after the 1st CO_2 chemisorption, which didn't exist in the pore size distributions after 2nd to 10th CO_2 adsorption. The disappearance of the micropores could be due to the tendency to reach more homogenous pore sizes through recrystallization and reorganization of CaO during CO_2 capture cycles which will be discussed in Section 4.3.2.3 on macro-structure. The sintering effect also contributes to the disappearance of the micropores.

4.3.2.3 Macro-structure

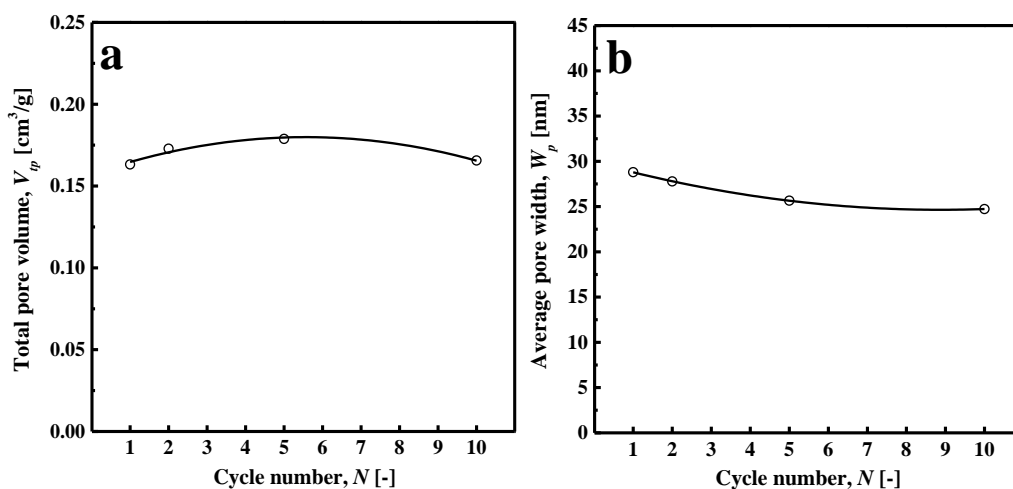


Figure 4.50 Pore volumes and average pore widths of 10T(27)/ES(calcined) after 1, 2, 5, 10 carbonation/decarbonation cycles.

The total pore volumes and average pore diameters of 10T(27)/ES(calcined) reflects more details on the pore structures after 1, 2, 5 and 10 CO_2 adsorption and adsorbent regeneration cycles (Figure 4.50). The pore volume of 10T(27)/ES(calcined) before CO_2 adsorption was $0.019 \text{ cm}^3/\text{g}$, which was a slightly lower than the pore volume for 10T(27)/ES(250) but three times higher than the pore volume $0.006 \text{ cm}^3/\text{g}$ of ES(250). The average pore diameter was around 19 nm. After the first CO_2 adsorption/desorption, the total pore volume increased to $0.16 \text{ cm}^3/\text{g}$, while in the following 2, 5 and 10 cycles, the pore volumes changed in the range of $0.16 \text{ cm}^3/\text{g}$ to $0.18 \text{ cm}^3/\text{g}$ with a mild fluctuation. In general, the pore volumes remained at a constant level, whereas the pore volumes of ES(250) and 10T(27)/ES(250) decreased with the numbers of cycles (Figure 4.14a and Figure 4.39a). The average pore widths after adsorption/desorption were increased (between 24 nm and 29 nm) compared to 15 nm before CO_2 carbonation. The pore widths of 10T(27)/ES(calcined) tended to decrease slightly with more cycles and it was opposite to the pore diameter developing for either ES(250) (Figure 4.14b) or 10T(27)/ES(250) (Figure 4.39b). Such kind of pore rearrangement in 10T(27)/ES(calcined) (Figure 4.50) was induced by the re-growth and reunion of crystals to obtain more homogenous structures and reduce surface energy, which was also reported in the literature [170]. The SEM photos of ES(250) (Figure 4.15) and 10T(27)/ES(250) (Figure 4.41) illustrate this phenomenon. A scheme of the pore development is shown in Figure 4.54.

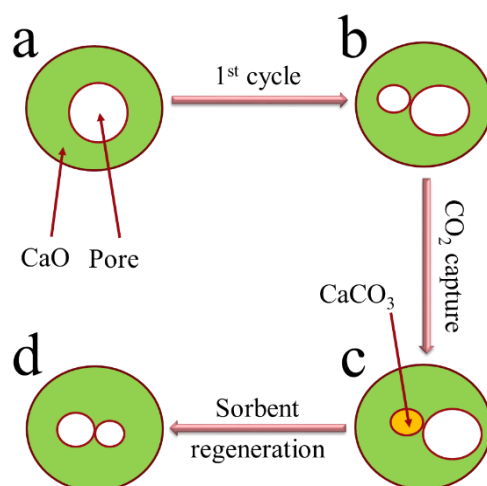


Figure 4.51 Scheme of pore rearranging during carbonation/decarbonation cycles: a) pristine sample, b) after the 1st carbonation, left pore (small) and right pore (large), c) after carbonation, left pore filled, d) after decarbonation, left pore expanded and right pore shrank [171].

In the pore size distribution demonstrated in Figure 4.12b, only one peak turned up in pristine ES(250) powders, which corresponds to the scheme of Figure 4.51a. After the 1st cycle of carbonation/decarbonation, bimodal pore size distributions (two peaks) were observed in all sample systems. In this process, the surface of CaO reacts with CO₂ and small pores are filled by CaCO₃ through carbonation. In the calcination stage, a sintering process is involved and guides ions to fill the pores, vacancies or inter-granular space. It causes a transfer of ions from small to large pore due to the surface energy gradient. The released CO₂ could enhance CaO sintering with the direction of gas flow. The final result is shown in Figure 4.51b [171]. After the 1st CO₂ adsorption/desorption cycle, the pores of a sample consist of two parts: left pore (small) generated by calcination and right pore (large) due to the pore growth by the flow of CO₂. P. Sun et al [171] divided the pores into small and large groups by the a pore diameter of 220 nm. Because of the limitation of the instrument used in the experiment, only pore size less than 300 nm could be detected. Thus, only few pores above 200 nm were detected in the pore size distribution. At the carbonation stage, the reaction occurred first in small pores (left) which were filled by CaCO₃, while the large pores (right) attributed only little to the carbonation as a result of low surface area (Figure 4.51c). There are two stages during carbonation, namely surface controlled reaction (fast reaction) and diffusion controlled reaction (slow reaction). When the fast reaction regime finishes and the small pores are completely filled by CaCO₃, slow reaction takes over for further carbonation and large pores act as a diffusion

transportation system. During the subsequent decarbonation, ideally left pore should be reproduced during calcination. However, sintering is always involved during calcination. The driving force of sintering is to reduce free energy by lowering surface area (forming large pores or eliminating pore amounts). Therefore, in the subsequent calcination, left pore regrew with relatively large size and right pore on the other hand shrank, as the CO_2 was liberated and transported outward (Figure 4.51d). When the right pore size is smaller than left pore size, in the next round of carbonation, right pore will be utilized first again and the reproduced left pore size will shrink further in calcination. Since the preparation of 10T(27)/ES(calcined) was based on the ES(calcined), some of the rods, and cleavages or gaps structures could still exist except for the reduced powder size, because of the manual grounding and the weak mechanism strength of ES(250). At the initial cycles of carbonation/decarbonation, these macropores and cleavages undergo the process shown in Figure 4.51 with the consequence of increased numbers of small pores, which lead to the incensements of pore volumes (Figure 4.50a).

After 2, 5 and 10 carbonation/decarbonation cycles, the pore volumes of 10T(27)/ES(250) and ES(250) decline, while the pore volumes of 10T(27)/ES(calcined) remain constant, which is also the reason for its stable durability in CO_2 capture (Figure 4.47 and Figure 4.48). To some degree, $\text{CaTiO}_3/\text{TiO}_2$ can slow down the sintering process. As a consequence, the rate of volume reduction of 10T(27)/ES(250) is slower than that of ES(250). As shown in Figure 4.18, the CaTiO_3 layer is supposed to isolate CaO particles and prevent sintering during carbonation/decarbonation cycles, which is successful with 10T(27)/ES(calcined). The pore volumes of 10T(27)/ES(calcined) almost remain nearly constant with slightly fluctuations. However, the average pore diameters appear to decline slightly during carbonation and calcination cycles (Figure 4.50) which is consistent with the pore rearrangement in Figure 4.51. On the contrary, the average pore widths of 10T(27)/ES(250) and ES(250) tend to decrease first and then increase. The particle size of ES(250) is the main factor associated to the sintering effect. When the particle sizes become small, for example several micrometers, sintering effect can be greatly inhibited by avoiding contact with the other CaO-rich particles. T/ES(calcined) sequence is the best example for this. This approach named microcapsule has been applied long time ago by Ishikawa H. et al [172] on alloy-copper hydrogen storage. Akiyama T. et al [173] produced copper-coated

microcapsule of Mg-Ni with 20 μm average diameter and showed its great properties on hydrogen storage. The size of T/ES(calcined) powder is below 20 μm because of the natural and brittle ES(250) structures.

4.3.2.4 Chemical reaction rate

CO_2 chemisorption has an intimate relationship with the structures of an adsorbent, which can be characterized by N_2 physisorption. As the aforementioned results, physisorption properties of 10T(27)/ES(calcined) were more stable than those of 10T(27)/ES(250) and ES(250) considering N_2 isotherms, pore size distributions, pore volumes and average pore sizes after different CO_2 capture cycles. The carbonation and chemical reaction rate isotherms of 10T(27)/ES(calcined) were supposed to be better than the performances of 10T(27)/ES(250) and ES(250) based on the physisorption results. Figure 4.52 shows the carbonation and chemical reaction rate isotherms after the 1st, 2nd, 5th and 10th CO_2 adsorption/desorption cycles. Part of the carbonation development of 10T(27)/ES(calcined) has been already discussed earlier (Section 4.3.2.1). The second and 5th carbonation isotherms of 10T(27)/ES(calcined)

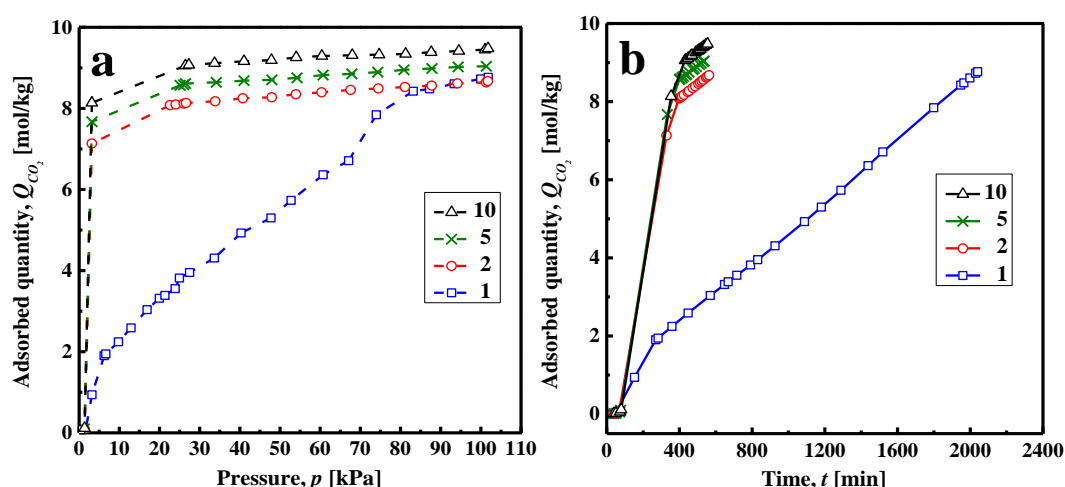


Figure 4.52 The 1st, 2nd, 5th and 10th carbonation (700 $^{\circ}\text{C}$, 100 % CO_2) and chemical reaction rate isotherms of 10T(27)/ES(calcined).

were similar to the 10th isotherm except slight difference in the CO_2 maximum adsorbed quantities. Compared with the 1st isotherm of 10T(27)ES(calcined), the turning point of the 2nd isotherm appeared at very low pressure (3 kPa) and chemisorption was mainly completed in this pressure range (Figure 4.52a). Among ES(250), 10T(27)/ES(250) and 10T(27)/ES(calcined), the reactivity of 10T(27)/ES(calcined) from the 2nd to 10th CO_2 chemisorption cycles was the highest, because the CO_2 adsorption occurred at very low

pressure and also reached the maximum CO₂ adsorption capacities at low pressures. The reaction rates of the 1st, 2nd, 5th and 10th carbonations with adsorbed quantity versus time (min) are demonstrated in Figure 4.52b. The chemical reaction rates of the 2nd and 5th carbonations for 10T(27)/ES(calcined) completely overlapped with the curve of the 10th carbonation at the Step I regime with instinct surface as dominator (Figure 4.52b). The curves at the Step II regime were parallel to each other. This means that the reaction rates of Step I and Step II are constant after the 1st carbonation cycle. Comparing the 1st chemical reaction rates of ES(250), 10T(27)/ES(250) and 10T(27)/ES(calcined), it could be found that the duration of the surface controlled kinetic reaction in 10T(27)/ES(calcined) was the shortest with the longest diffusion dominating reaction.

Table 4.6 BET specific surface areas of 10T(27)/ES(calcined) after 0, 1, 2, 5, 10 carbonation/decarbonation cycles.

Cycles	10T(27)/ES(calcined) (m ² /g)
0	4.40 ± 0.004
1	21.67 ± 0.04
2	23.66 ± 0.01
5	26.29 ± 0.02
10	23.95 ± 0.06

The causes for that could be the differences of the surface areas of the pristine adsorbents. The BET specific surface area evolution after 0, 1, 2, 5 and 10 CO₂ adsorption/regeneration cycles are listed in Table 4.6. The surface area of pristine 10T(27)/ES(calcined) was 4.40 m²/g in a medium range compared with the surface area value 1.97 m²/g of ES(250) and 6.77 m²/g for 10T(27)/ES(250). As described in Equation 4.8, the surface area of 10T(27)/ES(calcined) consists of two parts: S_{CaO} and S_{CaTiO_3} ($S_{TiO_2} = 0$ for no residual TiO₂). Since the Ca-source in 10T(27)/ES(calcined) was ES(250), S_{CaO} should be equal to the surface area of ES(250). During the synthesis of 10T(27)/ES(calcined), ES(250) underwent a twice-thermal treatment which could raise the sintering factor and the disappearance of the existed pores in ES(250). Thus, the real S_{CaO} in 10T(27)/ES(calcined) would be smaller than the primitive ES(250). With 10T(27)/ES(250) sample, the situation was different because TiO₂ or CaTiO₃ created an retardant effect on sintering and S_{CaO} would be larger than the original ES(250). Consequently, the BET specific surface area of 10T(27)/ES(calcined) was between the values for ES(250) and 10T(27)/ES(250). The accessible CaO surface area

was the lowest. Due to such variations in surface area, the first carbonation behavior of 10T(27)/ES(calcined) yielded the longest diffusion controlled reaction. After the first cycle, the surface area of 10T(27)/ES(calcined) grew to 21 m²/g and the surface areas remained constant with small fluctuations. Thanks to the large surface area, the reaction rate switched from a diffusion-controlled to a surface-controlled rate.

4.3.2.5 Further optimizing

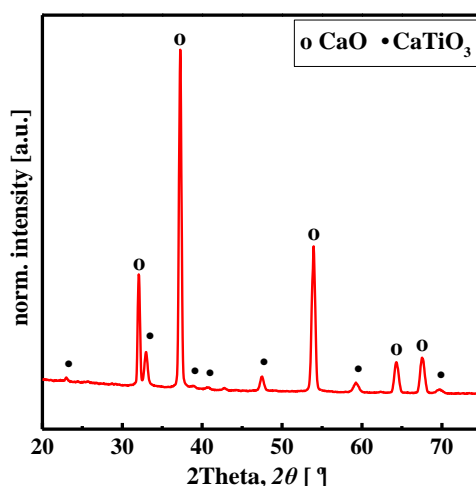


Figure 4.53 The X-ray diffraction patterns of 5T(27)/ES(calcined) powders heated at 850 °C for 2 hours.

The doped sample of T/ES(calcined) powders was proved to be an effective and stable CO₂ adsorption sorbent. For future application purpose, a further optimization process was conducted, which reduced the doping amount of T(27) (better CO₂ chemisorption performance than T(44)). Phase analysis, carbonation isotherm, chemical reaction rate as well as the CO₂ capture stability and CaO carbonation conversion are discussed here. The constituents of 5T(27)/ES(calcined) were similar to the other T/ES(calcined) samples with pure two phases except the ratio of CaO over CaTiO₃ here was greater and more CaO could participate into CO₂ capture.

Since the phase components in these three samples are all the same, the CO₂ chemisorption behaviors during carbonation/decarbonation become interesting. The 1st and 10th carbonation curves of CO₂ adsorption quantity versus pressure for 5T(27)/ES(calcined) are presented in Figure 4.54. During the 1st carbonation (Figure 4.54a), 5T(27)/ES(calcined) showed a quick CO₂ uptake at a pressure range of 0-25 kPa. The second part of the isotherm, after turning point, increased relatively mild. On the contrary to the 1st carbonation, the slope of the line for 5T(27)/ES(calcined) was

very large at low pressures with an obvious turning point in the 10th carbonation (Figure 4.54b). In the 10th carbonation, the carbonation isotherms of 5T(27)/ES(calcined) and 10T(27)/ES(calcined) were similar and the turning points of 5T(27)/ES(calcined) shifted to 3 kPa as well.

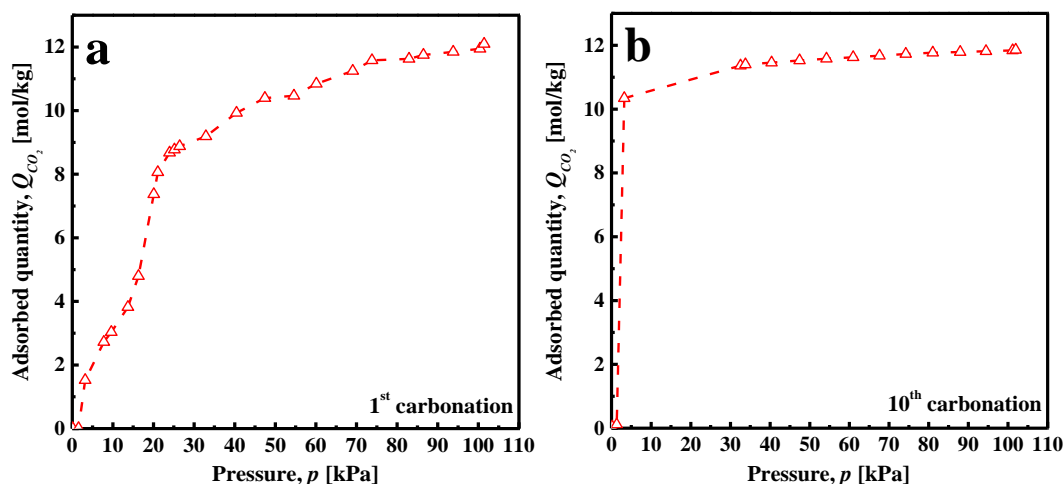


Figure 4.54 The 1st and 10th carbonation (700 °C, 100 % CO₂) isotherms of 5T(27)/ES(calcined) heated at 850 °C for 2 hours.

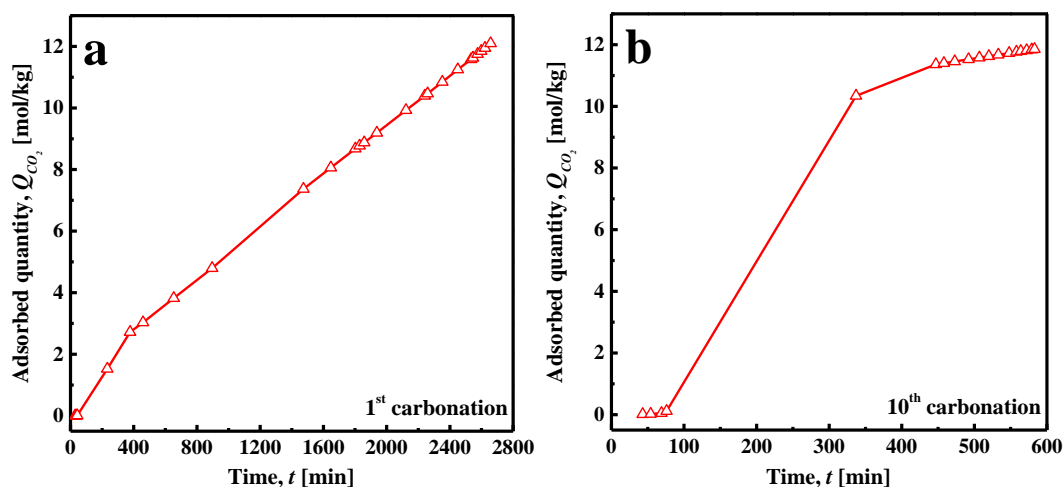


Figure 4.55 The 1st and 10th carbonation (700 °C, 100 % CO₂) reaction rate isotherms of 5T(27)/ES(calcined) heated at 850 °C for 2 hours.

The reaction rates of 1st and 10th carbonations with adsorbed quantity versus time (min) are shown in Figure 4.55. In the 1st carbonation (Figure 4.55a), the chemical activity of 5T(27)/ES(calcined) was almost equal to the activity of 10T(27)/ES(calcined), and the reaction rate of Step II was slightly higher than that of 10T(27)/ES(calcined). The diffusion time of 5T(27)/ES(calcined) lasted the longest comparing to the other two T/ES(calcined) samples (Figure 4.46a). Instead of the instinct surface controlled adsorption, diffusion dominated the whole carbonation rhythm. In the 10th carbonation

(Figure 4.55b), the Step I of chemisorption played the main role and the period of 5T(27)/ES(calcined) was much shorter than it in the 1st carbonation. The reaction rate of 5T(27)/ES(calcined) had been improved by four times, while the chemical reaction rate of 10T(27)/ES(calcined) and 10T(44)/ES(calcined) only enhanced by three and 1.5 times compared to the reaction rates in the first carbonation cycles (Figure 4.46b).

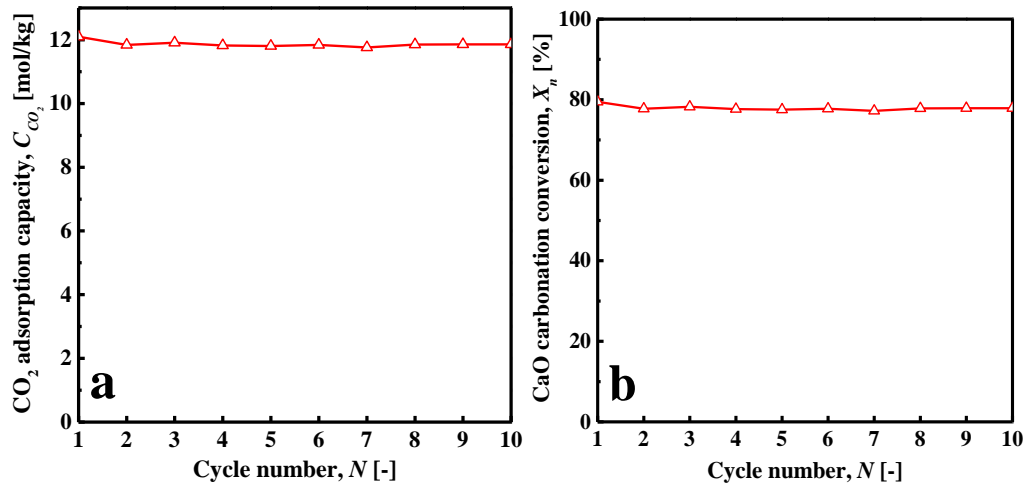


Figure 4.56 The CO₂ adsorption capacities and CaO carbonation conversions during carbonation (700 °C, 100 % CO₂)/decarbonation (850 °C, 100 % He) cycles of 5T(27)/ES(calcined) heated at 850 °C for 2 hours.

The compositions of CaO and CaTiO₃ in sample 5T(27)/ES(calcined) are 85.4 % and 14.6 %, respectively. These results were applied for the calculation of CO₂ conversion and the results are presented in Figure 4.56. A stable CO₂ adsorption capacity of 11.86 mol/kg was obtained by 5T(27)/ES(calcined) with average CaO carbonation conversion of 78 %. It is clear that the chemisorption properties of 5T(27)/ES(calcined) was enhanced. The reducing amount of TiO₂ resulted in a more effective CaO in the system, and consequently to enhance CO₂ adsorption quantities. Furthermore, the thinner layer of CaTiO₃ could reduce the resistance for CO₂ diffusion and probably large pores show up in the inner layer, which as well lowered the obstruction for the permeability of CO₂ molecule.

4.4 Conclusions

Three different CaO-based CO₂ adsorbents were produced and investigated. The CO₂ adsorption performance of ES(250) and T/ES(250) decayed during the CO₂ adsorption/desorption cycles due to the loss of surface areas and pores induced by sintering effect. The sintering effect with T/ES(250) was retarded during sample

preparation. T/ES(calcined) samples possessed stable CO₂ adsorption capacities with stable surface areas, pore volumes and pore diameters for CO₂ storage. The stability of CO₂ adsorption was the best for T/ES(calcined) with average CO₂ adsorbed quantities of 7.68 mol/kg, 9.08 mol/kg and 11.86 mol/kg for 10T(44)/ES(calcined), 10T(27)/ES(calcined) and 5T(27)/ES(calcined), respectively. The associated average CaO carbonation conversion were 60 %, 71 % and 78 %, respectively. Two chemical reaction rates exist in the system: intrinsic surface area controlled kinetic reaction rate (Step I: fast) and diffusion controlled reaction rate (Step II: slow). Generally, the 1st carbonation cycle was dominated by Step II as a result of the low porosity and surface area. After the first carbonation, the CO₂ adsorption was controlled by Step I with fast reaction rate and low CO₂ pressure activity. This was the consequence of the larger amount of pores produced by the outward CO₂ transportation during the first CO₂ adsorption/desorption cycle. The pore size was redistributed in the CO₂ carbonation/decarbonation.

In the present work, 5T(27)/ES(calcined) shows a quite good properties on either CO₂ adsorption capacity or chemisorption stability due to the isolation and support of CaTiO₃ inert layer. A core/shell structure is produced with CaTiO₃ as shell and CaO as core. Other methods may help to define this structure beside SEM, such as the energy dispersive X-ray spectroscopy (EDS) to study the shell and core separately. A further study can be done on refining the CaTiO₃ ratio in T/ES(calcined) system to maintain the chemical stability and pursue a higher CO₂ adsorption capacity in long term CO₂ adsorption/desorption cycles. For future application, a three dimensional scaffold is more practical and convenient for delivery, installation and replacement. Therefore, fabricating large size scaffold of CaTiO₃ doped CaO adsorbents will be a very interesting but challenging direction. Several aspects should be considered and investigated such as the CO₂ adsorption capacity and stability, the texture, the pore diameter and structure, operation life and heating exchange.

Summary

The present research work has focused on the adsorption as a CO₂ capture and separation technology to investigate the physisorption and chemisorption. A series of carbon materials were selected as physisorption adsorbents and CaO-based materials were derived from wasted eggshells as chemisorption solid sorbents. The main experimental techniques used were gas adsorption with micromeritics accelerated surface area and porosimetry system 2020 (micromeritics ASAP 2020). Different TiO₂ doped CaO-based adsorbents were prepared by the thermal synthesis through solid state chemical reaction.

Granular activated carbon, graphenes, carbon nanotubes (single-walled and multi-walled), graphite, fullerene were chosen as CO₂ physisorption materials without further modification or purification. There are various adsorption sites for carbon materials including internal surfaces, external surfaces, interstitial channels and external grooves. The activation order for these sites are $E(\text{internal pore}) > E(\text{interstitial channels}) > E(\text{external grooves}) > E(\text{external surface})$. Granular activated carbon had the highest micro-pores with internal pore as dominator of CO₂ adsorption, graphenes were plate nano-sheets and possessed interstitial channels as the CO₂ storeroom. The preferential interaction of CO₂ and graphenes were the π orbital of CO₂ and π ring of graphenes. The external grooves and surfaces and interstitial channels were the adsorption sites for carbon nanotubes. However, the role of the interstitial channels in adsorbing CO₂ depended on the sizes of tubes. The same active sites as on nanotubes were supposed to exist on the fullerene for CO₂ adsorption. The CO₂ adsorption of fullerene was quite low due to the low surface area and porosity. The same went for the graphite with very bad CO₂ performance. The BET specific surface area of graphene-750 (716 m²/g) was the highest one, followed by granular activated carbons with 617 m²/g, single-walled nanotubes with 390 m²/g, and graphene-125 with 124 m²/g. The BET specific surface areas of multi-walled carbon nanotubes were below 100 m²/g and the surface areas of graphite and fullerene were smaller than 3 m²/g. On the contrary, the CO₂ adsorption quantity of granular activated carbon was the largest with value of 1.78 mol/kg, the second one was graphene-750 with CO₂ adsorbed amount of 1.43 mol/kg and graphene-125 adsorbed 0.83 mol/kg CO₂. Comparing the micropore surface areas for these adsorbents, one could find that activated carbon

owned the highest micropore surface area ($273 \text{ m}^2/\text{g}$), while the micropore surface areas were $195 \text{ m}^2/\text{g}$ and $55 \text{ m}^2/\text{g}$ for graphene-750 and graphene-125, respectively. As a consequence of the different micropore surface areas, the CO_2 physisorption on carbon materials varied from one to another.

The calcined eggshells without doping were produced and the SEM results indicated that the structure of the decomposed eggshells were tunnel-shape gaps and micro rods. The N_2 adsorption showed that the porosity in this sample was very low. After the CO_2 chemisorption, the surface area increased due to the pore reconstruction and recrystallization. At the carbonation stage, the small pores were filled firstly by CaCO_3 while some space of big pores was left unfilled. During the decarbonation the existed pores shrunk due to the sintering, which tended to reduce the free energy by reducing surface area. The small pores on the other hand due to the CO_2 outward transportation regrew and became larger. Therefore, the surface area raised because of the CO_2 flowing and this also led to the kinetic reaction rate switching from diffusion to surface controlled rate. The stability of CO_2 adsorption performance for calcined eggshell was not ideal because of the severe decaying in both CO_2 adsorption capacity and CaO carbonation conversion. The morphologies and N_2 physisorption properties demonstrated that the surface area and porosity dropped dramatically during CO_2 adsorption/desorption cycles. This was caused by the sintering effect. Two series of doped CaO-based adsorbents with shell/core structure were prepared by solid state thermal reaction at $850 \text{ }^\circ\text{C}$ for 2 hours. Under this heating parameters, a tiny portion of TiO_2 remained without reaction with CaO for T/ES(250) samples. The inert layer ($\text{CaTiO}_3/\text{TiO}_2$) hindered the sintering effect to some certain extent, which could be observed by morphology photos as well as the surface areas and pore size distributions. The CO_2 chemisorption performance tendencies of T/ES(250) samples were similar to the ES(250) and the stability of CO_2 adsorption was not improved. The reasons could be the powder sizes. Although a ES(250) consisted of tunnel-shape gaps and micro rods. The CaTiO_3 could not penetrated into the deep inner of CaO which meant that this inert layer only isolated the contact between the powders but not the micro rods. The second series of doped CaO-based materials were T/ES(calcined) which applied ES(250) powders as source to produce hybrid sorbents. A pure two-phase system (CaTiO_3 and CaO) were obtained for T/ES(calcined) and the chemisorption behaviors were improved much with steady CO_2 adsorption capacities and CaO carbonation

conversions. The chemical reaction isotherms indicated that the major CO₂ reaction happened at the pressures lower than 3 kPa with surface reaction rate. The stability of T(27)/ES(calcined) with TiO₂ particle size of 27 nm as reaction agent was superior than that of T(44)/ES(calcined) with TiO₂ particle size of 44 μm as source. T(27)/ES(calcined) with low percentage of CaTiO₃ could still remain a good CO₂ adsorption performance with 11.86 mol/kg adsorbed CO₂ quantity and 78 % of CaO carbonation conversion. Comparing the N₂ physisorption properties of T/ES(calcined) to the ES(250) and T/ES(250), one could discover that the surface area and porosity in T/ES(calcined) samples were preserved on a relative constant level, which was the reason for the good performance on CO₂ capture and separation.

As the physisorption and chemisorption of CO₂ capture and separation were both investigated in this work, it is very obvious that the chemical adsorbents possessed almost 10 times higher CO₂ adsorption capacity than physical adsorbents as well as the higher selectivity due to the chemical bonds forming between CaO and CO₂. However, the operation temperature for chemical adsorbents was much higher than physical sorbents, which implied more energy consumption. The energy for physisorption and chemisorption was different because of the diverse driving forces. In CO₂ physisorption, the bonding was mainly van der Waals force and the bonding in CO₂ chemisorption was covalent or ion bonding forces. Both adsorptions were very useful depending on the operation environment. For example, CaO-based adsorbents can be applied in electric plant, which deals with high temperature gases and can save some energy for the CO₂ capture and separation process. Carbon materials can be used at some mild environment with low temperature.

References

- [1] Stocker TF, D. Qin, G.K. Plattner, M. Tignor, S.K. Allen, J. Boschung, A. Nauels, Y. Xia, V. Bex and P.M. Midgley. IPCC, 2013: Climate Change 2013: The physical science basis. Contribution of Working Group I to the Fifth Assessment Report of the Intergovernmental Panel on Climate Change. Cambridge, United Kingdom and New York, NY, USA 2013. p. 1535.
- [2] NASA. The NASA Earth's Energy Budget Poster. 2014.
- [3] Loeb NG, Wielicki BA, Doelling DR, Smith GL, Keyes DF, Kato S, et al. Toward Optimal Closure of the Earth's Top-of-Atmosphere Radiation Budget. *J Climate*. 2009;22:748-66.
- [4] Trenberth KE, Fasullo JT, Kiehl J. Earth's Global Energy Budget. *Bulletin of the American Meteorological Society*. 2009;90:311-23.
- [5] Tans P. NOAA/ESRL (www.esrl.noaa.gov/gmd/ccgg/trends/). 2014.
- [6] Foley J. Boundaries for a Healthy Planet. *Scientific American*. 2010;302:54-7.
- [7] James Hansen MS, Pushker Kharecha, David Beerling, Robert Berner, Valerie Masson-Delmotte MP, Maureen Raymo, Dana L. Royer, James C. Zachos Target Atmospheric CO₂: Where Should Humanity Aim? . *The Open Atmospheric Science Journal* 2008;2:217-31.
- [8] UNFCCC. Status of Ratification of the Kyoto Protocol. 2014.
- [9] Sims RH. Renewable Energy and Climate Change Mitigation: An Overview of the IPCC Special Report. In: Troccoli A, Dubus L, Haupt SE, editors. *Weather Matters for Energy*: Springer New York; 2014. p. 91-110.
- [10] Lehtveer M, Hedenus F. Nuclear power as a climate mitigation strategy – technology and proliferation risk. *Journal of Risk Research*. 2014;1-18.
- [11] de Gouw JA, Parrish DD, Frost GJ, Trainer M. Reduced emissions of CO₂, NO_x, and SO₂ from U.S. power plants owing to switch from coal to natural gas with combined cycle technology. *Earth's Future*. 2014;2:75-82.
- [12] Creutzig F, Ravindranath NH, Berndes G, Bolwig S, Bright R, Cherubini F, et al. Bioenergy and climate change mitigation an assessment, *GCB Bioenergy Early View*. *GCB Bioenergy*. 2014:n/a.
- [13] Chaturvedi V, Shukla PR. Role of energy efficiency in climate change mitigation policy for India: assessment of co-benefits and opportunities within an integrated assessment modeling framework. *Climatic Change*. 2014;123:597-609.
- [14] Florian H, Alexander P, Jan Philip D, David K, Hermann L-C, Markus B, et al. Investigating afforestation and bioenergy CCS as climate change mitigation strategies. *Environmental Research Letters*. 2014;9:064029.

- [15] Markusson N, Ginn F, Singh Ghaleigh N, Scott V. 'In case of emergency press here': framing geoengineering as a response to dangerous climate change. *Wiley Interdisciplinary Reviews: Climate Change*. 2014;5:281-90.
- [16] Kalkuhl M, Edenhofer O, Lessmann K. *The Role of Carbon Capture and Sequestration Policies for Climate Change Mitigation*. Environmental and Resource Economics. 2014.
- [17] Metz B, O. Davidson, H. C. de Coninck, M. Loos, and L. A. Meyer. *IPCC Special Report on Carbon Dioxide Capture and Storage*. Prepared by Working Group III of the Intergovernmental Panel on Climate Change. Cambridge, United Kingdom and New York, NY, USA: Cambridge University Press; 2005. p. 442.
- [18] Kumar S, Cho JH, Moon I. Ionic liquid-amine blends and CO₂ BOLs: Prospective solvents for natural gas sweetening and CO₂ capture technology: A review. *International Journal Of Greenhouse Gas Control*. 2014;20:87-116.
- [19] Poste AE, Grung M, Wright RF. Amines and amine-related compounds in surface waters: A review of sources, concentrations and aquatic toxicity. *Sci Total Environ*. 2014;481:274-9.
- [20] Gargiulo N, Pepe F, Caputo D. CO₂ Adsorption by Functionalized Nanoporous Materials: A Review. *J Nanosci Nanotechno*. 2014;14:1811-22.
- [21] Rezakazemi M, Amooghin AE, Montazer-Rahmati MM, Ismail AF, Matsuura T. State of the art membrane based CO₂ separation using mixed matrix membranes (MMMs): An overview on current status and future directions. *Prog Polym Sci*. 2014;39:817-61.
- [22] Bachelier F, Sun SH. Process and apparatus for the separation of air by cryogenic distillation. *Google Patents*; 2014.
- [23] Smith AR, Klosek J. A review of air separation technologies and their integration with energy conversion processes. *Fuel Processing Technology*. 2001;70:115-34.
- [24] Leung DY, Caramanna G, Maroto-Valer MM. An overview of current status of carbon dioxide capture and storage technologies. *Renewable and Sustainable Energy Reviews*. 2014;39:426-43.
- [25] Xu G, Liang FF, Yang YP, Hu Y, Zhang K, Liu WY. An Improved CO₂ Separation and Purification System Based on Cryogenic Separation and Distillation Theory. *Energies*. 2014;7:3484-502.
- [26] Maqsood K, Pal J, Turunawarasu D, Pal AJ, Ganguly S. Performance enhancement and energy reduction using hybrid cryogenic distillation networks for purification of natural gas with high CO₂ content. *Korean J Chem Eng*. 2014;31:1120-35.
- [27] Wilcox J. *Carbon Capture*. New York, USA: Springer Science+Business Media, LLC; 2012.

- [28] Aaron D, Tsouris C. Separation of CO₂ from Flue Gas: A Review. *Separation Science and Technology*. 2005;40:321-48.
- [29] Wilcox J, Haghpanah R, Rupp EC, He J, Lee K. Advancing adsorption and membrane separation processes for the gigaton carbon capture challenge. *Annual review of chemical and biomolecular engineering*. 2014;5:479-505.
- [30] Robeson LM. The upper bound revisited. *J Membrane Sci*. 2008;320:390-400.
- [31] D'Alessandro DM, Smit B, Long JR. Carbon dioxide capture: prospects for new materials. *Angewandte Chemie*. 2010;49:6058-82.
- [32] Scholes CA, Chen GQ, Stevens GW, Kentish SE. Nitric oxide and carbon monoxide permeation through glassy polymeric membranes for carbon dioxide separation. *Chemical Engineering Research and Design*. 2011;89:1730-6.
- [33] Bernardo P, Drioli E, Golemme G. Membrane Gas Separation: A Review/State of the Art. *Industrial & Engineering Chemistry Research*. 2009;48:4638-63.
- [34] Pera-Titus M. Porous inorganic membranes for CO₂ capture: present and prospects. *Chemical reviews*. 2014;114:1413-92.
- [35] Songolzadeh M, Soleimani M, Ravanchi MT, Songolzadeh R. Carbon Dioxide Separation from Flue Gases: A Technological Review Emphasizing Reduction in Greenhouse Gas Emissions. *Sci World J*. 2014.
- [36] Goh PS, Ismail AF, Sanip SM, Ng BC, Aziz M. Recent advances of inorganic fillers in mixed matrix membrane for gas separation. *Separation and Purification Technology*. 2011;81:243-64.
- [37] Li S, Martinek JG, Falconer JL, Noble RD, Gardner TQ. High-Pressure CO₂/CH₄ Separation Using SAPO-34 Membranes. *Industrial & Engineering Chemistry Research*. 2005;44:3220-8.
- [38] Yu M, Noble RD, Falconer JL. Zeolite Membranes: Microstructure Characterization and Permeation Mechanisms. *Accounts of Chemical Research*. 2011;44:1196-206.
- [39] Funke HH, Chen MZ, Prakash AN, Falconer JL, Noble RD. Separating molecules by size in SAPO-34 membranes. *J Membrane Sci*. 2014;456:185-91.
- [40] Zhang X-L, Qiu L-F, Ding M-Z, Hu N, Zhang F, Zhou R-F, et al. Preparation of Zeolite T Membranes by a Two-Step Temperature Process for CO₂ Separation. *Industrial & Engineering Chemistry Research*. 2013;52:16364-74.
- [41] van den Bergh J, Tihaya A, Kapteijn F. High temperature permeation and separation characteristics of an all-silica DDR zeolite membrane. *Microporous and Mesoporous Materials*. 2010;132:137-47.
- [42] Zhang J, Burke N, Zhang S, Liu K, Pervukhina M. Thermodynamic analysis of molecular simulations of CO₂ and CH₄ adsorption in FAU zeolites. *Chemical*

Engineering Science. 2014;113:54-61.

[43] Sjöberg E, Sandström L, Öhrman OGW, Hedlund J. Separation of CO₂ from black liquor derived syngas using an MFI membrane. *J Membrane Sci.* 2013;443:131-7.

[44] Zhou M, Korelskiy D, Ye P, Grahn M, Hedlund J. A uniformly oriented MFI membrane for improved CO₂ separation. *Angewandte Chemie.* 2014;53:3492-5.

[45] Mason CR, Maynard-Atem L, Heard KW, Satilmis B, Budd PM, Friess K, et al. Enhancement of CO₂ Affinity in a Polymer of Intrinsic Microporosity by Amine Modification. *Macromolecules.* 2014;47:1021-9.

[46] Rodenas T, van Dalen M, García-Pérez E, Serra-Crespo P, Zornoza B, Kapteijn F, et al. Visualizing MOF Mixed Matrix Membranes at the Nanoscale: Towards Structure-Performance Relationships in CO₂/CH₄ Separation Over NH₂-MIL-53(Al)@PI. *Advanced Functional Materials.* 2014;24:249-56.

[47] Nie F, He G, Zhao W, Ju J, Liu Y, Dai Y. Improving CO₂ separation performance of the polyethylene glycol (PEG)/polytrifluoropropylsiloxane (PTFPMS) blend composite membrane. *Journal of Polymer Research.* 2013;21.

[48] Liang L, Gan Q, Nancarrow P. Composite ionic liquid and polymer membranes for gas separation at elevated temperatures. *J Membrane Sci.* 2014;450:407-17.

[49] Severance M, Wang B, Ramasubramanian K, Zhao L, Ho WS, Dutta PK. Rapid crystallization of faujasitic zeolites: mechanism and application to zeolite membrane growth on polymer supports. *Langmuir : the ACS journal of surfaces and colloids.* 2014;30:6929-37.

[50] Switzer JR, Ethier AL, Hart EC, Flack KM, Rumble AC, Donaldson JC, et al. Design, synthesis, and evaluation of nonaqueous silylamines for efficient CO₂ capture. *ChemSusChem.* 2014;7:299-307.

[51] Zheng S, Tao M, Liu Q, Ning L, He Y, Shi Y. Capturing CO₂ into the Precipitate of a Phase-Changing Solvent after Absorption. *Environmental science & technology.* 2014;48:8905-10.

[52] Ramdin M, de Loos TW, Vlucht TJH. State-of-the-Art of CO₂ Capture with Ionic Liquids. *Industrial & Engineering Chemistry Research.* 2012;51:8149-77.

[53] Sistla YS, Khanna A. Carbon dioxide absorption studies using amine-functionalized ionic liquids. *Journal of Industrial and Engineering Chemistry.* 2014;20:2497-509.

[54] Luo X, Guo Y, Ding F, Zhao H, Cui G, Li H, et al. Significant improvements in CO₂ capture by pyridine-containing anion-functionalized ionic liquids through multiple-site cooperative interactions. *Angewandte Chemie.* 2014;53:7053-7.

[55] Samanta A, Zhao A, Shimizu GKH, Sarkar P, Gupta R. Post-Combustion CO₂ Capture Using Solid Sorbents: A Review. *Industrial & Engineering Chemistry*

Research. 2012;51:1438-63.

[56] Wang Q, Luo J, Zhong Z, Borgna A. CO₂ capture by solid adsorbents and their applications: current status and new trends. *Energy & Environmental Science*. 2011;4:42.

[57] Jianghua Ling AN, Penny Xiao, Dong Xu, Paul A Webley, Yuchun Zhai. Overview of CO₂ Capture from Flue Gas Streams by Vacuum Pressure Swing Adsorption Technology. *Austin Journal of Chemical Engineering*. 2014;1:7.

[58] Pirngruber GDL-I-C, Damien. Design of a Pressure Swing Adsorption Process for Postcombustion CO₂ Capture. *Industrial & Engineering Chemistry Research*. 2013;52:5985-96.

[59] Sculley JP, Verdegaal WM, Lu W, Wriedt M, Zhou HC. High-throughput analytical model to evaluate materials for temperature swing adsorption processes. *Adv Mater*. 2013;25:3957-61.

[60] Ribeiro RPPL, Grande CA, Rodrigues AE. Electric Swing Adsorption for Gas Separation and Purification: A Review. *Separation Science and Technology*. 2014;49:1985-2002.

[61] Yu C-H. A Review of CO₂ Capture by Absorption and Adsorption. *Aerosol Air Qual Res*. 2012.

[62] Yu J, Balbuena PB. Water Effects on Postcombustion CO₂ Capture in Mg-MOF-74. *The Journal of Physical Chemistry C*. 2013;117:3383-8.

[63] Yuan B, Wu X, Chen Y, Huang J, Luo H, Deng S. Adsorption of CO₂, CH₄, and N₂ on ordered mesoporous carbon: approach for greenhouse gases capture and biogas upgrading. *Environmental science & technology*. 2013;47:5474-80.

[64] Atluri R, Iqbal MN, Bacsik Z, Hedin N, Villaescusa LA, Garcia-Bennett AE. Self-assembly mechanism of folate-templated mesoporous silica. *Langmuir : the ACS journal of surfaces and colloids*. 2013;29:12003-12.

[65] Su F, Lu C, Kuo S-C, Zeng W. Adsorption of CO₂ on Amine-Functionalized Y-Type Zeolites. *Energy & Fuels*. 2010;24:1441-8.

[66] Heydari-Gorji A, Yang Y, Sayari A. Effect of the Pore Length on CO₂ Adsorption over Amine-Modified Mesoporous Silicas. *Energy & Fuels*. 2011;25:4206-10.

[67] Su F, Lu C, Chen HS. Adsorption, desorption, and thermodynamic studies of CO₂ with high-amine-loaded multiwalled carbon nanotubes. *Langmuir : the ACS journal of surfaces and colloids*. 2011;27:8090-8.

[68] Nguyen NT, Furukawa H, Gandara F, Nguyen HT, Cordova KE, Yaghi OM. Selective Capture of Carbon Dioxide under Humid Conditions by Hydrophobic Chabazite-Type Zeolitic Imidazolate Frameworks. *Angewandte Chemie*. 2014.

[69] Fracaroli AM, Furukawa H, Suzuki M, Dodd M, Okajima S, Gandara F, et al.

Metal-organic frameworks with precisely designed interior for carbon dioxide capture in the presence of water. *J Am Chem Soc.* 2014;136:8863-6.

[70] Shan S, Li S, Jia Q, Jiang L, Wang Y, Peng J. Impregnation Precipitation Preparation and Kinetic Analysis of Li_4SiO_4 -Based Sorbents with Fast CO_2 Adsorption Rate. *Industrial & Engineering Chemistry Research.* 2013;52:6941-5.

[71] Seggiani M, Puccini M, Vitolo S. Alkali promoted lithium orthosilicate for CO_2 capture at high temperature and low concentration. *International Journal of Greenhouse Gas Control.* 2013;17:25-31.

[72] Wang C, Dou B, Song Y, Chen H, Xu Y, Xie B. High Temperature CO_2 Sorption on Li_2ZrO_3 Based Sorbents. *Industrial & Engineering Chemistry Research.* 2014;53:12744-52.

[73] Yan Yan Li MMW, Wei Gang Lin, Ying Wang, Jian Hua Zhu. A novel porous MgO sorbent fabricated through carbon insertion. *J Mater Chem A.* 2014;2:12014-22.

[74] Lai CW. Modification of One-Dimensional TiO_2 Nanotubes with CaO Dopants for High CO_2 Adsorption. *Int J Photoenergy.* 2014.

[75] Liu Qiming MJ, Zhou Yuan, Wang Tianhe. Synthesis of MgO-Modified Mesoporous Silica and Its Adsorption Performance toward CO_2 . *Wuhan University Journal of Natural Science.* 2014;19:111-6.

[76] M. Elena Diego BA, Gemma Grasa, J. Carlos Abanades. Design of a Novel Fluidized Bed Reactor To Enhance Sorbent Performance in CO_2 Capture Systems Using CaO. *Industrial & Engineering Chemistry Research.* 2014;53:10059-71.

[77] Sengupta S, Reddy SA, Dongara R, Das AK, Bhunia H, Bajpai PK. Improvement in Regeneration Properties and Multicycle Stability for $\text{K}_2\text{CO}_3/\text{Al}_2\text{O}_3$ Adsorbents for CO_2 Removal from Flue Gas. *Energy & Fuels.* 2014;28:5354-62.

[78] Ishihara S, Sahoo P, Deguchi K, Ohki S, Tansho M, Shimizu T, et al. Dynamic breathing of CO_2 by hydrotalcite. *J Am Chem Soc.* 2013;135:18040-3.

[79] Michio Inagaki FK. *Materials Science and Engineering of Carbon: Fundamentals.* USA: Butterworth-Heinemann; 2014.

[80] Wang J, Senkowska I, Kaskel S, Liu Q. Chemically activated fungi-based porous carbons for hydrogen storage. *Carbon.* 2014;75:372-80.

[81] Shiflett MB, Corbin DR, Elliott BA, Subramoney S, Kaneko K, Yokozeki A. Sorption of trifluoromethane in activated carbon. *Adsorption.* 2014;20:565-75.

[82] Mestre AS, Freire C, Pires J, Carvalho AP, Pinto ML. High performance microspherical activated carbons for methane storage and landfill gas or biogas upgrade. *J Mater Chem A.* 2014;2:15337.

[83] Thomas E. Rufford DHJ, Jon Zhu. *Green Carbon Materials: Advances and Applications.* USA: Pan Stanford; 2014.

- [84] Wickramaratne NP, Jaroniec M. Activated carbon spheres for CO₂ adsorption. *ACS Appl Mater Interfaces*. 2013;5:1849-55.
- [85] Su F, Lu C, Hu S. Adsorption of benzene, toluene, ethylbenzene and p-xylene by NaOCl-oxidized carbon nanotubes. *Colloids and Surfaces A: Physicochemical and Engineering Aspects*. 2010;353:83-91.
- [86] Liu L, Nicholson D, Bhatia SK. Adsorption of CH₄ and CH₄/CO₂ mixtures in carbon nanotubes and disordered carbons: A molecular simulation study. *Chemical Engineering Science*. 2014.
- [87] Tylianakis E, Dimitrakakis GK, Martin-Martinez FJ, Melchor S, Dobado JA, Klontzas E, et al. Designing novel nanoporous architectures of carbon nanotubes for hydrogen storage. *International Journal of Hydrogen Energy*. 2014;39:9825-9.
- [88] Sun S-J. Gas adsorption on a single walled carbon nanotube-model simulation. *Physics Letters A*. 2008;372:3493-5.
- [89] Sandeep Agnihotri JPBM, Massoud Rostam-Abadi, Mark J. Rood. Structural Characterization of Single-Walled Carbon Nanotube Bundles by Experiment and Molecular Simulation. *Langmuir : the ACS journal of surfaces and colloids*. 2005;21:896-904.
- [90] Dutta D, Wood BC, Bhide SY, Ayappa KG, Narasimhan S. Enhanced Gas Adsorption on Graphitic Substrates via Defects and Local Curvature: A Density Functional Theory Study. *The Journal of Physical Chemistry C*. 2014;118:7741-50.
- [91] Cabrera-Sanfeliix P. Adsorption and Reactivity of CO₂ on Defective Graphene Sheets. *J Phys Chem A*. 2009;113:493-8.
- [92] Sanyal B, Eriksson O, Jansson U, Grennberg H. Molecular adsorption in graphene with divacancy defects. *Physical Review B*. 2009;79.
- [93] A. Martinez-Alonso JMDT. Physical Adsorption of Ar and CO₂ on C₆₀ Fullerene. *J Phys Chem B*. 2001;105:135-9.
- [94] A. Martinez-Alonso JMDT. Physisorption of Simple Gases on C₆₀ Fullerene. *Langmuir : the ACS journal of surfaces and colloids*. 2000;16:1343-8.
- [95] Zottl S, Kaiser A, Bartl P, Leidlmair C, Mauracher A, Probst M, et al. Methane Adsorption on Graphitic Nanostructures: Every Molecule Counts. *The journal of physical chemistry letters*. 2012;3:2598-603.
- [96] Delgado JA, Águeda VI, Uguina MA, Sotelo JL, Brea P, Grande CA. Adsorption and Diffusion of H₂, CO, CH₄, and CO₂ in BPL Activated Carbon and 13X Zeolite: Evaluation of Performance in Pressure Swing Adsorption Hydrogen Purification by Simulation. *Industrial & Engineering Chemistry Research*. 2014;140117091024005.
- [97] Dundar E, Zacharia R, Chahine R, B énard P. Potential theory for prediction of high-pressure gas mixture adsorption on activated carbon and MOFs. *Separation and*

Purification Technology. 2014;135:229-42.

[98] An-Hui Lu SD. Porous Materials for Carbon Dioxide Capture. Springer Heidelberg New York Dordrecht London: Springer; 2014.

[99] Khalili S, Ghoreyshi A, Jahanshahi M. Carbon dioxide captured by multi-walled carbon nanotube and activated charcoal: A comparative study. Chemical Industry and Chemical Engineering Quarterly. 2013;19:153-64.

[100] Casco ME, Morelos-Gómez A, Vega-Dáz SM, Cruz-Silva R, Tristán-López F, Muramatsu H, et al. CO₂ adsorption on crystalline graphitic nanostructures. Journal of CO₂ Utilization. 2014;5:60-5.

[101] Liu W, An H, Qin C, Yin J, Wang G, Feng B, et al. Performance Enhancement of Calcium Oxide Sorbents for Cyclic CO₂ Capture—A Review. Energy & Fuels. 2012;26:2751-67.

[102] Valverde JM. Ca-based synthetic materials with enhanced CO₂ capture efficiency. J Mater Chem A. 2013;1:447.

[103] Valverde JM, Perejon A, Perez-Maqueda LA. Enhancement of fast CO₂ capture by a nano-SiO₂/CaO composite at Ca-looping conditions. Environmental science & technology. 2012;46:6401-8.

[104] Wang F, Kuzuya T, Hirai S. Improvement of CO₂ Absorption Properties of Limestone Ore by the Addition of Reagent Grade-SiO₂ and Natural Diatomite. Mater Trans. 2011;52:2211-5.

[105] Lan PQ, Wu SF. Synthesis of a Porous Nano-CaO/MgO-Based CO₂ Adsorbent. Chemical Engineering & Technology. 2014;37:580-6.

[106] Broda M, Kierzkowska AM, Müller CR. Development of Highly Effective CaO-based, MgO-stabilized CO₂ Sorbents via a Scalable “One-Pot” Recrystallization Technique. Advanced Functional Materials. 2014;24:5753-61.

[107] Yu CT, Chen WC. Hydrothermal preparation of calcium-aluminum carbonate sorbent for high-temperature CO₂ capture in fixed-bed reactor. Fuel. 2014;122:179-85.

[108] Lee MS, Yogi Goswami D, Kothurkar N, Stefanakos EK. Development and Evaluation of Calcium Oxide Absorbent Immobilized on Fibrous Ceramic Fabrics for High Temperature Carbon Dioxide Capture. Powder Technology. 2014.

[109] Reddy GK, Quillin S, Smirniotis P. Influence of the Synthesis Method on the Structure and CO₂ Adsorption Properties of Ca/Zr Sorbents. Energy & Fuels. 2014;28:3292-9.

[110] Koirala R, Reddy GK, Lee JY, Smirniotis PG. Influence of Foreign Metal Dopants on the Durability and Performance of Zr/Ca Sorbents during High Temperature CO₂ Capture. Separation Science And Technology. 2014;49:47-54.

[111] Zhao C, Zhou Z, Cheng Z. Sol-gel-Derived Synthetic CaO-Based CO₂ Sorbents

Incorporated with Different Inert Materials. *Industrial & Engineering Chemistry Research*. 2014;140829133149007.

[112] Lide DR. *CRC Handbook of Chemistry and Physics*, Internet Version 2015. 95 ed. Boca Raton, FL: CRC Press; 2014.

[113] Yu C-T, Chen W-C. Preparation, characterization of Ca/Al carbonate pellets with TiO₂ binder and CO₂ sorption at elevated-temperature conditions. *Powder Technology*. 2013;239:492-8.

[114] S.F. Wu YQZ. Behavior of CaTiO₃/Nano-CaO as a CO₂ Reactive Adsorbent. *Industrial&Engineering Chemistry Research*. 2010;49:2701-076.

[115] Masahiko Aihara TN, Junro Matsushita, Yoichi Negishi, Haruhiko Ohya. Development of porous solid reactant for thermal-energy storage and temperature upgrade using carbonation decarbonation reaction. *Applied Energy*. 2001;69:225-38.

[116] Olivares-Marín M, Maroto-Valer MM. Development of adsorbents for CO₂ capture from waste materials: a review. *Greenhouse Gases: Science and Technology*. 2012;2:20-35.

[117] GLOBAL POULTRY TRENDS 2013: Growth in European Egg Production is Outside the EU. *The Poultry Site*; 2014.

[118] Varga D. SHELLBRANE Report Summary. 2014.

[119] Oliveira DA, Benelli P, Amante ER. A literature review on adding value to solid residues: egg shells. *Journal of Cleaner Production*. 2013;46:42-7.

[120] Witton T. Characterization of calcium oxide derived from waste eggshell and its application as CO₂ sorbent. *Ceramics International*. 2011;37:3291-8.

[121] Sacia ER, Ramkumar S, Phalak N, Fan LS. Synthesis and Regeneration of Sustainable CaO Sorbents from Chicken Eggshells for Enhanced Carbon Dioxide Capture. *Acs Sustain Chem Eng*. 2013;1:903-9.

[122] Mohammadi M, Lahijani P, Mohamed AR. Refractory dopant-incorporated CaO from waste eggshell as sustainable sorbent for CO₂ capture: Experimental and kinetic studies. *Chem Eng J*. 2014;243:455-64.

[123] A.D. McNaught AW. IUPAC. *Compendium of Chemical Terminology*. 2nd ed. Oxford: Blackwell Scientific Publications; 1997.

[124] S. J. Gregg KSW. *Adsorption, Surface Area and Porosity*. 2nd ed. London: Academic Press INC.; 1982.

[125] Clapeyron É. *Mémoire sur la puissance motrice de la chaleur*. Paris: Journal de l'École polytechnique XIV; 1834.

[126] Walter Greiner LN, Horst Stöcker. *Thermodynamics and statistical mechanics*: Springer-Verlag New York Berlin Heidelberg; 1994.

- [127] Loebenstein WV. Calculations and comparisons of nonideal gas corrections for use in gas adsorption. *Journal of Colloid and Interface Science*. 1971;36:397-400.
- [128] S.Lowell JES. *Powder Surface Area and Porosity*. 2nd ed. New York: Chapman and Hall; 1984.
- [129] Brunauer S. *The Adsorption of Gases and Vapors*. Vol. I, Physical Adsorption. USA: Princeton University Press; 1943.
- [130] Joyner LG, Weinberger EB, Montgomery CW. Surface Area Measurements of Activated Carbons, Silica Gel and other Adsorbents. *J Am Chem Soc*. 1945;67:2182-8.
- [131] K.S.W. Sing DHE, R.A.W. Haul, L. Moscou, R.A. Pierotti, J. Rouquerol, T. Siemieniewska. Reporting Physisorption Data for Gas/Solid Systems with Special Reference to the Determination of Surface Area and Porosity. *Pure & Appl Chem*. 1985;57:603-19.
- [132] Allen T. *Particle Size Measurement*. 5 ed. London, UK: Chapman & Hall; 1997.
- [133] Cohan LH. Sorption hysteresis and the vapor pressure of concave surfaces. *J Am Chem Soc*. 1938;60:433-5.
- [134] Gargiulo N, Peluso A, Aprea P, Pepe F, Caputo D. CO₂ Adsorption on Polyethylenimine-Functionalized SBA-15 Mesoporous Silica: Isotherms and Modeling. *J Chem Eng Data*. 2014;59:896-902.
- [135] Feng X, Hu G, Hu X, Xie G, Xie Y, Lu J, et al. Tetraethylenepentamine-Modified Siliceous Mesocellular Foam (MCF) for CO₂ Capture. *Industrial & Engineering Chemistry Research*. 2013;52:4221-8.
- [136] Han SJ, Bang Y, Kwon HJ, Lee HC, Hiremath V, Song IK, et al. Elevated temperature CO₂ capture on nano-structured MgO-Al₂O₃ aerogel: Effect of Mg/Al molar ratio. *Chem Eng J*. 2014;242:357-63.
- [137] Lee DW, Jin MH, Lee CB, Oh D, Ryi SK, Park JS, et al. Facile synthesis of mesoporous silica and titania supraparticles by a meniscus templating route on a superhydrophobic surface and their application to adsorbents. *Nanoscale*. 2014;6:3483-7.
- [138] Woodward RT, Stevens LA, Dawson R, Vijayaraghavan M, Hasell T, Silverwood IP, et al. Swellable, Water- and Acid-Tolerant Polymer Sponges for Chemoselective Carbon Dioxide Capture. *J Am Chem Soc*. 2014;136:9028-35.
- [139] Xu ZH, Yu JG, Low JX, Jaroniec M. Microemulsion-Assisted Synthesis of Mesoporous Aluminum Oxyhydroxide Nanoflakes for Efficient Removal of Gaseous Formaldehyde. *Acs Appl Mater Inter*. 2014;6:2111-7.
- [140] Todan L, Dascalescu T, Preda S, Andronescu C, Munteanu C, Culita DC, et al. Porous nanosized oxide powders in the MgO-TiO₂ binary system obtained by sol-gel method. *Ceramics International*. 2014.

- [141] Lee SY, Park SJ. Isothermal exfoliation of graphene oxide by a new carbon dioxide pressure swing method. *Carbon*. 2014;68:112-7.
- [142] Langmuir I. THE CONSTITUTION AND FUNDAMENTAL PROPERTIES OF SOLIDS AND LIQUIDS. PART I. SOLIDS. *J Am Chem Soc*. 1916;38:2221-95.
- [143] Langmuir I. THE ADSORPTION OF GASES ON PLANE SURFACES OF GLASS, MICA AND PLATINUM. *J Am Chem Soc*. 1918;40:1361-403.
- [144] Brunauer S, Emmett PH, Teller E. Adsorption of Gases in Multimolecular Layers. *J Am Chem Soc*. 1938;60:309-19.
- [145] Yunes PAWCORWCJPOYS. Analytical Methods in Fine Particle Technology. USA: Micromeritics Instrument Corporation; 1997.
- [146] Thomson W. On the equilibrium of vapour at a curved surface of liquid. *Philosophical Magazine Series 4*. 1871;42:448-52.
- [147] Halsey G. Physical Adsorption on Non - Uniform Surfaces. *The Journal of Chemical Physics*. 1948;16:931-7.
- [148] Harkins WD, Jura G. Surfaces of Solids. XIII. A Vapor Adsorption Method for the Determination of the Area of a Solid without the Assumption of a Molecular Area, and the Areas Occupied by Nitrogen and Other Molecules on the Surface of a Solid. *J Am Chem Soc*. 1944;66:1366-73.
- [149] Lippens BC, Linsen BG, Boer JHd. Studies on pore systems in catalysts I. The adsorption of nitrogen; apparatus and calculation. *Journal of Catalysis*. 1964;3:32-7.
- [150] Jones JE. On the Determination of Molecular Fields. II. From the Equation of State of a Gas. *Proceedings of the Royal Society of London Series A*. 1924;106:463-77.
- [151] Barrett EP, Joyner LG, Halenda PP. The Determination Of Pore Volume And Area Distributions In Porous Substances .1. Computations From Nitrogen Isotherms. *J Am Chem Soc*. 1951;73:373-80.
- [152] Micromeritics ASAP 2020 physisorption analyzer.
- [153] Ren X, Chen C, Nagatsu M, Wang X. Carbon nanotubes as adsorbents in environmental pollution management: A review. *Chem Eng J*. 2011;170:395-410.
- [154] Presser V, McDonough J, Yeon S-H, Gogotsi Y. Effect of pore size on carbon dioxide sorption by carbide derived carbon. *Energy & Environmental Science*. 2011;4:3059.
- [155] Calbi M, Riccardo J. Energy Barriers at the Ends of Carbon Nanotube Bundles: Effects on Interstitial Adsorption Kinetics. *Physical Review Letters*. 2005;94.
- [156] Oh J, Mo Y-H, Le V-D, Lee S, Han J, Park G, et al. Borane-modified graphene-based materials as CO₂ adsorbents. *Carbon*. 2014;79:450-6.

- [157] Mahesh V. Iyer L-SF. High temperature CO₂ capture using engineered enggshells: a route to carbon management. US Patent. US2006.
- [158] Dennis JS, Pacciani R. The rate and extent of uptake of CO₂ by a synthetic, CaO-containing sorbent. *Chemical Engineering Science*. 2009;64:2147-57.
- [159] Rout KR, Feroso J, Chen D, Jakobsen HA. Kinetic rate of CO₂ uptake of a synthetic Ca-based sorbent: Experimental data and numerical simulations. *Fuel*. 2014;120:53-65.
- [160] Lee D. An apparent kinetic model for the carbonation of calcium oxide by carbon dioxide. *Chem Eng J*. 2004;100:71-7.
- [161] Valverde JM, Sanchez-Jimenez PE, Perez-Maqueda LA. High and stable CO₂ capture capacity of natural limestone at Ca-looping conditions by heat pretreatment and recarbonation synergy. *Fuel*. 2014;123:79-85.
- [162] Sanchez-Jimenez PE, Valverde JM, Perez-Maqueda LA. Multicyclic conversion of limestone at Ca-looping conditions: The role of solid-state diffusion controlled carbonation. *Fuel*. 2014;127:131-40.
- [163] Alvarez D, Abanades JC. Determination of the Critical Product Layer Thickness in the Reaction of CaO with CO₂. *Industrial & Engineering Chemistry Research*. 2005;44:5608-15.
- [164] German RM, Munir ZA. Surface Area Reduction During Isothermal Sintering. *Journal of the American Ceramic Society*. 1976;59:379-83.
- [165] Hanaor DH, Sorrell C. Review of the anatase to rutile phase transformation. *J Mater Sci*. 2011;46:855-74.
- [166] Hegazy A, Prouzet E. Room Temperature Synthesis and Thermal Evolution of Porous Nanocrystalline TiO₂ Anatase. *Chemistry of Materials*. 2011;24:245-54.
- [167] Olivares-Marin M, Cuerda-Correa EM, Nieto-Sanchez A, Garcia S, Pevida C, Roman S. Influence of morphology, porosity and crystal structure of CaCO₃ precursors on the CO₂ capture performance of CaO-derived sorbents. *Chem Eng J*. 2013;217:71-81.
- [168] Vieille L, Govin A, Grosseau P. Improvements of calcium oxide based sorbents for multiple CO₂ capture cycles. *Powder Technology*. 2012;228:319-23.
- [169] Huang CH, Chang KP, Yu CT, Chiang PC, Wang CF. Development of high-temperature CO₂ sorbents made of CaO-based mesoporous silica. *Chem Eng J*. 2010;161:129-35.
- [170] Abanades JC, Alvarez D. Conversion Limits in the Reaction of CO₂ with Lime. *Energy & Fuels*. 2003;17:308-15.
- [171] Sun P, Grace JR, Lim CJ, Anthony EJ. The effect of CaO sintering on cyclic CO₂ capture in energy systems. *AIChE Journal*. 2007;53:2432-42.

[172] Ishikawa H, Oguro K, Kato A, Suzuki H, Ishii E. Preparation and properties of hydrogen storage alloy-copper microcapsules. *Journal of the Less Common Metals*. 1985;107:105-10.

[173] Akiyama T, Fukutani T, Ohta H, Takahashi R, Yagi J-I, Waseda Y. Microencapsulation of Mg-Ni hydrogen storage alloy. *Environmental and Energy Engineering*. 1995;41:1349-52.

Legends

List of Figures

Figure 1.1 Mean concentration of atmospheric CO₂ in May from 1958 to 2014 at the Mauna Loa Observatory in Hawaii.

Figure 1.2 Illustration of CO₂ capture and separation technologies and examples.

Figure 1.3 Sketch of gas cryogenic distillation.

Figure 1.4 Sketch of membrane separation.

Figure 1.5 Sketch of adsorption/absorption.

Figure 2.1 Scheme of adsorption process.

Figure 2.2 The six types of physisorption isotherms.

Figure 2.3 Hysteresis loop types of physisorption isotherm.

Figure 2.4 Illustration of contact angle.

Figure 2.5 Demonstration of pore size.

Figure 2.6 Illustration of the potential energy relationship between physisorption and chemisorption.

Figure 3.1 An overview of Micromeritics ASAP 2020.

Figure 3.2 High energy synchrotron radiation diffraction patterns for carbon materials.

Figure 3.3 Adsorption (solid line) and desorption (dash line) N₂ isotherms for different carbon materials at -196 °C.

Figure 3.4 Pore size distribution of different carbon materials with N₂ under -196 °C.

Figure 3.5 Pure CO₂ adsorption isotherms on various carbon materials at 25 °C.

Figure 3.6 Influence of micropore volumes on CO₂ adsorption capacities of carbon materials.

Figure 3.7 Relationships between CO₂ adsorption capacities and BET specific, micropore and external surface areas.

Figure 4.1 Flowchart of producing the CaO-based samples.

Figure 4.2 Normal camera photos of dried ES powders (sieve size: 125 μm - 250 μm).

Figure 4.3 SEM morphology of dried ES powders.

Figure 4.4 The powder size and pore width distributions of dried ES powders calculated by Image J from SEM micrographs.

Figure 4.5 The X-ray diffraction pattern for dried ES powders.

Figure 4.6 Normal camera photos of color changes for ES(250) heated at different

parameters: A-1) 750 °C, 1 h; A-2) 750 °C, 5 h; B-1) 800 °C, 1 h; B-2) 800 °C, 3 h; B-3) 800 °C, 5 h; C-1) 850 °C, 1 h; C-2) 850 °C, 2 h; C-3) 850 °C, 3 h; C-4) 850 °C, 5 h; D-1) 900 °C, 1 h.

Figure 4.7 The weight losses of ES(250) under different annealing temperatures with various holding time.

Figure 4.8 The X-ray diffraction patterns of ES(250) at different annealing temperatures for 1 hour.

Figure 4.9 The X-ray diffraction patterns of ES(250) heated at 750 °C, 800 °C and 850 °C for different hours.

Figure 4.10 The SEM micrographs of ES(250) heated at 850 °C for 2 hours.

Figure 4.11 The gap size and particle thickness distributions of ES(250) heated at 850 °C for 2 hours calculated by Image J from SEM micrographs.

Figure 4.12 Adsorption (solid line) and desorption (dash line) isotherms and pore size distributions with N₂ at -196 °C of ES(250) heated at 850 °C for 2 hours.

Figure 4.13 Adsorption (solid line) and desorption (dash line) isotherms and pore size distributions with N₂ at -196 °C of ES(250) after 1, 2, 5, 10 carbonation/decarbonation cycles.

Figure 4.14 Pore volumes and average pore widths of ES(250) after 1, 2, 5, 10 carbonation/decarbonation cycles.

Figure 4.15 SEM micrographs of ES(250) powders after different carbonation/decarbonation cycles: (A, B) 1 cycle without CO₂ reaction, (C, D) 1 cycle and (E, F) 10 cycles.

Figure 4.16 The 1st, 2nd, 5th and 10th carbonation (700 °C, 100 % CO₂) and chemical reaction rate isotherms of ES(250).

Figure 4.17 The CO₂ adsorption capacities and CaO carbonation conversions during carbonation (700 °C, 100 % CO₂)/decarbonation (850 °C, 100 % He) cycles of ES(250) powders heated at 850 °C for 2 hours.

Figure 4.18 Scheme of the experimental concept.

Figure 4.19 Normal camera photos of color changes for 10T(27)/ES(250) powders heated at different parameters: a-1) 750 °C, 1 h; a-2) 750 °C, 5 h; b-1) 800 °C, 1 h; b-2) 800 °C, 3 h; b-3) 800 °C, 5 h; c-1) 850 °C, 1 h; c-2) 850 °C, 2 h; c-3) 850 °C, 3 h; c-4) 850 °C, 5 h; d-1) 900 °C, 1 h.

Figure 4.20 Weight losses of 10T(27)/ES(250) powders under different annealing

temperatures with various holding time.

Figure 4.21 The X-ray diffraction patterns of 10T(27)/ES(250) powders at different annealing temperatures for 1 hour.

Figure 4.22 The X-ray diffraction patterns of 10T(27)/ES(250) powders heated at 750 °C, 800 °C and 850 °C for different hours.

Figure 4.23 The X-ray diffraction patterns of 10T(27)/ES(250) powders heated from 850 °C to 1200 °C for 2 hours.

Figure 4.24 SEM morphologies of 10T(27)/ES(250) powders heated at (A, B) 850 °C, (C, D) 1000 °C and (E, F) 1200 °C for 2 hours.

Figure 4.25 Adsorption (solid line) and desorption (dash line) isotherms and pore size distributions with N₂ at -196 °C of 10T(27)/ES(250) heated at 850 °C, 900 °C, 1000 °C, 1100 °C and 1200 °C for 2 hours.

Figure 4.26 The X-ray diffraction patterns of 10T/ES(250) without and with different TiO₂ sizes heated at 850 °C for 2 hours.

Figure 4.27 The stabilities of CaTiO₃ and TiO₂ during carbonation (700 °C, 100 % CO₂)/decarbonation (850 °C, 100 % He) procedures.

Figure 4.28 The 1st and 10th carbonation (700 °C, 100 % CO₂) isotherms of 10T/ES(250) powders with different TiO₂ sizes heated at 850 °C for 2 hours.

Figure 4.29 The 1st and 10th carbonation (700 °C, 100 % CO₂) reaction rate isotherms of 10T/ES(250) powders with different TiO₂ sizes heated at 850 °C for 2 hours.

Figure 4.30 Scheme of the layers after carbonation.

Figure 4.31 SEM morphologies of shell/core structures for 10T(27)/ES(250).

Figure 4.32 The X-ray diffraction patterns of T(27)/ES(250) with different T(27) concentrations heated at 850 °C for 2 hours.

Figure 4.33 Adsorption (solid line) and desorption (dash line) isotherms and pore size distributions with N₂ at -196 °C of T(27)/ES(250) with different T(27) concentrations heated at 850 °C for 2 hours.

Figure 4.34 BET specific surface area changes of T(27)/ES(250) with different initial T(27) concentrations heated at 850 °C for 2 hours.

Figure 4.35 The 1st and 10th carbonation (700 °C, 100 % CO₂) isotherms of T(27)/ES(250) with different T(27) concentrations heated at 850 °C for 2 hours.

Figure 4.36 The 1st and 10th carbonation (700 °C, 100 % CO₂) reaction rate isotherms of T(27)/ES(250) with different T(27) concentrations heated at 850 °C for 2 hours.

Figure 4.37 The maximum CO₂ uptakes during carbonation (700 °C, 100 % CO₂)/decarbonation (850 °C, 100 % He) cycles of T(27)/ES(250) powders with different T(27) concentrations and heated at 850 °C for 2 hours.

Figure 4.38 Adsorption (solid line) and desorption (dash line) isotherms and pore size distributions with N₂ at -196 °C of 10T(27)/ES(250) after 1, 2, 5, 10 carbonation/decarbonation cycles.

Figure 4.39 Pore volumes and average pore widths of 10T(27)/ES(250) after 1, 2, 5, 10 carbonation/decarbonation cycles.

Figure 4.40 SEM morphologies of 10T(27)/ES(250) after: (A, B) 1 and (C, D) 10 carbonation/decarbonation cycles.

Figure 4.41 SEM morphologies of 10T(27)/ES(250) under inert layer after: (A, B) 1 and (C, D) 10 carbonation/decarbonation cycle.

Figure 4.42 The 1st, 2nd, 5th and 10th carbonation (700 °C, 100 % CO₂) and chemical reaction rate isotherms of 10T(27)/ES(250).

Figure 4.43 The CO₂ adsorption capacities and CaO carbonation conversions during carbonation (700 °C, 100 % CO₂)/decarbonation (850 °C, 100 % He) cycles of 10T(27)/ES(250) powders heated at 850 °C for 2 hours.

Figure 4.44 The X-ray diffraction patterns of 10T/ES(calcined) powders with different TiO₂ sizes heated at 850 °C for 2 hours.

Figure 4.45 The 1st and 10th carbonation (700 °C, 100 % CO₂) isotherms of 10T/ES(calcined) powders with different TiO₂ sizes heated at 850 °C for 2 hours.

Figure 4.46 The 1st and 10th carbonation (700 °C, 100 % CO₂) reaction rate isotherms of 10T/ES(calcined) powders with different TiO₂ sizes heated at 850 °C for 2 hours.

Figure 4.47 The CO₂ adsorption capacities and CaO carbonation conversions during carbonation (700 °C, 100 % CO₂)/decarbonation (850 °C, 100 % He) cycles of 10T(27)/ES(calcined) heated at 850 °C for 2 hours.

Figure 4.48 The CO₂ adsorption capacities and CaO carbonation conversions during carbonation (700 °C, 100 % CO₂)/decarbonation (850 °C, 100 % He) cycles of 10T(44)/ES(calcined) heated at 850 °C for 2 hours.

Figure 4.49 Adsorption (solid line) and desorption (dash line) isotherms and pore size distributions with N₂ at -196 °C of 10T(27)/ES(calcined) after 1, 2, 5, 10 carbonation/decarbonation cycles.

Figure 4.50 Pore volumes and average pore widths of 10T(27)/ES(calcined) after 1, 2,

5, 10 carbonation/decarbonation cycles.

Figure 4.51 Scheme of pore rearranging during carbonation/decarbonation cycles: a) pristine sample, b) after the 1st carbonation, left pore (small) and right pore (large), c) after carbonation, left pore filled, d) after decarbonation, left pore expanded and right pore shrank.

Figure 4.52 The 1st, 2nd, 5th and 10th carbonation (700 °C, 100 % CO₂) and chemical reaction rate isotherms of 10T(27)/ES(calcined).

Figure 4.53 The X-ray diffraction patterns of 5T(27)/ES(calcined) powders heated at 850 °C for 2 hours.

Figure 4.54 The 1st and 10th carbonation (700 °C, 100 % CO₂) isotherms of 5T(27)/ES(calcined) heated at 850 °C for 2 hours.

Figure 4.55 The 1st and 10th carbonation (700 °C, 100 % CO₂) reaction rate isotherms of 5T(27)/ES(calcined) heated at 850 °C for 2 hours.

Figure 4.56 The CO₂ adsorption capacities and CaO carbonation conversions during carbonation (700 °C, 100 % CO₂)/decarbonation (850 °C, 100 % He) cycles of 5T(27)/ES(calcined) heated at 850 °C for 2 hours.

List of Tables

Table 2.1 Physisorption versus Chemisorption.

Table 3.1 The full widths at half maximum of plane (0 0 2) and (1 0 0) for carbon adsorbents calculated from high energy synchrotron radiation diffraction patterns.

Table 3.2 Physical properties of various carbon adsorbents.

Table 3.3 Pore volumes, sizes and distribution ranges for different carbon adsorbents.

Table 4.1 BET specific surface areas for ES(250) under different calcination conditions.

Table 4.2 BET specific surface areas of ES(250) after 0, 1, 2, 5, 10 carbonation/decarbonation cycles.

Table 4.3 Weight ratios and names of the samples.

Table 4.4 BET specific surface areas for 10T(27)/ES(250) under different annealing temperatures for 2 hours.

Table 4.5 BET specific surface areas of 10T(27)/ES(250) after 0, 1, 2, 5, 10 carbonation/decarbonation cycles.

Table 4.6 BET specific surface areas of 10T(27)/ES(calcined) after 0, 1, 2, 5, 10 carbonation/decarbonation cycles.

List of abbreviations

APW	average pore width (nm)
ASAP	Accelerated Surface Area and Porosimetry System
PV	total pore volume (cm ³ /g)
BET	Brunauer Emmett and Teller
BJH	Barrett-Joyner-Halenda
CNTs	carbon nanotubes
C ₆₀	fullerene
ES	eggshell
ES(250)	dried eggshell (size: 125 μm - 250 μm) after calcination
FWHM	full width at the half maximum
GACs	granular activated carbon
Graphene-125	graphene nano platelets (average surface area: 125 m ² /g)
Graphene-750	graphene nano platelets (average surface area: 750 m ² /g)
IUPAC	International Union of Pure and Applied Chemistry
MWNTs(1020)	multi-walled carbon nanotubes (diameter: 10 nm - 20 nm)
MWNTs(60100)	multi-walled carbon nanotubes (diameter: 60 nm - 100 nm)
PSD	pore size distribution
SEM	scanning electron microscopy
SWNTs(2)	single-walled carbon nanotubes (diameter: < 2 nm)
SSA	specific surface area
T(27)	TiO ₂ (particle size: 27 nm)
T(44)	TiO ₂ (particle size: 44 μm)
aT/ES(250)	samples prepared by TiO ₂ and dried eggshell as sources (weight ratio: a / 1-a)
T/ES(calcined)	samples prepared by TiO ₂ and calcined eggshell as sources
XRD	X-ray diffraction

Acknowledgements

First of all, I would like to express my sincere gratitude to Professor Eberhard Burkel, for his constant interest, patient tutorial and guidance. He has helped me both in the daily life and on my Ph.D thesis work with his experience, insight and advice.

I am grateful to have the financial support from China Scholarship Council.

I would like to warmly thank Prof. Christoph Schick and Prof. Martin Köckerling for the friendly help and suggestions on my work.

I would like to warmly thank Ms. Regina Lange, Prof. Thomas Gerber, Dr. Gerd Holzüter and the medical research center for the support with the scanning electron microscopy.

My deep thanks go to a former colleague Dr. Jianfeng Zhang for his constant support and patience.

Many thanks to the numerous beamtimes of BW5 in DESY/HASYLAB Hamburg.

Last but not least, I would like to thank all the people who made my work and life easier, happier and pleasant, my family, my friend Yeong Zen Chua, Ulrike Schröder, Stefan Flor and all my other colleagues in the villa.

Rostock, 01.10.2014

Qingqing Xu

Declaration

I hereby declare that this thesis is a presentation of my original research work and effort. It has not been submitted anywhere for any award. Where other sources of information have been used, they have been acknowledged.

Rostock, 01.10.2014

Qingqing Xu